DYNAMIC DEFORMATION BEHAVIOUR OF A DUAL-PHASE HIGH ENTROPY ALLOY

A Thesis Submitted to

Indian Institute of Technology Guwahati

in Partial Fulfilment of the Requirements

for the award of the degree of

DOCTOR OF PHILOSOPHY

by

SAMRAT TAMULY

DEPARTMENT OF MECHANICAL ENGINEERING

INDIAN INSTITUTE OF TECHNOLOGY GUWAHATI

GUWAHATI – 781039, INDIA

2023

Dedicated to my

Loving Family

Department of Mechanical Engineering

Indian Institute of Technology Guwahati

Guwahati-781039 INDIA

CERTIFICATE

It is certified that the work contained in the thesis entitled **"Dynamic Deformation Behaviour of a Dual-Phase High Entropy Alloy"** submitted by **Mr. SAMRAT TAMULY** to the **Indian Institute of Technology Guwahati** for the award of the degree of **Doctor of Philosophy** has been carried out under my supervision in the **Department of Mechanical Engineering**. This work has not been submitted elsewhere for the award of any other degree or diploma.

This thesis, in my opinion, has reached the standard fulfilling the requirements for the award of the degree of Doctor of Philosophy in accordance with the regulations of the institute.

(Dr.Prasenjit Khanikar)

Assistant Professor,

Department of Mechanical Engineering,

Indian Institute of Technology Guwahati

Guwahati-781039

INDIA

Department of Mechanical Engineering

Indian Institute of Technology Guwahati

Guwahati-781039, INDIA

SELF DECLARATION

I declare that,

a. The work contained in this thesis is original and has been carried out by me under the supervision of **Dr. Prasenjit Khanikar**.

b. To the best of my knowledge, the work has not been submitted to any other institute for any degree or diploma.

c. I have followed all the guidelines provided by the institute in preparing the thesis.

d. Whenever I have used any materials (data, theoretical analysis, figures) from any other sources, due credit has been given to all of them by properly citing the documents.

(Samrat Tamuly)
Department of Mechanical Engineering,
Indian Institute of Technology Guwahati,
Guwahati-781039
INDIA

ACKNOWLEDGMENT

The journey of doctoral study is always a difficult yet a spiritual one. I would have never successfully completed this thesis without the constant support of numerous people to whom I am indebted to.

*At foremost, I express my deepest gratitude to my supervisor, **Prof. Prasenjit Khanikar**, for his invaluable guidance and immense support throughout my Ph.D. work . His zeal and dedication to work for society, innovative thinking capability and ability to work tirelessly have always inspired me. His approach, combined with critical thinking, professional ethics, focusing on smart works and the presence of mind, will remain as a great lesson for the rest of my life. His guidance on doing systematic and constructive research with utmost liberty and a focused mind is remarkable. I am also extremely thankful to my collaborators **Dr. Saurabh Dixit from MIDHANI** and **Dr. Boopathy Kombaiah** from **Idaho National Lab** for their insightful inputs at every research outputs.*

*I am thankful to all Doctoral Committee members, **Prof. S. Kanagaraj**, **Prof. R. Ganesh Narayanan** and **Prof. Amit Shelke**, for their insightful comments and valuable suggestions during my progress of research work. I would also like to express my sincere thanks to all others faculty members from the **Department of Mechanical Engineering** for their help.*

*I would like to convey my special thanks to **Prof. P. Venkitanarayanan** and his students at Indian Institute of Technology Kanpur for allowing me to carry a significant part of my research in their lab, Prof. **Kamanio Chattopadhyay** and his students at Indian Institute of Science, Bengaluru for their initial help in alloy fabrication.*

*Very special thanks to all the faculties and staff members of the **Department of Mechanical Engineering, Central Workshop** and **Central Instruments Facility** centre of IIT Guwahati for providing all necessary facilities to carry out the research works.*

*The company of my beloved friends, notably **Akshay, Bikram, Avinish ji, Saptarshi Da, Jibajyoti, Monish, Prangan, Sid, Pranay and all my friends**, made my years of stay balanced, enjoyable and memorable at IIT Guwahati. Each of them deserves special appreciation. Special gratitude also goes to all my friends from **Christ Jyoti School, K.V. Nagaon, Tezpur University, NIT Surathkal** and **Indian Institute of Technology Guwahati**.*

Lastly I thank my family again, whose constant support during this sinusoidal journey of research kept me sane and my peace index reasonably high.

Place: **Date:** **Samrat Tamuly**

ABSTRACT

A novel dual-phase high entropy alloy comprising of FCC and BCC phases is processed at a large scale under industrial environment to understand the castability and scalability of high entropy alloys with a special attention towards strength-ductility balance and its potential use in high strain rate applications. Subsequently, appropriate experiments using split Hopkinson pressure bar were conducted and deformation behaviour from microstructural aspects were analysed. To understand the effect of cooling rate of solidification on the mechanical properties, the alloy was remelted and rapidly solidified at small-scale suction-cast laboratory environment. Furthermore, friction stir processing was also employed as a viable and effective rapid mass-production based thermo-mechanical process and the processed samples were compressed under a range of strain rates. For comparative analysis of the large-scale as-cast alloy, the suction-cast alloy and the friction stir processed alloy, the hardness, compressive strength, strain rate sensitivity, strain hardening behaviour and deformation mechanisms of all the alloy samples under both quasi-static and dynamic loading were examined. The friction stir processed samples exhibited the highest strength and the lowest strain rate sensitivity among all the conditions of the alloy. The as-cast alloy samples exhibited the highest strain rate sensitivity among all the alloy samples and excellent strain hardening at high strain rate of loading. The rapidly cooled suction-cast alloy displayed higher strength than the as-cast condition but lower strength than the friction stir processed samples. Similarly, the strain rate sensitivity of the suction-cast alloy was higher than the friction stir processed alloy and lower than the as-cast alloy. All the alloy samples were characterised by distinct deformation mechanisms under different strain rate regimes. The as-cast alloy resulted in wavy deformation bands under quasi-static loading conditions and deformation twins near interphase boundary under dynamic loading conditions. The suction-cast alloy under quasi-static compression displayed clear strain partitioning between FCC and BCC phases at moderate strains and the deformation became homogeneous without any strain partitioning at higher strains. The dynamic deformation in the suction-cast alloy resulted in the formation of deformation twins and bands. The friction stir processing of the as-cast alloy led to very high FCC to BCC phase transformation and grain refinement, and the deformation of the processed alloy further exhibited moderate stress induced phase transformation effect under both quasi-static and dynamic conditions. However, distinct twins were formed in friction stir processed alloy under dynamic loading which were almost absent under quasi-static compression.

Keywords: *High Entropy Alloys, Strengthening Mechanisms, High Strain Rate, Strain Rate Sensitivity, Deformation Mechanisms, Friction stir Processing*

CONTENTS

LIST OF ABBREVIATIONS

ASTM	American Society for Testing and Materials
BCC	Body Centred Cubic
DRX	Dynamic Recrystallization
EBSD	Electron Backscatter Diffraction
EDS	Energy Dispersive X-ray Spectrometer
FCC	Face Centred Cubic
FESEM	Field Emission Scanning Electron Microscope
FSP	Friction Stir Processing
GND	Geometrically Necessary Dislocation
GOS	Grain Orientation Spread
HEA	High Entropy Alloy
HSR	High Strain Rate
HV	Hardness Value
IM	Induction Melted (As-cast)
OIM	Orientation Image mapping
OM	Optical Micrograph
KAM	Kernel Average Misorientation
SC	Suction Cast
SHPB	Split Hopkinson Pressure Bar
SEM	Standard Error of the Mean
SRS	Strain Rate Sensitivity
TEM	Transmission Electron Microscopy
TRIP	Transformation Induced Plasticity
UTM	Universal Testing Machine
XRD	X-ray Diffraction

LIST OF FIGURES

LIST OF TABLES

Chapter 1
INTRODUCTION

1.1 Background

With the ever-depleting natural resources it becomes imperative to judiciously use the limited amount of remaining assets. High entropy alloys can cater to preventing the overburdening a single mineral rather distribute depletion in an equitable and sustainable manner. There is a wide range of High Entropy Alloys (HEA) that has been found so far with different combination of principal elements. In contrast to conventional alloy design, high entropy alloys (HEAs)/multi-component alloys (MCAs) are designed with five or more principal elements in equi-atomic or near equi-atomic ratios [1–3] . Despite such a unique compositional blend of selected elements, a simple solid solution is produced due to their high configurational entropy associated with multi-principal elements. The HEAs exhibit excellent high-temperature mechanical properties, corrosion resistance and cryogenic properties arising from their inherent sluggish diffusion rate and high lattice distortion [4] . High entropy alloys also have a low tendency to form intermetallic phase reducing the probability of failure of the material by sudden embrittlement making them an excellent prospect for structural and high impact absorbing applications [5].

HEAs are fabricated primarily by melting and casting techniques (vacuum arc melting, vacuum induction melting etc.). Despite the promising properties of HEAs, the two major impediments for industry-based applications are their castability at a large scale and associated chemical inhomogeneity. Due to these constraints, the production of HEAs at an industrial scale has not been explored widely [6–8]. Although Lu et al. has cast near eutectic alloy of around 2.5 kg [9] and Licavoli *et al.* [10] have induction-melted high entropy alloy in 8 kg ingots, no study was found on HEA fabrication at industrial melting of the order of

100 kg. The controlled cooling rate is also a challenge associated with the large-scale production of HEAs compared with lab-scale fabrication [11]. Among HEAs, AlCoCrFeNi alloy system with five principal elements is one of the extensively studied HEA groups [12–14]. The single-phase face centred cubic (FCC) based alloys of the AlCoCrFeNi system have low yield strength while exhibiting excellent ductility [14,15]. In contrast, most of the body centred cubic (BCC) based HEAs possess high strength with low ductility. Low strength of single-phase FCC high entropy alloys and low ductility of BCC high entropy alloys are great hindrances to structural and other industrial applications [15–17]. This is also one of the reasons that have led the researchers to develop multiphase/heterophase HEAs comprising both FCC and BCC phases to balance the trade-off between strength and ductility [16]. Recent studies have suggested that the presence of dual-phase HEAs having both FCC and BCC phases can also exhibit high strength at high temperatures [18].Furthermore, multiphase phase alloys have good castability with controllable microstructure and stable defect structures. Thus, multiphase HEAs have proved to be superior alloys than single-phase HEAs in terms of ease of processing and overall mechanical properties.

With the growing attention towards materials having properties related to blast protection, armour applications, shock mitigation, car crashworthiness, high speed forming, fast forming processes, high strain rate study has found considerable importance [14,19,20]. The dynamic loading study needs careful observation due to paramount difference from quasi static study as the wave propagation creates a discrete state of stress. The inertial forces which remain always in the state of equilibrium are neglected under low strain rate regimes. However, at high strain rates due to large deposition of energy at the surface of the material at high strain rates these forces are not neglected. The deformation mechanisms of metals and alloys at high strain rate is not only confined to deformation by slip but also has shown the formation of substructures, dislocation entangling, mechanical twinning etc.[14,20,21].

The studies on HEAs under dynamic loading has not been carried out extensively. The few works that have been investigated can be broadly based on these groups AlCoCrFeNi and CoCrFeMnNi [22–24]along with addition of some minor elements like Titanium (Ti), Silicon (Si) etc [25–27]. Various analysis that have been studied are focused on yield strength, strain hardening, strain rate sensitivity, microstructural evolution, deformation mechanisms, thermal softening behaviour and consistency of constitutive model. The contribution of the elements in the comprehensive mechanical properties have also been studied where it was felt necessary. Recent studies have showed promising mechanical properties of dual-phase as well as eutectic or near eutectic HEAs under dynamic loading [28–30].

As discussed, the strength ductility trade-off of HEAs in as-cast condition do not meet advance application requirements, tunability of the HEAs through various thermomechanical processes become imperative. Apart from compositional variation for hetero-phase HEAs, precipitation strengthened HEAs or their combined strengthening mechanisms, various thermomechanical processes can be employed to improve the mechanical properties of high entropy alloys because of the low stacking fault energies (SFE) are attributed with this class of alloys through straining, high temperature deformation, grain refinement [14,22,24,31]. Refining the grain structure from the coarse grain achieved during casting, controlling grain coarsening during annealing and the sluggish diffusion of HEAs are major problems faced in the path of applicability of HEAs. [32,33]. Friction stir welding/processing (FSP/FSW) is one the better methods of addressing the above-mentioned issues associated with HEAs. Application of FSP in HEAs is rapid thermo-mechanical process which not only refines the grans but also removes residual stresses , promotes dynamic recrystallization and enhances strain hardening through transformation induced plasticity in HEAs [32,34–38].

1.2 Literatute Review

1.2.1 High Entropy Alloy

History of high entropy alloys

First ignition that triggered research and development of the concept of high entropy alloys (HEAs) or multi principal alloy element alloys (MPEAs) or now complex concentrated alloys (CCAs) came from two independent research from Jien- Wei Yeh (2004) and Brien Cantor (2004) and one dependent research S Ranganathan (2003) [39–41]. Infact, Cantor began his work with his undergraduate student in 1981 and J.W Yeh started his earliest work on multicomponent alloys in 1991 based on high entropy of mixing. Prior to this, metal alloying was carried out to improve the physical, mechanical, chemical and electrical properties based on one principal element [42]. The common perception of formation of complex structures like intermetallic or intermediate phases were removed when Jien-Weh Yeh and his group observed that in $CuCoNiCrAl_xFe$ system exhibited simpler microstructures and Cantor *et al.* in his equimolar CoCrFeMnNi alloy formed single phase FCC solid solution [39]. Raganathan *et al.* in 2003 after discussions with J.W. Yeh actually published the first journal on HEAs along with bulk metallic glasses in his article “Alloyed pleasures – multi-metallic cocktails” in Current Science as a review and pointed out the limitation of metallurgist of combining elements of a single phase and encouraging multicomponent alloys [41].

Definition

High entropy alloys (HEAs) by definition are solid solution alloy system containing more than five principal elements with equimolar or near equimolar atomic percentage. In general, the atomic percentage of elements lies between 5% and 35%. This atomic percentage which restricts the definition of HEAs comes from experimental observation that shows that the Gibbs free energy (G) is negative for such combinations as the configurational entropy (S) is relatively to compete with enthalpy of mixing (H) to form random solid solutions [5,43]. Therefore, the value of configurational entropy higher than 1.5 R for an alloy system with five or more principal elements with above mentioned atomic percentages are considered HEAs as shown in Fig 1.1 (reproduced) [1]. However, with subsequent research and exploration, the definition multicomponent equimolar alloy under the category of HEAs and only those derived from the centre of the phase diagram have highest entropy. Entropy still contributes significantly to the characteristics of the alloy system. Besides, the narrow definition of HEAs from microstructural aspect that the alloy system must include only disordered solid solution are also challenged. This is because alloy system is also influenced by the enthalpy of mixing, atomic size and valence electron concentration which will be discussed subsequently [43].

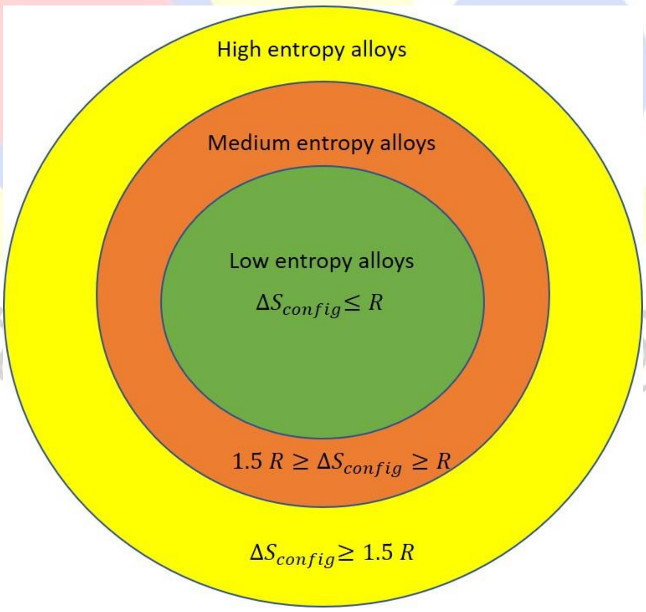

Figure 1.1 Alloy classification based on configurational entropy [1]

Phase prediction

As discussed, the final phase formation depends on multiple factors and possibility of formation of intermetallic as well as amorphous phase also exist depending on the alloying elements and solidification route. A parametric approach to the final phase formation is therefore utilized to understand the nature pf phases formed in HEAs which includes configurational entropy, enthalpy of mixing, atomic size mismatch and melting points [5,44,45].

(a) Thermodynamics and geometry effects

The thermodynamic effects of phase formation rules are derived from the Gibbs free energy G, the enthalpy H and the entropy S, by the following equation:

$$\Delta G_{mix} = \Delta H_{mix} - T\Delta S_{mix} \qquad 1.1$$

, where ΔG_{mix} is the Gibbs free energy of mixing, ΔH_{mix} is the enthalpy of mixing, ΔS_{mix} is the entropy of mixing and T is the temperature of the mixing elements.

The classical atomic size effect derived from Home-Ruthery rules and Inou empirical rules is modified for HAEs and Bulk metallic glasses (BMGs) to find the atomic size δ difference as the following:

$$\delta = \sqrt{\sum_{i=1}^{n} x_i (1 - \frac{d_i}{\sum_{j=1}^{n} x_j d_j})^2} \qquad 1.2$$

, where x_i , x_j= mole fraction of the elements

And d_i , d_j = diameter of the elements.

The entropy of mixing ΔS_{mix} is generated from configuration, vibration, electronic and magnetic contributions but the configurational entropy $\Delta S_{configurational}$ is dominant and therefore considered. This configurational entropy is given by:

This configurational entropy is given by:

$$\Delta S = -R\left(\frac{1}{x_i}\mathrm{In}\frac{1}{x_i} + \frac{1}{x_i}\mathrm{In}\frac{1}{x_i} \ldots \ldots . . \frac{1}{x_i}\mathrm{In}\frac{1}{x_i}\right) = R\mathrm{In}\frac{1}{x_i} \qquad 1.3$$

, where R = Universal gas constant = 8.314 KJ/K mol,

x_i = mole fraction of the elements.

Further, the enthalpy of mixing ΔH_{mix} for multicomponent alloys is given by:

$$\Delta H_{mix} = \sum_{i=1, i \neq j}^{n} 4\, \Delta H_{AB}^{mix}\, x_i x_j \qquad 1.4$$

, where, ΔH_{mix} = enthalpy of mixing

ΔH_{AB}^{mix} = Enthalpy of mixing for binary equiatomic alloy

x_i, x_j = Mole fraction of the elements

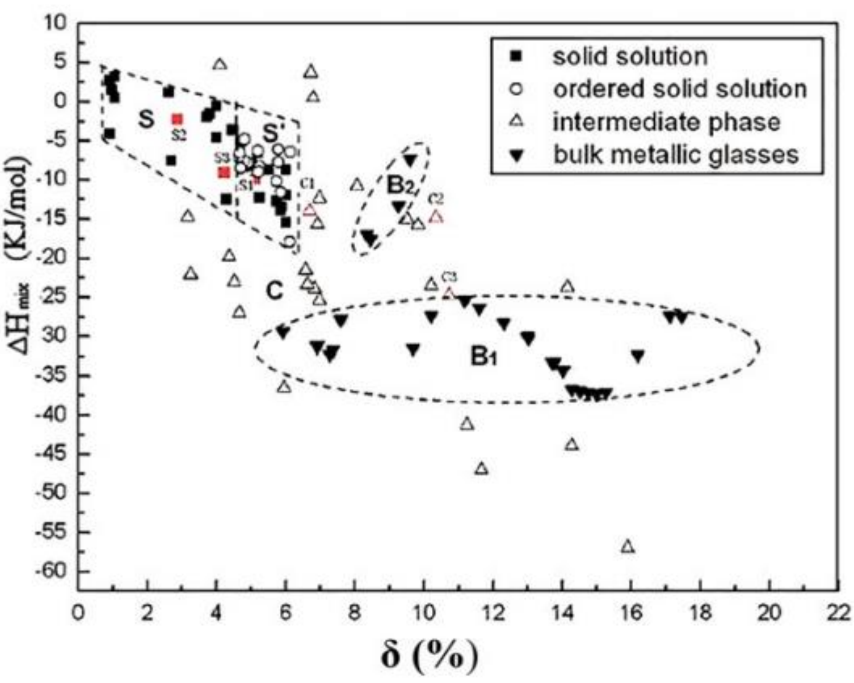

Figure 1.2 Phase selection map based on enthalpy of mixing and atomic size difference [46]

While plotting the enthalpy of mixing with the atomic size difference as shown in Fig 1.2 (*permission sought*), it was seen low atomic size difference allow component to substitute smoothly and equal probability exist for the atoms to occupy lattice sites to form solid solutions with ΔH_{mix} not negative enough to form compounds. As the atomic size effect increases as shown in S`, both ordered and disordered solid solution exist for similar range of enthalpy as S.

The entropy of mixing ΔS_{mix} is generated from configuration, vibration, electronic and magnetic contributions but the configurational entropy $\Delta S_{configurational}$ is dominant and therefore considered. This configurational entropy is given by:

$$\Delta S_{configurational} = -R\left(\frac{1}{x_i}\mathrm{In}\frac{1}{x_i} + \frac{1}{x_i}\mathrm{In}\frac{1}{x_i} \dots \dots \dots \frac{1}{x_i}\mathrm{In}\frac{1}{x_i}\right) = R\mathrm{In}\frac{1}{x_i} \qquad 1.5$$

, where R = Universal gas constant = 8.314 KJ/K mol, x_i = mole fraction of the elements.

But with high values of $\Delta S_{configurational}$, solid solution formation occurs prior to the formation of intermetallic, thus reducing the maximum number of phases formed in HEAs. The combined plot of Fig 1.2 replotted along with the entropy effect is shown in Fig 1.3 (*permission sought*). It was observed that all HEAs have high values of entropy $\Delta S_{configurational}$ in the range of 12-17.5 J/ (mol K) with smaller values of atomic size difference δ.

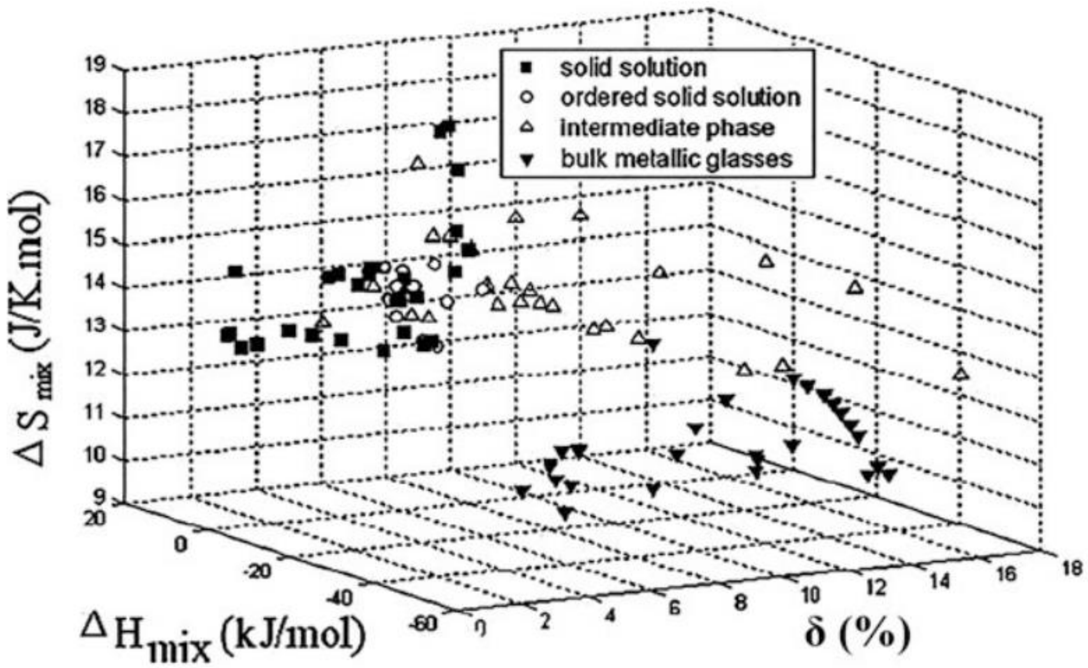

Figure 1.3 Phase selection diagram of HEAs and BMGs based on enthalpy, entropy and size effect [46]

Further combining the effects of atomic size, enthalpy and configurational entropy a new parameter Ω is developed that can be calculated as follows:

$$\Omega = \frac{T_m \Delta S_{mix}}{|\Delta H_{mix}|} \quad 1.6$$

$$T_m = \sum_{i=1}^{n} x_i (T_m)_i \quad 1.7$$

, where T_m is the average melting temperature of N principal elements of the alloy. The analysis of the Ω and δ the criteria for formation of solid solutions in multicomponent alloys were that $\Omega \geq 1.1$ and $\delta \leq 6.6\%$. Again, taking into consideration the Ω and number of elements N, shown in Fig 1.4 (*permission sought*)it can be inferred that larger values of Ω and N, resulted in solid solutions.

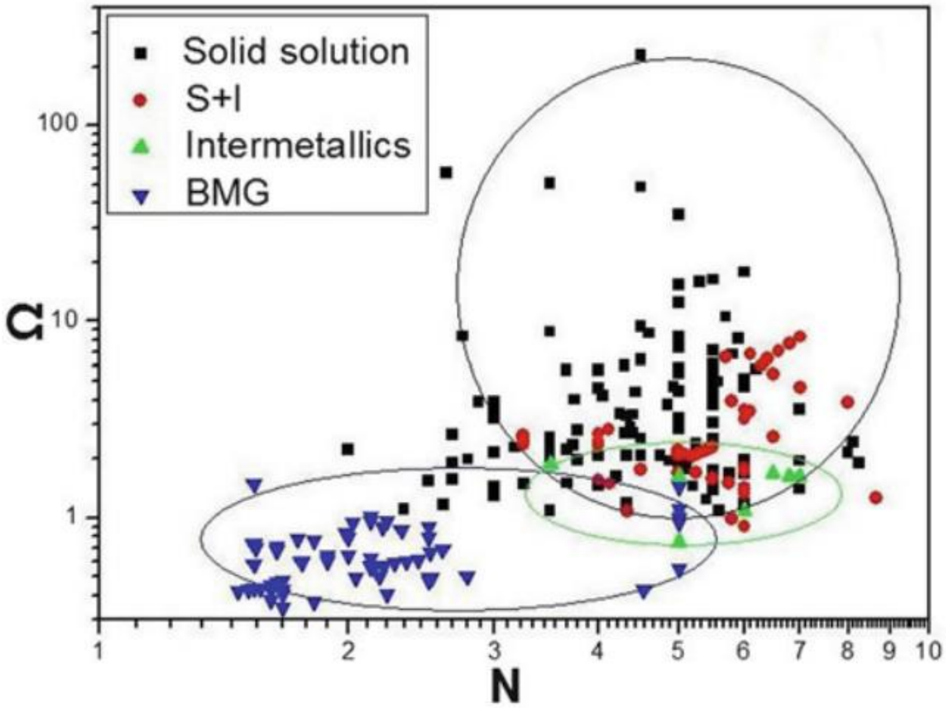

Figure 1.4 Phase selection diagrams of HEAs and BMGs based on Ω and number of elements (permission) [45]

VEC rule

Valence electron concentration (VEC) is the total number of d electrons present in the valence band and they play an important role in the stability of phase and physical properties of an alloy system. It was experimentally shown that for Al_x-TM (transition metal) system of HEAs, increasing the concentration of Al leads to decrease in the VEC. For FCC and BCC phase formation in multicomponent alloys, it was found that single phase FCC base HEAs are formed at VEC>8, BCC phases VEC<6.87 and for both FCC and BCC phases to exist the VEC must lie between 6.87 and 8. Thus, the VEC rule help in designing FCC and BCC based HEAs [47–49].

Core effects of HEAs

The core effects of HEAs focus around the composition, processing, crystal structure along with microstructure, physical and mechanical properties. There four principal effects i.e. considered core in HEAs. These were proposed in 2006 taking into consideration the thermodynamics and they influence different aspects of physical metallurgy of the alloys as shown in Fig. 1.5 (reproduced) [1].

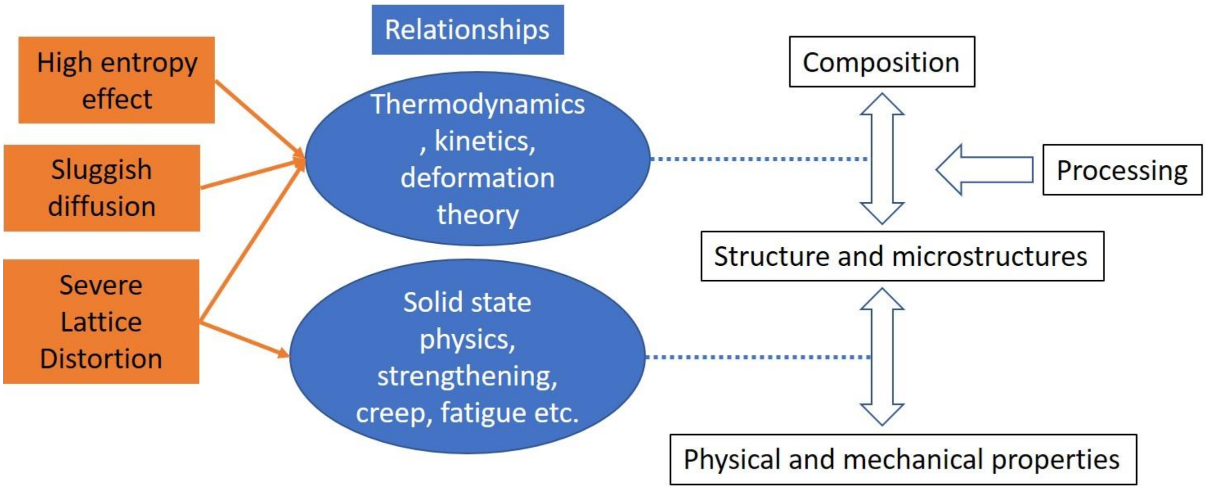

Figure 1.5 The physical metallurgy influenced by the core effect of HEAs [1]

(a) High entropy effect

This is the most important thermodynamic effect HEAs which inhibit the formation of many kinds of stoichiometric compounds which are ordered and brittle in nature. Instead, the high entropy due to configuration promotes formation of stable random solid solutions following the Gibbs free energy law (G=H – T*S). It also reduces the number of phases which can otherwise be formed by following the Gibbs' phase rule. The proportion of mixing enthalpy in HEAs for unlike atomic pairs for solution phase reduces the enthalpy for solid solutions and therefore higher entropy effect is necessary for formation of random solid solutions so that the Gibbs free energy is reduced in equilibrium state. In addition to that, size difference effect as discussed in the previous section of phase formation it was found that random solid solution formation is mostly formed in case of low atomic difference, small enthalpy of mixing and large values of entropy. Thus, high entropy helps inf formation of lower number of stable phase and random solid solution which are advantageous for applications [1,5].

(b) Severe Lattice Distortion

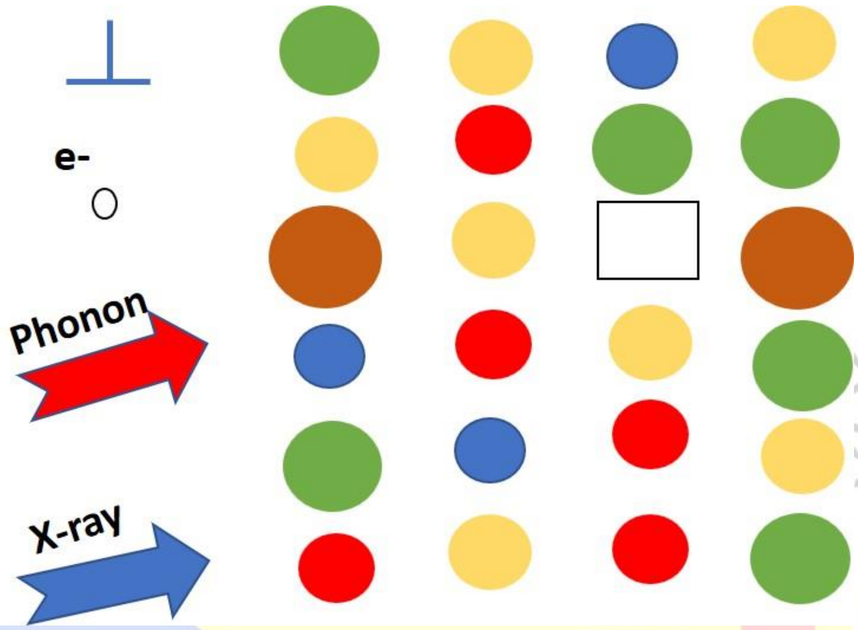

Figure 1.6 Schematic diagram showing the severely distorted lattice and the various interactions with dislocations, electrons, phonons and x-ray beam

Due to the difference in size every atom in a multicomponent alloy system suffers from internal stress and lattice strain as shown in Fig 1.6. Furthermore, the different bonding energies and crystal structure tendencies causes added lattice strain due to unsymmetrical bindings and bonding structure affecting the atomic position from site to site. The high lattice distortion increases the hardness, reduces the thermal diffusivities and lowers the electrical conductivities [1,5].

(c) Sluggish Diffusion Effect

The partitioning of composition for phases require complementing diffusion of many different kinds of atoms and with limited vacancy concentration in HEAs substitutional diffusion becomes extremely difficult. The movement of a vacancy or atom occurs through a fluctuated path or slow diffusion or higher activation energy resulting in diffusional activities being slower than conventional alloys in cases of HEAs. The slow diffusion rate in HEAS increases the recrystallization temperature, precipitation hardening becomes easier, slower grain growth and increased creep resistance [1,5].

(d) Cocktail effect

This was proposed by Prof. S Ranganathan and it talks about the alloy pleasures in alloy development where there is overall enhancement of the properties of the HEAs with contribution from grain morphology, grain size distribution, grain and phase boundaries, and properties of each constituting phase [41].

1.2.2 Multi-Phase/ Dual- Phase AlCoCrFeNi system of High Entropy Alloys

Wide range of research have been carried out on single-phase, HEA such as face-centred cubic (FCC) alloys; $Al_{0.1}$CoCrFeNi [50] and CoCrFeMnNi [51], and body-centered cubic (bcc) alloys; AlCoCrFeNiTi_x [25], NbMoTaW [52], TaNbHfZrTi [53] due to their simple crystal structure and excellent tensile or compression strength. Several HEAs like AlCoCrFeNiMox and AlCoCrFeNiTix displayed fracture strengths of close ~4 GPa [26] and yield strengths of ~2.5 GPa [25,54]. The bcc based HEAs comprising refractory elements VnbMoTaW [55] and ordered HEA systems primarily containing the B2 phase, such as AlCoCrFeNi [56], showed yield stress of ~1250 MPa under room temperature conditions.

Of all HEAs, AlCoCrFeNi system of HEAs are the most extensively studied as can be gauged from published literature. However, single phase FCC HEAs of AlCoCrFeNi system exhibits low strength with exceptional ductility. $Al_{0.1}$CoCrFeNi and $Al_{0.3}$CoCrFeNi possessed yield strengths lower than 200 MPa [14,22]. On the contrary, BCC based HEAs of AlCoCrFeNi system exhibited high strengths at the expense of ductility. Therefore, there was a gradual shift in the interest of the research fraternity to shift towards a more balanced strength-ductility multiphase HEA alloy design, where both the load bearing capacity as well as good toughness for forming into various shapes are addressed. Literatures have shown that dual-phase HEA like $Al_{0.5}CoCrFeNi$ with dendritic morphology displayed yield strength close to 1294 MPa with respectable ductility of ~6% [57]. Dual-phase HEAs with lamellar structures with BCC/B2 along with FCC like $Al_{0.6}CoCrFeNi$ and $Al_{0.7}CoCrFeNi$ exhibited strengths of close to 964 MPa and 1076 MPa with minimum loss of ductility [29,58]. Other eutectic or near eutectic HEAs having FCC and BCC like $Al_{0.9}CoCrFeNi_{2.1}$ displayed yield strength of 645 MPa with low ductility of 6.9% in as -cast condition [59]. Besides, HEAs also have the tendencies of phase separation, formation of secondary phase, ordering phase precipitates resulting out of competition between configurational entropy at high temperatures with enthalpy of mixing at lower temperatures. This ultimately results in the formation of more than a single phase after the solidification is complete.

As mentioned, the applicability in industries with stable defect structures, consistent microstructures and mechanical properties is a challenging aspect of HEAs. HEAs which breaks the compositional barrier of traditional conventional alloys needs to accentuate this hope and activate its full potential through their consistency of performance. In addition, the large-scale production of HEAs at an large industrial scale are quite limited due bad liquidity of the HEA melts and castability of HEAs. However, Licavoli et al made the first attempt at processing HEAs in mass scale instead of small ingots approaching the size of 8 kg by vacuum arc melting of single-phase FCC CoCrFeMnNi [10]. The alloy showed promising with formation of some secondary phase in the form of precipitates. Thereafter, attempt was made to fabricate eutectic HEAs at a large scale of 2.5 kg by Lu *et al.* [9]and were very successful. Recently, Kumar *et al.* in 2022 published a paper on attempting industrial scale production of

HEAs of the scale of 25 kg for AlCoCrFeNi system of HEAs and achieved promising results while comparing the large alloy to lab scale production [60]. Thus, a need for upscaling the size of production of multiphase/dual-phase HEAs due to their ease of casting than single phase and higher probability of meeting industry applications with improved strength ductility trade-off is essential.

1.2.3 Thermo-Mechanical Processing and Severe Plastic Deformation of High Entropy Alloy

In general, as-cast alloys possess casting defects, coarse grains with low strength and rapid solidification to avoid phase separation and elemental segregation resulting in residual thermal stresses. In order to remove these defects, several thermo-mechanical processing is conducted on HEAs that have resulted in significant improvement in the overall mechanical properties of the HEAs. Grain refinement through cold rolling followed by solutionising and annealing in some HEAs. $Al_{0.1}CoCrFeNi$ and $Al_{0.3}CoCrFeNi$ after cold rolling alone or combination of cold rolling followed by post processing have shown their yield strengths increase to 749 MPa and 1037 MPa respectively at the expense of significant ductility [23,61]; In addition, in CoCrFeMnNi due their sluggish diffusion rates resulting in high recrystallization temperature (0.62 T_m) and grain coarsening during annealing affects the overall microstructural evolution of the HEA [32]. Severe plastic deformation (SPD) techniques like high pressure torsion (HPT) and equal channel angular pressing (ECAP) combined with annealing have proven to be effective strengthening mechanisms[32,33]. In addition to deformation by slip, the low SFE alloys under SPD technique have exhibited displacive lattice transformation or transformation induced plasticity (TRIP) effect resulting in superior strain hardening properties and enhanced strength and hardness [62–64]. Pioneering work on TRIP assisted dual-phase FCC-HCP based high iron metastable HEA

$Fe_{80-x}CoCrMn_x$ with non-equimolar composition were carried out by Li *et al.* though cold rolling route and named it TRIP-DP-HEA [34,35]. Despite the advantages of the above mentioned SPD processes, these processes are slow as they require post process treatment and cannot be used for mass production [32,33].

Friction stir welding/friction stir processing (FSW/FSP) is a cost effective, a highly efficient process in production and a fast SPD technique that can be used for strengthening HEAs in large scale. FSP is a solid-state friction-based approach between a non-consumable tool and a base metal to alter microstructure, stress distribution and strength through locally heating at high temperature combined with plastically deformed with large strain, high effective strain rate and material transfer [32,33,62,65]. FSP process also retains the solid strengthening of the HEAs and also effectively removes the coarser dendritic structure of the as- cast alloy as shown in Fig. 1.7 (*permission sought*) [33,62].

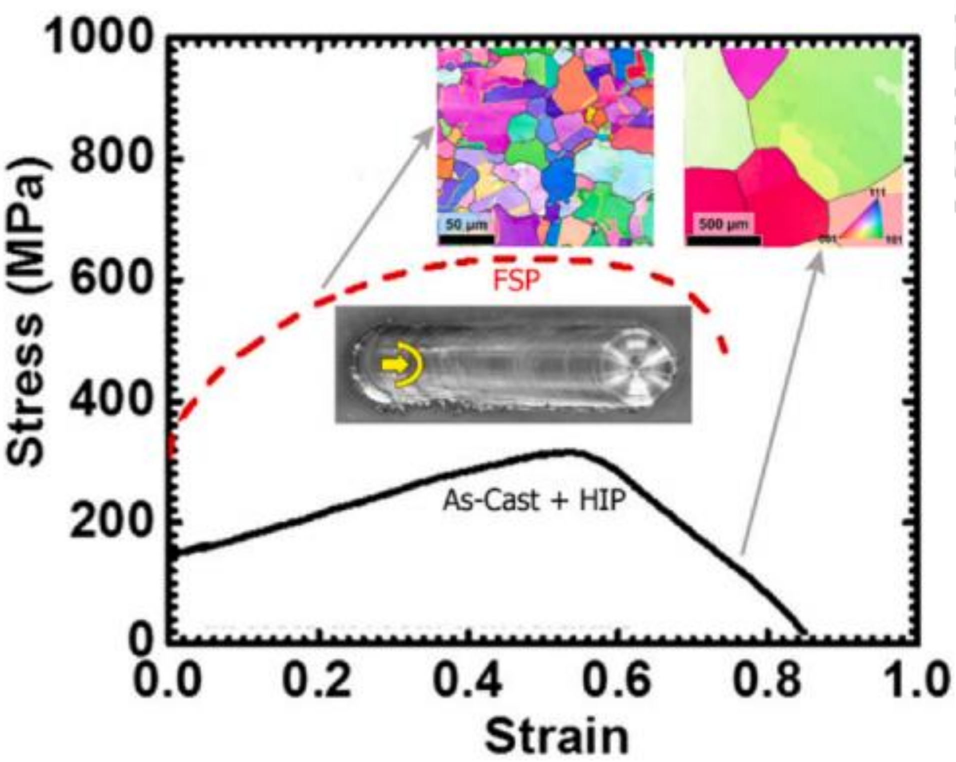

Figure 1.7 FSP of $Al_{0.1}CoCrFeNi$ showing grain refinement and improvement of mechanical properties in the HEA [65]

Subsequently, FSP has become an effective SPD method for not only grain refinement but also to realise the advantages of TRIP effect in HEA [32,34–38]. Multi-pass FSP of DP-5Si-HEA showed an improvement of improvement of more than 600 MPa than DP-HEA, however FSP of DP-HEA could improve its strength by only 100 MPa [36,66]. Majority of the studies related to TRIP assisted HEAs through FSP works focussed on displacive lattice phenomenon related to transformation of FCC (γ) to HCP (ε) phase (Fig.1.8 (*permission sought*)) [63,66,67]. Therefore, further research on the effects of TRIP assisted dual-phase HEA from FCC phase to BCC and deformation mechanics at high strain rate needs to be understood in detail.

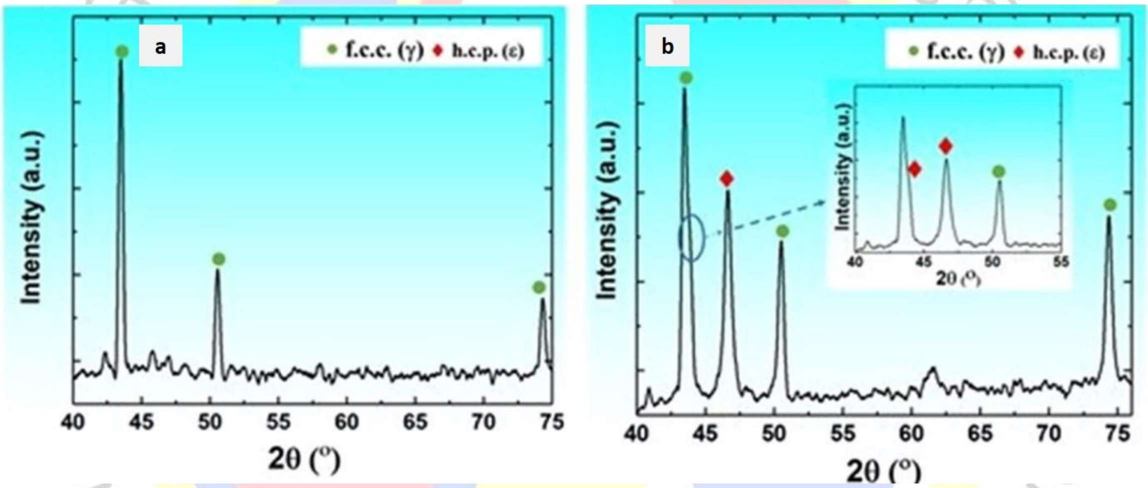

Figure 1.8 The resulting TRIP effect after friction stir processing of DP-5Si-HEA [66]

1.2.4 High Strain Rate Deformation

Deformation behaviour of a materials under an external load depends on the type of loading (tension or compression or bending or torsion), the nature of loading (monotonic or cyclic), operating temperature and the strain rate. Therefore, the strain rate is an important factor in controlling the material properties and its response to external load. The strain rate is generally defined as $\dot{\varepsilon} = \frac{d\varepsilon}{dt}$. The different strain rate range employed for mechanical testing are listed in Table 1.1.

Table 1.1 Different Mechanical Testing categories as per strain rates

Tests	Strain rate range, s^{-1}
Creep Tests	10^{-8} to 10^{-5}
Quasi-static tests	10^{-5} to 10^{-1}
Dynamic tests	10^{-1} to 10^{4}
Ballistic tests	10^{5} to 10^{8}

The most important parameter determining the influence of strain rate on any material is its strain rate sensitivity (SRS) parameter m. This strain rate sensitivity can be determined from the plastic flow curves of a material performed at different strain rates or from strain jump tests where the strain is periodically changed at intervals. The strain rate sensitivity m is generally derived from the extended Hollomon equation given below:

$$\sigma = k\varepsilon^{n}\dot{\varepsilon}^{m} \tag{1.8}$$

A positive strain sensitivity value represents the increase in flow stress with the increase in strain rate as exhibited by metallic materials like iron, aluminium, steel etc. Negative strain rate sensitivity is the decrease in the flow stress of a material with the increase in the rate of loading and such negative strain rate sensitivity materials like nanostructured aluminium and materials exhibiting dynamic strain aging.

Several testing techniques are capable of achieving the above-mentioned strain rate categories. The conventional quasi static tests are carried out in servo electric or servo `strain rates of the up to 10^{2} s^{-1} special servo hydraulic testing systems are now designed for the required cross head speed. Dynamic tests are performed in Split Hopkinson pressure bar (SHPB) or Kolsky bar where the strain ranges between 10^{2} to 10^{3} s^{-1}. Beyond these strain rates to attain extremely high level of strain rates Taylor impact and shock wave flyer techniques are employed. The fundamental distinction in the which separates high strain rate deformation from that of quasi static deformation is the inertia and wave propagation become very significant at high strain rates[20,68]. The schematic of the different factors under different strain rate regimes are shown in Fig 1.9. In high strain rate loading, particularly in split Hopkinson system strain rate and stress are derived from different wave interactions during the impact.

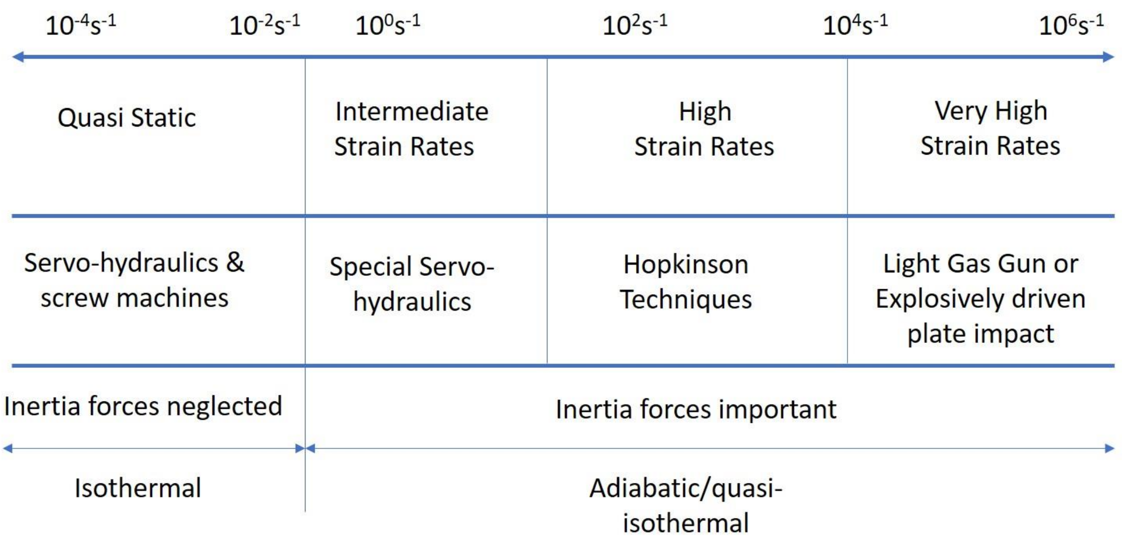

Figure 1.9 Schematic of different strain rate regimes and the effects that come under each regime

Hopkinson pressure bar is the most important apparatus for uniaxial compression testing of materials at high strain rate loading. Subsequent modifications of the apparatus have now facilitated the high strain rate tension and torsion testing.

The specimen is sandwiched between two well machined bars. The bars remain elastic through the experiment while the large plastic strains can be recorded in the specimen. The dynamic loading is triggered by a striker bar which exerts pressure by directly striking the input bar which eventually causes the deformation in the specimen. The elastic wave analysis theory involving strain, strain rate and stress derived from the elastic strains of the bars is given by the following equations[58]:

$$\sigma(t) = \frac{A.E.\varepsilon_t}{A_s} \tag{1.9}$$

$$\frac{\partial \varepsilon}{\partial t} = \frac{2. C_b. \varepsilon_r}{l_s} \quad 1.10$$

, where $\sigma(t)$ is the stress in the specimen, A is the areas of the cross-sectional area of the bar, E is the elastic of modulus of the bars, ε_t is the strain pulse transmitted from the output bar, ε_r is the strain pulse transmitted from the specimen and the measured in the input bar, $\frac{\partial \varepsilon}{\partial t}$ is the specimen strain rate, C_b is the elastic wave speed of the bar material and l_s is the specimen length. This analysis is simple and same for all cases of loading including tension and torsion. The simplicity of specimen geometry is the major advantage of SHPB. Mostly cylindrical samples are used for conducting SHPB compression tests. In addition, rectangular button is used for compression under SHPB compression test.

1.2.5 Micro-Mechanisms of High Entropy Alloys Under High Strain Rate

The dislocation generation and their rearrangement into substructures under mechanical loading primarily determines the controlling deformation mechanisms. A range of substructures like deformation bands, stacking fault-stacking fault interactions, deformation twins, adiabatic shear bands etc. are formed in HEAs under high strain rate. In general, single FCC phase CoCrFeMnNi system and AlCoCrFeNi system of high entropy alloys possess low stacking fault energy which results formation of profuse deformation twins under high strain rate and excellent strain hardening [14,22,24]. The BCC based HEAs exhibited low strain rate sensitivity and low strain hardening even under high strain rate loading with formation of micro-cracks in certain cases[25,26]. The dual-phase HEAs having FCC phase and BCC phase under dynamic loading also forms deformation twins near grain boundaries or interphase boundaries and heavy dislocation pile up at the interphase. $Al_{0.3}CoCrFeNi$ single phase HEA showed remarkable shear resistance under high strain rate and strain rate sensitivity. However, the overall strength of the alloy was quite low [14]. Some dual-phase HEAs with eutectic or near eutectic composition are now being experimented under dynamic loading and they have yielded excellent results. Precipitation hardened by L12 nano-precipitate proved to be an outstanding way of increasing strength without hampering the strain rate sensitivity of the alloy as was examined in $Al_{0.7}CoCrFeNi$ [69]. Some of the HEAs deformed at high strain rate are highlighted in Table

Table 1.2 Key findings of high entropy alloys under high strain rate loadings

SL No	High Entropy Alloy	Preliminary Information	Findings under High Strain Rate Loading	Ref.
1	$Al_{0.1}CrFeCoNi$	Single phase FCC	- SRS: 0.026 - Profuse deformation Twinning and secondary nano twinning due to very low stacking fault energy at high strain rate loading.	[22]
2	$Al_{0.1}CrFeCoNi$	Single Phase FCC Conditions: -As-cast -20% Cold rolled -40% Cold rolled -40% Cold rolled +550°C/24h -40% Cold rolled +620°C/50h -40% Cold rolled +700°C/5h -40% Cold rolled	-SRS: - As-cast: 0.017 - 20% Cold rolled: 0.09 - 40% Cold rolled: 0 - 40% Cold rolled +550°C/24h: 0.017 - 40% Cold rolled +620°C/50h: 0.014 - 40% Cold rolled +700°C/5h: 0.008 - 40% Cold rolled +800°C/1h: 0.004	[61]

		+800°C/1h	Recovery cases: -The SRS remained intact due to recovery at 550°C/24h and excellent strain hardening due to formation of deformation twins and dislocation cells at high strain rate. Recrystallization cases: -The introduction of new grains at 40% Cold rolled +700°C/5h which increases long range obstacles reducing the SRS but increased ductility and work hardening.	
3	$Al_{0.3}$CrFeCoNi	Single phase FCC Arc melted	-SRS: 0.053 -High strain hardening due formation of mechanical twining. Forest dislocation and solid solution hardening. -The modest thermal softening during high strain rate gave rise to excellent resistance to shear localization.	[14]
4.	$Al_{0.3}$CrFeCoNi	Homogenised Conditions: -As-cast -20% Cold rolled -50% Cold	-SRS -50% Cold rolled+1150°C/1h:0.063 -50% Cold rolled + 1150°C/1h + 700°C/50h:0.054 -50% Cold rolled + 1150°C/1h +	[23]

		rolled+1150°C/1h -50% Cold rolled + 1150°C/1h + 700°C/50h -50% Cold rolled + 1150°C/1h + 550°C/150h -50% Cold rolled + 700°C/50h -50% Cold rolled + 550°C/150h -50% Cold rolled	550°C/150h:0.044 -50% Cold rolled + 700°C/50h:0.022 -50% Cold rolled + 550°C/150h:0.017 -50% Cold rolled:0.006 -An extraordinarily large range of SRS observed (0.006-0.063). -High work hardening rate of 2200 MPa under dynamic loading. -All cases of precipitation hardening reduced the SRS marginally.	
5	$AlCrCuFeNi_2$	Dual- Phase (FCC+ BCC) Arc Melted	-SRS: 0.00142 -Shear band of 5 µm formed at quasi static loading and quasi-cleavage fracture observed under high strain rate loading.	[70]
6	AlCoCrFeNiTix	BCC phase Arc Melted x = (0.2, 0.4 and 0.6)	-SRS At x = 0.20: 0.0084 At x = 0.4: 0.00026 At x = 0.6: 0.00022 -The HEAs exhibited higher fracture strains than bulk metallic glass owing to its high solid solution strengthening and strong	[25]

			dislocation interactions.	
7	$AlCoCr_{1.5}Fe_{1.5}NiTi_{0.5}$	BCC/B2 phase Arc Melted	-SRS: 0.0079 -No work hardening increase in both cases quasi and dynamic	[26]
8	CoCrFeMnNi	Single phase FCC Spark plasma sintering	-Formation of deformation bands, shear bands at high strain rates - Micro voids and cracks along grain boundaries causing serration in stress strain curve.	[51]
9	CoCrFeMnNi	Vacuum Induction Melted Single Phase FCC	- SRS: 0.028 -Deformation twins formed at lower strain under dynamic loading than quasi static loading. -Dynamic recrystallization leading to grain refinement near localized shear zones (thermal softening) (at high plastic strain) under dynamic loading.	[24]
10	$Al_{0.7}CoCrFeNi$	Dual-Phase (FCC+BCC/B2) Arc melted Conditions: -30% cold rolled -30% cold rolled + homogenised +	-30% cold rolled exhibited the worst work hardening rate but highest strength compared to the other three conditions. -580 °C/24 h exhibited good work hardening due to L12 phase as dislocation storage and good strength due to hierarchical	[58]

		1100 °C/5 min -30% cold rolled + homogenised + 1100 °C/5 min +580 °C/24 h	microstructures.	
11	$Al_{0.7}CoCrFeNi$	Dual-phase (FCC+BCC/B2) Arc melting + homogenised 1150°C/1 min Conditions: -30% Cold rolled + 1100°C/5min -30% Cold rolled + 1100°C/5min+580°C/24 h	-SRS -30% Cold rolled + 1100°C/5min: 0.018 -30% Cold rolled + 1100°C/5min+580°C/24 h: 0.017 30% Cold rolled + 1100°C/5min -Under high strain rate nano twins are formed along with heavy dislocation pile up at the interphase boundary. -30% Cold rolled + 1100°C/5min+580 °C/24 h:FCC/ L12(precipitate)+BCC/B2 - Similar substructures like deformation twin in the FCC phase and highly faulted BCC/B2 were observed at high strain rate deformation. -SRS does not substantially decrease due L12 phase evolved after 30% Cold rolled + 1100°C/5min+580°C/24 h because they are coherent and thermally active.	[69]

12	$Al_{0.3}CoCrFeNi$ $Al_{0.7}CoCrFeNi$	$Al_{0.3}CoCrFeNi$ (single-phase FCC) $Al_{0.7}CoCrFeNi$ (dual-phase FCC+BCC) Arc melting Conditions: - $Al_{0.3}CoCrFeNi$ -0.063(homo) -0.054 (ppt) $Al_{0.7}CoCrFeNi$ -0.018(homo) -0.017 (ppt)	SRS: $Al_{0.3}CoCrFeNi$ -0.063(homo) -0.054 (ppt) $Al_{0.7}CoCrFeNi$ -0.018(homo) -0.017 (ppt) -$Al_{0.3}CoCrFeNi$ - profuse twining $Al_{0.7}CoCrFeNi$ -Quasi no twin only dislocation pile up at interphase boundary and forest dislocation at interior -Dynamic nano twinning (fine lamellar inhibit twin and higher SFE) and disrupted lamellar structure -L12 nano-ppt. acts like short range barrier and does not lower SRS too much	[28]
13	$Al_{0.6}CrFeCoNi$	Dual-phase (FCC+BCC)	-SRS:0.029 Dislocation cell walls and dislocation tangles in quasi -Sparse deformation twins under high strain rate loading can be observed	[29]

			Strength ductility balanced due to FCC BCC and deformation substructures	
14	AlCoFeCrNi	0.021	Fractured in both cases quasi cleavage and dislocation slip in fracture surface at quasi molten droplets under HSR	[68]
15	AlxCrMnFeCoNi (0,0.4,0.6)	Arc melting x = 0 (FCC phase) x = 0.4 (FCC) Arc Melted and Drop Cast	-SRS: x=0.4: 0.039 x=0.6: 0.024 -Profuse GND at interphase so excellent strain hardening dislocation heavy pile up comparable to twin boundary B2 phase has negligible effect on SRS. -SRS decreased due to long range interphase yet better WHR and WH than single phase HEAs	[72]
16	$Cr_{26}Mn_{20}Fe_{20}Co_{20}Ni_{14}$	Single phase FCC Vacuum Induction Melting Forged at 1273 K + 1273 K/8 h	-SRS (Dynamic): 0.076 -Strain hardening exponent increased with increasing strain rate at high strain rate. -Stacking fault reactions increased with increasing strain rates and eventually formed stacking twins at 3000 s^{-1}.	[73]

17	$Al_{0.5}CoCrFeNi$	Dual- phase (FCC+BCC/B2) Arc melting Conditions: Hot rolled at 700°C + 1150°C/5min + 700°C/ (x =1,4,20,40,80 h)	-The flow stress corresponding to 0.02% strain under a strain rate of 2000 s^{-1} increased with increasing hours of heat treatment as the percentage of B2 phase increased in the form of precipitates causing precipitation hardening.	[57]
18	$Co_{11.3}Cr_{20.4}Fe_{22.6}Mn_{21.8}Ni_{23.9}$	Single phase FCC Vacuum Induction Melting	-SRS: 0.048 -Enhanced strain hardening was observed due to formation of deformation bands, dislocation pile-ups near sub-grain grain boundary. - Plausible deformation twins were also observed but not dominant deformation mechanism.	[74]
19	$Al_{1.19}Co_2CrFeNi_{1.81}$	Dual-phase (FCC+BCC/B2) Arc melting	-SRS Quasi: 0.0102 Dynamic: 0.111 Dynamic at cryogenic temperatures:0.17 -Interphase boundary dislocation pile-ups and deformation twins were observed under room temperature high strain rate deformation. -Abundant deformation twins and	[75]

			secondary nano-twins were formed along with Lomer-Cottrell (L-C) locks at high strain deformation at cryogenic temperatures.	
20	$AlCoCrFeNi_{2.1}$	Dual-Phase (FCC+BCC/B2) Preparation: -Drop cast (DC) -Suction cast (SC)	-SRS Drop cast: 0.02 Suction cast: 0.029 -The suction cast condition exhibited higher strain rate hardening than the drop cast sample by forming irregular dislocation cells in the FCC phase during dynamic deformation.	[30]

1.3 Research Gap and Motivation

The following research gaps were identified from previous literature on high entropy alloys and their behaviour under high strain rate loading.

1) High entropy alloys have shown extraordinary mechanical properties but the balance in strength and ductility is still a major constraint.
2) Although high entropy alloys have shown excellent strain hardening properties under high strain rate loading, studies related to high strain rate loading of dual-phase high entropy alloys are not extensively explored.
3) Another major challenge is the scalability of high entropy alloys due to their poor castability.
4) Studies related to high strain rate deformation of TRIP-assisted high entropy alloys processed via friction stir processing have not been published.

These research gaps emphasized the importance of study on dynamic deformation behaviour of dual-phase high entropy alloys and motivated to pursue the thesis work in this field.

1.4 Objectives

The primary aim of this thesis work is to develop a novel dual-phase high entropy alloy at a large scale in an industrial environment and to understand the deformation behaviour of the alloy under dynamic loading conditions to explore the possibilities of using the alloy for high strain rate applications. To achieve this aim, the following objectives are pursued.

- To develop a dual-phase high entropy alloy comprising of FCC and BCC phases at large scale through proper processing technique.
- To investigate the mechanical properties, strain rate sensitivity and deformation behaviour under both quasi-static and dynamic loading.
- To investigate the effects of the cooling rate of solidification on the mechanical properties, strengthening contributions, strain rate sensitivity and deformation mechanisms by comparing the rapidly cooled lab-scale alloy with the large-scale processed alloy.
- Finally, to enhance the properties of the large-scale processed alloy through friction stir processing and to study the strength, strengthening contributions, strain rate sensitivity and deformation behaviour of the alloy after processing.

1.5 Organization of the thesis

This thesis contains 7 chapters and they are summarized below as:

- Chapter 1 starts with the brief introduction of the background and significance of the thesis work. The thesis also discusses the relevant literature related to the alloy system, high strain rate test techniques and deformation mechanisms of the alloy system under high strain rate loading followed by the research gap and motivation. Finally, the chapter ends with the primary aim and the objectives of the work
- Chapter 2 discusses the design considerations in developing a dual-phase high entropy alloy and the different processing routes undertaken during the course of carrying out the study. The chapter also discusses about the different experimental methodologies involved in the study.
- Chapter 3 compares the quasi-static mechanical properties and deformation behaviour of industrially melted as-cast alloy with the rapidly cooled lab-scale alloy.
- Chapter 4 investigates the deformation mechanisms involved under dynamic loading of the industrially melted as-cast alloy.
- Chapter 5 involves the study of strain rate sensitivity and the study of deformation behaviour of the rapidly cooled small-scale suction-cast alloy under dynamic loading.
- Chapter 6 investigates the effects of friction stir processing on the mechanical properties of the industrially melted large-scale alloy under a wide range of strain rates. The chapter also discusses the deformation mechanisms involved in the friction stir processed alloy under both quasi-static and dynamic loadings.
- Chapter 7 concludes the major findings of the thesis work and suggests the scope of future work.

References

[1] J.W. Yeh, Alloy design strategies and future trends in high-entropy alloys, JOM. 65 (2013) 1759–1771. https://doi.org/10.1007/s11837-013-0761-6.

[2] M.H. Tsai, J.W. Yeh, High-entropy alloys: A critical review, Mater. Res. Lett. (2014). https://doi.org/10.1080/21663831.2014.912690.

[3] D.B. Miracle, O.N. Senkov, A critical review of high entropy alloys and related concepts, Acta Mater. 122 (2017) 448–511. https://doi.org/10.1016/j.actamat.2016.08.081.

[4] C.J. Tong, M.R. Chen, S.K. Chen, J.W. Yeh, T.T. Shun, S.J. Lin, S.Y. Chang, Mechanical performance of the AlxCoCrCuFeNi high-entropy alloy system with multiprincipal elements, in: Metall. Mater. Trans. A Phys. Metall. Mater. Sci., 2005. https://doi.org/10.1007/s11661-005-0218-9.

[5] E.J. Pickering, N.G. Jones, High-entropy alloys: a critical assessment of their founding principles and future prospects, Int. Mater. Rev. 61 (2016) 183–202. https://doi.org/10.1080/09506608.2016.1180020.

[6] Y. Lu, Y. Dong, H. Jiang, Z. Wang, Z. Cao, S. Guo, T. Wang, T. Li, P.K. Liaw, Promising properties and future trend of eutectic high entropy alloys, Scr. Mater. 187 (2020) 202–209. https://doi.org/10.1016/j.scriptamat.2020.06.022.

[7] L. Han, X. Xu, L. Wang, F. Pyczak, R. Zhou, Y. Liu, A eutectic high-entropy alloy with good high-temperature strength-plasticity balance, Mater. Res. Lett. (2019). https://doi.org/10.1080/21663831.2019.1650130.

[8] Y. Lu, Y. Dong, S. Guo, L. Jiang, H. Kang, T. Wang, B. Wen, Z. Wang, J. Jie, Z. Cao, H. Ruan, T. Li, A promising new class of high-temperature alloys: Eutectic high-entropy alloys, Sci. Rep. 4 (2014) 1–5. https://doi.org/10.1038/srep06200.

[9] Y. Lu, X. Gao, L. Jiang, Z. Chen, T. Wang, J. Jie, H. Kang, Y. Zhang, S. Guo, H. Ruan, Y. Zhao, Z. Cao, T. Li, Directly cast bulk eutectic and near-eutectic high entropy alloys with balanced strength and ductility in a wide temperature range, Acta Mater. 124 (2017) 143–150. https://doi.org/10.1016/j.actamat.2016.11.016.

[10] J.J. Licavoli, M.C. Gao, J.S. Sears, P.D. Jablonski, J.A. Hawk, Microstructure and

Mechanical Behavior of High-Entropy Alloys, J. Mater. Eng. Perform. 24 (2015) 3685–3698. https://doi.org/10.1007/s11665-015-1679-7.

[11] F.J. Wang, Y. Zhang, G.L. Chen, H.A. Davies, Cooling Rate and Size Effect on the Microstructure and Mechanical Properties of AlCoCrFeNi High Entropy Alloy, J. Eng. Mater. Technol. 131 (2009) 034501-1–3. https://doi.org/10.1115/1.3120387.

[12] C.J. Tong, M.R. Chen, S.K. Chen, J.W. Yeh, T.T. Shun, S.J. Lin, S.Y. Chang, Mechanical performance of the AlxCoCrCuFeNi high-entropy alloy system with multiprincipal elements, Metall. Mater. Trans. A Phys. Metall. Mater. Sci. 36 (2005) 1263–1271. https://doi.org/10.1007/s11661-005-0218-9.

[13] X. Yang, S.Y. Chen, J.D. Cotton, Y. Zhang, Phase Stability of Low-Density, Multiprincipal Component Alloys Containing Aluminum, Magnesium, and Lithium, JOM. 66 (2014) 2009–2020. https://doi.org/10.1007/s11837-014-1059-z.

[14] Z. Li, S. Zhao, H. Diao, P.K. Liaw, M.A. Meyers, High-velocity deformation of Al0.3 CoCrFeNi high-entropy alloy: Remarkable resistance to shear failure, Sci. Rep. 7 (2017) 1–8. https://doi.org/10.1038/srep42742.

[15] Z. Tang, O.N. Senkov, C.M. Parish, C. Zhang, F. Zhang, L.J. Santodonato, G. Wang, G. Zhao, F. Yang, P.K. Liaw, Tensile ductility of an AlCoCrFeNi multi-phase high-entropy alloy through hot isostatic pressing (HIP) and homogenization, Mater. Sci. Eng. A. (2015). https://doi.org/10.1016/j.msea.2015.08.078.

[16] M.A. Hemphill, T. Yuan, G.Y. Wang, J.W. Yeh, C.W. Tsai, A. Chuang, P.K. Liaw, Fatigue behavior of Al 0.5CoCrCuFeNi high entropy alloys, Acta Mater. 60 (2012) 5723–5734. https://doi.org/10.1016/j.actamat.2012.06.046.

[17] Q. Wang, Y. Ma, B. Jiang, X. Li, Y. Shi, C. Dong, P.K. Liaw, A cuboidal B2 nanoprecipitation-enhanced body-centered-cubic alloy Al0.7CoCrFe2Ni with prominent tensile properties, Scr. Mater. 120 (2016) 85–89. https://doi.org/10.1016/j.scriptamat.2016.04.014.

[18] F. He, Z. Wang, Q. Wu, J. Li, J. Wang, C.T. Liu, Phase separation of metastable CoCrFeNi high entropy alloy at intermediate temperatures, Scr. Mater. 126 (2017) 15–19. https://doi.org/10.1016/j.scriptamat.2016.08.008.

[19] X. Sun, Dynamic strength evaluation/crashworthiness of self-piercing riveted joints,

in: Self-Piercing Riveting Prop. Process. Appl., 2014: p. P 56-78. https://doi.org/10.1533/9780857098849.1.56.

[20] M.A. Meyers, Shear Bands: Metallurgical Aspects, 1994. https://books.google.com.au/books?id=WoEDHtRTOhoC.

[21] A. Das, S. Tarafder, S. Sivaprasad, D. Chakrabarti, Influence of microstructure and strain rate on the strain partitioning behaviour of dual phase steels, Mater. Sci. Eng. A. 754 (2019) 348–360. https://doi.org/10.1016/j.msea.2019.03.084.

[22] N. Kumar, Q. Ying, X. Nie, R.S. Mishra, Z. Tang, P.K. Liaw, R.E. Brennan, K.J. Doherty, K.C. Cho, High strain-rate compressive deformation behavior of the Al0.1CrFeCoNi high entropy alloy, Mater. Des. 86 (2015) 598–602. https://doi.org/10.1016/j.matdes.2015.07.161.

[23] S. Gangireddy, B. Gwalani, K. Liu, R. Banerjee, R.S. Mishra, Microstructures with extraordinary dynamic work hardening and strain rate sensitivity in Al0.3CoCrFeNi high entropy alloy, Mater. Sci. Eng. A. 734 (2018) 42–50. https://doi.org/10.1016/j.msea.2018.07.088.

[24] J.M. Park, J. Moon, J.W. Bae, M.J. Jang, J. Park, S. Lee, H.S. Kim, Strain rate effects of dynamic compressive deformation on mechanical properties and microstructure of CoCrFeMnNi high-entropy alloy, Mater. Sci. Eng. A. 719 (2018) 155–163. https://doi.org/10.1016/j.msea.2018.02.031.

[25] Z.M. Jiao, S.G. Ma, M.Y. Chu, H.J. Yang, Z.H. Wang, Y. Zhang, J.W. Qiao, Superior Mechanical Properties of AlCoCrFeNiTix High-Entropy Alloys upon Dynamic Loading, J. Mater. Eng. Perform. 25 (2016) 451–456. https://doi.org/10.1007/s11665-015-1869-3.

[26] T.W. Zhang, Z.M. Jiao, Z.H. Wang, J.W. Qiao, Dynamic deformation behaviors and constitutive relations of an AlCoCr1.5Fe1.5NiTi0.5 high-entropy alloy, Scr. Mater. 136 (2017) 15–19. https://doi.org/10.1016/j.scriptamat.2017.03.039.

[27] L. Ma, C. Li, Y. Jiang, J. Zhou, L. Wang, F. Wang, T. Cao, Y. Xue, Cooling rate-dependent microstructure and mechanical properties of AlxSi0.2CrFeCoNiCu1−xhigh entropy alloys, J. Alloys Compd. 694 (2017) 61–67. https://doi.org/10.1016/j.jallcom.2016.09.213.

[28] S. Gangireddy, B. Gwalani, V. Soni, R. Banerjee, R.S. Mishra, Contrasting mechanical behavior in precipitation hardenable AlXCoCrFeNi high entropy alloy microstructures: Single phase FCC vs. dual phase FCC-BCC, Mater. Sci. Eng. A. 739 (2019) 158–166. https://doi.org/10.1016/j.msea.2018.10.021.

[29] L. Wang, J.W. Qiao, S.G. Ma, Z.M. Jiao, T.W. Zhang, G. Chen, D. Zhao, Y. Zhang, Z.H. Wang, Mechanical response and deformation behavior of Al0.6CoCrFeNi high-entropy alloys upon dynamic loading, Mater. Sci. Eng. A. 727 (2018) 208–213. https://doi.org/10.1016/j.msea.2018.05.001.

[30] M. Hu, K. Song, W. Song, Dynamic mechanical properties and microstructure evolution of AlCoCrFeNi2.1 eutectic high-entropy alloy at different temperatures, J. Alloys Compd. 892 (2022) 162097. https://doi.org/10.1016/j.jallcom.2021.162097.

[31] L. Wang, J.W. Qiao, S.G. Ma, Z.M. Jiao, T.W. Zhang, G. Chen, D. Zhao, Y. Zhang, Z.H. Wang, Mechanical response and deformation behavior of Al0.6CoCrFeNi high-entropy alloys upon dynamic loading, Mater. Sci. Eng. A. (2018). https://doi.org/10.1016/j.msea.2018.05.001.

[32] S.Y. Anaman, S. Ansah, H.H. Cho, M.G. Jo, J.Y. Suh, M. Kang, J.S. Lee, S.T. Hong, H.N. Han, An investigation of the microstructural effects on the mechanical and electrochemical properties of a friction stir processed equiatomic CrMnFeCoNi high entropy alloy, J. Mater. Sci. Technol. 87 (2021) 60–73. https://doi.org/10.1016/j.jmst.2021.01.043.

[33] J. Zhang, R. Fu, Y. Li, Y. Lei, L. Guo, H. Lv, J. Yang, Synergistic enhancement in strength and ductility of nitrogen-alloyed CoCrFeMnNi high-entropy alloys via multi-pass friction stir processing, J. Alloys Compd. 927 (2022) 167015. https://doi.org/10.1016/j.jallcom.2022.167015.

[34] Z. Li, C.C. Tasan, K.G. Pradeep, D. Raabe, A TRIP-assisted dual-phase high-entropy alloy: Grain size and phase fraction effects on deformation behavior, Acta Mater. 131 (2017) 323–335. https://doi.org/10.1016/j.actamat.2017.03.069.

[35] Z. Li, K.G. Pradeep, Y. Deng, D. Raabe, C.C. Tasan, Metastable high-entropy dual-phase alloys overcome the strength-ductility trade-off, Nature. 534 (2016) 227–230. https://doi.org/10.1038/nature17981.

[36] S.S. Nene, K. Liu, M. Frank, R.S. Mishra, R.E. Brennan, K.C. Cho, Z. Li, D. Raabe, Enhanced strength and ductility in a friction stir processing engineered dual phase high entropy alloy, Sci. Rep. 7 (2017) 1–7. https://doi.org/10.1038/s41598-017-16509-9.

[37] N. Li, C.L. Jia, Z.W. Wang, L.H. Wu, D.R. Ni, Z.K. Li, H.M. Fu, P. Xue, B.L. Xiao, Z.Y. Ma, Y. Shao, Y.L. Chang, Achieving a High-Strength CoCrFeNiCu High-Entropy Alloy with an Ultrafine-Grained Structure via Friction Stir Processing, Acta Metall. Sin. (English Lett. 33 (2020) 947–956. https://doi.org/10.1007/s40195-020-01037-9.

[38] T. Wang, M. Komarasamy, S. Shukla, R.S. Mishra, Simultaneous enhancement of strength and ductility in an AlCoCrFeNi2.1 eutectic high-entropy alloy via friction stir processing, J. Alloys Compd. 766 (2018) 312–317. https://doi.org/10.1016/j.jallcom.2018.06.337.

[39] J.W. Yeh, S.K. Chen, S.J. Lin, J.Y. Gan, T.S. Chin, T.T. Shun, C.H. Tsau, S.Y. Chang, Nanostructured high-entropy alloys with multiple principal elements: Novel alloy design concepts and outcomes, Adv. Eng. Mater. 6 (2004) 299–303. https://doi.org/10.1002/adem.200300567.

[40] B. Cantor, I.T.H. Chang, P. Knight, A.J.B. Vincent, Microstructural development in equiatomic multicomponent alloys, Mater. Sci. Eng. A. 375–377 (2004) 213–218. https://doi.org/10.1016/j.msea.2003.10.257.

[41] S. Ranganathan, Alloyed pleasures: Multimetallic cocktails, Curr. Sci. 85 (2003) 1404–1406.

[42] J. Chen, X. Zhou, W. Wang, B. Liu, Y. Lv, W. Yang, D. Xu, Y. Liu, A review on fundamental of high entropy alloys with promising high–temperature properties, J. Alloys Compd. 760 (2018). https://doi.org/10.1016/j.jallcom.2018.05.067.

[43] B.S. Murty, J.W. Yeh, S. Ranganathan, P.P. Bhattacharjee, High-entropy alloys: basic concepts, in: High-Entropy Alloy., 2019. https://doi.org/10.1016/b978-0-12-816067-1.00002-3.

[44] Y. Zhang, X. Yang, P.K. Liaw, Alloy design and properties optimization of high-entropy alloys, JOM. (2012). https://doi.org/10.1007/s11837-012-0366-5.

[45] Y. Zhang, Z.P. Lu, S.G. Ma, P.K. Liaw, Z. Tang, Y.Q. Cheng, M.C. Gao, Guidelines

in predicting phase formation of high-entropy alloys, MRS Commun. (2014) 4(2),52-62. https://doi.org/10.1557/mrc.2014.11.

[46] Y. Zhang, Y.J. Zhou, J.P. Lin, G.L. Chen, P.K. Liaw, Solid-solution phase formation rules for multi-component alloys, Adv. Eng. Mater. 10 (2008) 534–538. https://doi.org/10.1002/adem.200700240.

[47] R. Sriharitha, B.S. Murty, R.S. Kottada, Alloying, thermal stability and strengthening in spark plasma sintered AlxCoCrCuFeNi high entropy alloys, J. Alloys Compd. 583 (2014) 419–426. https://doi.org/10.1016/j.jallcom.2013.08.176.

[48] T. Yang, S. Xia, S. Liu, C. Wang, S. Liu, Y. Zhang, J. Xue, S. Yan, Y. Wang, Effects of AL addition on microstructure and mechanical properties of AlxCoCrFeNi High-entropy alloy, Mater. Sci. Eng. A. 648 (2015) 15–22. https://doi.org/10.1016/j.msea.2015.09.034.

[49] C. Li, J.C. Li, M. Zhao, Q. Jiang, Effect of aluminum contents on microstructure and properties of Al xCoCrFeNi alloys, J. Alloys Compd. (2010). https://doi.org/10.1016/j.jallcom.2010.03.111.

[50] N. Kumar, Q. Ying, X. Nie, R.S. Mishra, Z. Tang, P.K. Liaw, R.E. Brennan, K.J. Doherty, K.C. Cho, High strain-rate compressive deformation behavior of the Al0.1CrFeCoNi high entropy alloy, Mater. Des. 86 (2015) 598–602. https://doi.org/10.1016/j.matdes.2015.07.161.

[51] B. Wang, A. Fu, X. Huang, B. Liu, Y. Liu, Z. Li, X. Zan, Mechanical Properties and Microstructure of the CoCrFeMnNi High Entropy Alloy Under High Strain Rate Compression, J. Mater. Eng. Perform. 25 (2016) 2985–2992. https://doi.org/10.1007/s11665-016-2105-5.

[52] Y. Zou, S. Maiti, W. Steurer, R. Spolenak, Size-dependent plasticity in an Nb25Mo25Ta 25W25 refractory high-entropy alloy, Acta Mater. 65 (2014) 85–97. https://doi.org/10.1016/j.actamat.2013.11.049.

[53] M. lei Hu, W. dong Song, D. bo Duan, Y. Wu, Dynamic behavior and microstructure characterization of TaNbHfZrTi high-entropy alloy at a wide range of strain rates and temperatures, Int. J. Mech. Sci. 182 (2020) 105738. https://doi.org/10.1016/j.ijmecsci.2020.105738.

[54] J.M. Zhu, H.M. Fu, H.F. Zhang, A.M. Wang, H. Li, Z.Q. Hu, Microstructures and compressive properties of multicomponent AlCoCrFeNiMox alloys, Mater. Sci. Eng. A. 527 (2010) 6975–6979. https://doi.org/10.1016/j.msea.2010.07.028.

[55] O.N. Senkov, G.B. Wilks, J.M. Scott, D.B. Miracle, Mechanical properties of Nb\textsubscript{25}Mo\textsubscript{25}Ta\textsubscript{25}W\textsubscript{25} and V\textsubscript{20}Nb\textsubscript{20}Mo\textsubscript{20}Ta\textsubscript{20}W\textsubscript{20} refractory high entropy alloys, Intermetallics. 19 (2011) 698–706.

[56] Y.P. Wang, B.S. Li, M.X. Ren, C. Yang, H.Z. Fu, Microstructure and compressive properties of AlCrFeCoNi high entropy alloy, Mater. Sci. Eng. A. 491 (2008) 154–158. https://doi.org/10.1016/j.msea.2008.01.064.

[57] B. Gwalani, T. Torgerson, S. Dasari, A. Jagetia, M.S.K.K.Y. Nartu, S. Gangireddy, M. Pole, T. Wang, T.W. Scharf, R. Banerjee, Influence of fine-scale B2 precipitation on dynamic compression and wear properties in hypo-eutectic Al0.5CoCrFeNi high-entropy alloy, J. Alloys Compd. 853 (2021) 157126. https://doi.org/10.1016/j.jallcom.2020.157126.

[58] S. Gangireddy, B. Gwalani, R. Banerjee, R.S. Mishra, High Strain Rate Response of Al0.7CoCrFeNi High Entropy Alloy: Dynamic Strength Over 2 GPa from Thermomechanical Processing and Hierarchical Microstructure, J. Dyn. Behav. Mater. 5 (2019) 1–7. https://doi.org/10.1007/s40870-018-00178-4.

[59] X. Jin, Y. Liang, J. Bi, B. Li, Enhanced strength and ductility of Al0.9CoCrNi2.1 eutectic high entropy alloy by thermomechanical processing, Materialia. (2020). https://doi.org/10.1016/j.mtla.2020.100639.

[60] J. Kumar, N. Nayan, R.K. Gupta, M. Ramalingam Munisamy, K. Biswas, High Entropy Alloys: Laboratory to Industrial Attempt, Int. J. Met. (2022). https://doi.org/10.1007/s40962-022-00811-y.

[61] S. Gangireddy, L. Kaimiao, B. Gwalani, R. Mishra, Microstructural dependence of strain rate sensitivity in thermomechanically processed Al0.1CoCrFeNi high entropy alloy, Mater. Sci. Eng. A. 727 (2018) 148–159. https://doi.org/10.1016/j.msea.2018.04.108.

[62] A. Sittiho, M. Bhattacharyya, J. Graves, S.S. Nene, R.S. Mishra, I. Charit, Friction stir processing of a high entropy alloy Fe42Co10Cr15Mn28Si5 with transformative characteristics: Microstructure and mechanical properties, Mater. Today Commun. 28 (2021) 102635. https://doi.org/10.1016/j.mtcomm.2021.102635.

[63] S. Bhowmik, J. Zhang, S.C. Vogel, S.S. Nene, R.S. Mishra, B.A. McWilliams, M. Knezevic, Effects of plasticity-induced martensitic transformation and grain refinement on the evolution of microstructure and mechanical properties of a metastable high entropy alloy, J. Alloys Compd. 891 (2022) 161871. https://doi.org/10.1016/j.jallcom.2021.161871.

[64] S. Sinha, S.S. Nene, M. Frank, K. Liu, R.A. Lebensohn, R.S. Mishra, Deformation mechanisms and ductile fracture characteristics of a friction stir processed transformative high entropy alloy, Acta Mater. 184 (2020) 164–178. https://doi.org/10.1016/j.actamat.2019.11.056.

[65] N. Kumar, M. Komarasamy, P. Nelaturu, Z. Tang, P.K. Liaw, R.S. Mishra, Friction stir processing of a high entropy alloy Al0.1CoCrFeNi, Jom. 67 (2015) 1007–1013. https://doi.org/10.1007/s11837-015-1385-9.

[66] S.S. Nene, M. Frank, K. Liu, R.S. Mishra, B.A. McWilliams, K.C. Cho, Extremely high strength and work hardening ability in a metastable high entropy alloy, Sci. Rep. 8 (2018) 1–8. https://doi.org/10.1038/s41598-018-28383-0.

[67] K. Liu, S.S. Nene, M. Frank, S. Sinha, R.S. Mishra, Metastability-assisted fatigue behavior in a friction stir processed dual-phase high entropy alloy, Mater. Res. Lett. 6 (2018) 613–619. https://doi.org/10.1080/21663831.2018.1523240.

[68] C.T. Wang, Y. He, Z. Guo, X. Huang, Y. Chen, H. Zhang, Y. He, Strain Rate Effects on the Mechanical Properties of an AlCoCrFeNi High-Entropy Alloy, Met. Mater. Int. 27 (2021) 2310–2318. https://doi.org/10.1007/s12540-020-00920-5.

[69] B. Gwalani, S. Gangireddy, Y. Zheng, V. Soni, R.S. Mishra, R. Banerjee, Influence of ordered L1 2 precipitation on strain-rate dependent mechanical behavior in a eutectic high entropy alloy, Sci. Rep. 9 (2019) 1–13. https://doi.org/10.1038/s41598-019-42870-y.

[70] S.G. Ma, Z.M. Jiao, J.W. Qiao, H.J. Yang, Y. Zhang, Z.H. Wang, Strain rate effects on

the dynamic mechanical properties of the AlCrCuFeNi2 high-entropy alloy, Mater. Sci. Eng. A. 649 (2016) 35–38. https://doi.org/10.1016/j.msea.2015.09.089.

[71] A. Arab, Y. Guo, Z. Dilshad Ibrahim Sktani, P. Chen, Effect of strain rate and temperature on deformation and recrystallization behaviour of BCC structure AlCoCrFeNi high entropy alloy, Intermetallics. 147 (2022) 107601. https://doi.org/10.1016/j.intermet.2022.107601.

[72] C.M. Cao, W. Tong, S.H. Bukhari, J. Xu, Y.X. Hao, P. Gu, H. Hao, L.M. Peng, Dynamic tensile deformation and microstructural evolution of AlxCrMnFeCoNi high-entropy alloys, Mater. Sci. Eng. A. 759 (2019) 648–654. https://doi.org/10.1016/j.msea.2019.05.095.

[73] X. Gao, Y. Lu, J. Liu, J. Wang, T. Wang, Y. Zhao, Extraordinary ductility and strain hardening of Cr26Mn20Fe20Co20Ni14 TWIP high-entropy alloy by cooperative planar slipping and twinning, Materialia. 8 (2019) 100485. https://doi.org/10.1016/j.mtla.2019.100485.

[74] H. Li, C. Shao, O.K. Orhan, D.F. Rojas, M. Ponga, J.D. Hogan, Strain-Rate-Dependent mechanical behavior of a non-Equimolar CoCrFeMnNi high entropy alloy with a segmented coarse grain structure, Materialia. 21 (2022) 101271. https://doi.org/10.1016/j.mtla.2021.101271.

[75] X. Zhong, Q. Zhang, M. Ma, J. Xie, M. Wu, S. Ren, Y. Yan, Dynamic compressive properties and microstructural evolution of Al1.19Co2CrFeNi1.81 eutectic high entropy alloy at room and cryogenic temperatures, Mater. Des. 219 (2022) 110724. https://doi.org/10.1016/j.matdes.2022.110724.

Chapter 2 MATERIALS AND METHODOLOGY

2.1 Introduction

This chapter deals with the aspects of design considerations taken before fabrications, the different processing routes undertaken for the study, the characterizations techniques and mechanical testing methods adopted to meet the thesis objectives. Firstly, the criteria to fabricate a dual-phase high entropy alloy is established. This is followed by the different processing routes undertaken during the thesis work.

2.2 Material

A novel dual FCC-BCC phase high entropy alloy of AlCoCrFeNi system with a nominal composition of $Al_{0.65}CoCrFe_2Ni$ was designed. The nominal composition has been listed in Table 2.1.

Table 2.1 Nominal composition of the principal elements of the high entropy alloy

Elements	At. wt. %
Al	0.1150
Co	0.1769
Cr	0.1769
Fe	0.3538
Ni	0.1769

For the calculation of the enthalpy of mixing, the following equation Eq 2.1 was used.

$$\Delta H_{mix} = \sum_{i=1, i \neq j}^{n} 4\, \Delta H_{AB}^{mix}\, x_i x_j \qquad 2.1$$

The binary enthalpy of mixing of two elements each for the alloy system of Table 2.2 was taken for determining the weighted average enthalpy of mixing.

Table 2.2 Enthalpy of mixing values for binary alloy system consisting of the principal elements of the alloy under study.

Binary Equi-atomic Alloy	Enthalpy of mixing (eV/atom)
AlCr	- 20.32
AlCo	-29.06
AlFe	-21.56
AlNi	-32.546
CoCr	-4.44
CoFe	-0.561
CoNi	-0.218
CrFe	-1.448
CrNi	-6.645
FeNi	-1.542

The theoretical values of enthalpy of mixing (ΔH_{mix}), configurational entropy (ΔS) and size effect (δ) were calculated as $-12.2636\ KJ/mol$, 1.535 R (gas constant) and 4.67%, respectively [1]. The overall combined effect (Ω) of entropy, enthalpy and size effect is calculated to be greater than 1.1 thereby conforming to all the required criteria of high entropy alloys [2–4]. The valence electron concentration (VEC) criteria of 6.4<VEC<8.5 was also maintained at 7.626 to obtain both FCC and BCC phases in the alloy [5]. All the parameters are listed in Table 2.3.

Table 2.3 Parameters of dual-phase high entropy alloy $Al_{0.65}CoCrFe_2Ni$

Parameters	Values
Configurational entropy, $\Delta S_{configurational}$	1.535 R
Enthalpy of mixing, ΔH_{mix}	$-12.2636\ KJ/mol$
Atomic size effect, δ	4.67%
Combine effect, Ω	16.9
Valence electron Concentration, VEC	7.626

2.3 Processing Techniques

2.3.1 Industrially Melted/As-Cast/Large-Scale (IM)

The large-scale alloy was prepared by vacuum induction melting setup at Mishra Dhatu Nigam Limited, (MIDHANI) Hyderabad. The vacuum induction furnace has a crucible with alumina lining and a capacity of 60 Kg. The melting was performed in an argon atmosphere of around 10^{-2} mbar for 30 minutes. Electromagnetic stirring was used to ensure the homogeneity of the melt pool. After the complete meltdown and stirring, the liquid melt was poured in a rectangular shaped mould located within the argon chamber. An appropriate riser was designed on the top of the mould to the casting to ensure casting defect-free condition. The cast was kept within the furnace chamber in the argon atmosphere for a few hours to complete solidification. The cooling rate of solidification during this processing was ~10 K/s. This initial alloy prepared at a large industrial scale under a low cooling rate is named as the IM (industrially melted) alloy in this thesis for convenience.

2.3.2 Suction Cast/Small-Scale/Lab-Scale (SC)

Figure 2.1 (a) Vacuum arc melting set up (b) Copper mould (c) Suction-cast (SC) sample

Another sample of the alloy was further fabricated from the pre-melted IM alloys at a small lab scale using Cu-suction casting. Firstly, they are re-melted for three to four times in vacuum arc melting furnace where an electric arc is struck between tungsten electrode and the as-cast IM alloy of 50g samples placed in semi hemispherical depression in the copper hearth These re-melted alloy samples were then suction cast into a copper-cooled mould to obtain cylindrical samples of diameter 6mm and length of 80mm. This processing technique involved a high cooling rate of the order of 10^3 K/s. This condition constitutes the second alloy conditions which is designated as the SC (suction cast) alloy.

2.3.3 Friction Stir Processed (FSP)

Friction Stir Processing (FSP) of the IM alloy were carried out using a semiautomatic FSW machine with 25 kW spindle drive motor power. A hydraulic power pack system was fitted that provided maximum compression force of $55-58$ KN (working range) during welding condition. The machine frame was robust; thus, it did not deflect significantly during the FSP experiments. The available traverse speeds and rotational speeds are in the range of 20 $\mathrm{mm/s}$ to 300 $\mathrm{mm/s}$ and 300 to 1800 $\mathrm{rev/min}$ respectively. The fixture has mainly four main components i.e. backing plate, clamping plate, stopper and alignment bolts. These necessary features were aimed to clamp the work plate rigidly and arrest the motions in X, Y and Z directions during welding. The low carbon steel plates were secured with work holding fixtures on the machine traverse table. The Y axis motion was constrained with horizontal clamps and the X axis motion was clamped by the stopper fixed at the end position.

2.4 Characterisation

2.4.1 X-Ray Diffraction

Initial characterization for qualitative confirmation for crystal structures present in the alloy system were carried out by XRD (Make: Rigaku Technologies, Japan Model: Smartlab) operated at 45kV and 200 mA using Cu-Kα radiation ($\lambda = 1.5402$ Å). The analysis helped in the ascertaining the interplanar spacing and also helped us in understanding the dislocation density of the alloy under different conditions. Samples were cut using WEDM and the thickness of the samples were kept under 3mm. Then the samples were polished by standard metallographic techniques before placing under XRD. The scanning was carried out for a range from 20° to 100° at a scan rate of 0.5°/s. The diffraction peaks in terms of Miller indices were found out to ascertain the phases present. The concept of peak broadening of XRD peaks were also employed the dislocation density of the alloy samples.

2.4.2 Metallography Sample Preparation

The samples for microstructural examinations were prepared by standard metallographic sample preparation technique. Initial samples were cut using Wire Electrical discharge machining (WEDM). The sliced samples of the samples were mounted in thermosetting resin using hot mounting press (Make: Buehler, Model: Simplimet-2). The samples were then polished with various grades (80-2000 grit size) of SiC coated emery papers. Finally, the samples are cloth polished and ultrasonically cleaned in acetone for 5 minutes.

2.4.3 Scanning Electron Microscopy

The polished samples were observed under Field Emission Scanning Electron microscope (FESEM) (Make: Zeiss, Model: Sigma 300). The instrument is a high-performance instrument designed for gaining maximum information from the broadest range of sample and high flexibility in imaging and analysis, which can also be future upgradability for any kind of in situ application. The majority of the FESEM imaging was carried out with accelerating voltages of the range of 10-20 kV. The composition analysis was carried out using energy dispersive X-ray spectroscope EDX fitted with the FESEM. The X-ray elemental mapping technique obtained quantitative distribution of various elements of the high entropy alloy over the specified area.

2.4.4 Electron Backscatter Diffraction

The polished samples discussed under metallographic sample preparation are electropolished before considering for Electron backscatter diffraction analysis. FEI Quanta 200 HV SEM with TSL-EDX OIM system facility at Indian Institute of Technology Bombay was availed for orientation image mapping. Different misorientation calculations like inverse pole figure (IPF), phase map, kernel average misorientation (KAM), grain orientation spread (GOS) maps and geometrically necessary dislocation (GND) maps were utilized to characterize the samples before and after deformation.

2.4.5 Transmission Electron Microscopy

The crystal structure of the samples was further investigated using a TEM (Make: JEOL, Model:2100F) equipped with an energy-dispersive X-ray spectrometer (EDS) facility and operated at an accelerating voltage of 200 kV. TEM specimens were prepared by slicing fine pieces of the sample using a diamond cutter and then polishing them down to 80-100 µm thickness using SiC papers. Discs having a 3 mm diameter were punched out from these thin slices. The final thinning of the TEM specimen was done using twin-jet electropolishing, with 10% perchloric acid and 90% ethanol solution as the electrolyte at about -35°C and an applied voltage of 20V. Selective area electron diffraction (SAED) patterns were obtained, which were then indexed to identify the structure of the alloy before and after deformation.

2.5 Mechanical Testing

2.5.1 Hardness

Another vital property of the alloy is the determination of the hardness of the specimen which is correlated to the crystal structure and the composition of the material being tested. There are numerous methods to determine the hardness. The hardness here is determined by the micro Vickers hardness tester by Omni Tech. Vickers hardness can be determined as follows:

$$HV = \frac{2F \sin\frac{136°}{2}}{d^2} \qquad 2.2$$

2.5.2 Quasi Static Compression Testing

The compression tests were carried out in cylindrical samples of diameter 6mm with height 6mm in a digitally controlled closed loop servo hydraulic 100 kN dynamic testing machine (Make: Instron, Model: 8801) at strain rates of 10^{-2}-10^{-4} s^{-1}. Load-displacement data generated during the test were recorded using a data acquisition system integrated with the machine. These were eventually used to determine 0.2% offset yield strength (YS) and the strain hardening exponent (*n*).

2.5.3 High Strain Rate Testing

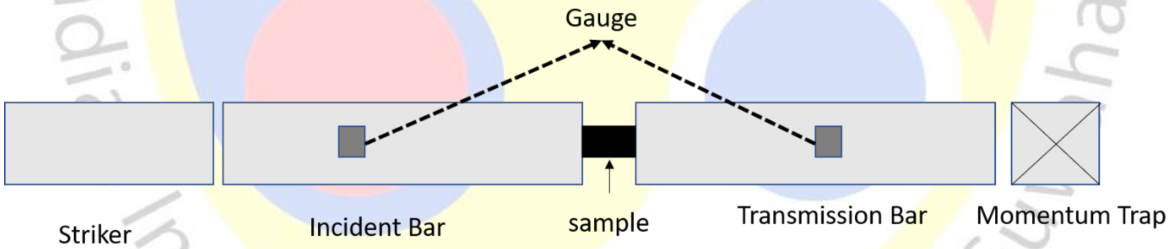

Figure 2.2 Schematic of SHPB apparatus experimental setup

Split Hopkinson pressure bar (SHPB) is a standard technique to characterize a material at high strain rates. The setup consists of a striker bar, an incident bar and a transmitter bar aligned to each other as shown in the schematic (Fig 2.2). The alloy sample are sandwiched between the incident and the transmitter bar. An important factor that limits the maximum attainable specimen stress is the yield stress of the bars used. Therefore, careful examination of failure stress levels of specimen is needed before selecting material for pressure bars. In the present work the bars used were made of Maraging steel having yield strength of 2.1 GPa.

The diameters of the striker bar, incident bar and transmitted bar used were equal to 12.5 mm. The length of the incident bar and the transmitted bar were 1525 mm and 1350 mm. The length of the striker bar was used were 300 mm and 400 mm according to vary the input strain/volt. The equations developed in following sections are valid for elastic behaviour of the bar only.

The impact of the 300 mm and 400 mm striker bar onto the incident bar generates a finite length compressive stress pulse. The stress pulse travels through the incident bar towards the first face of the specimen where part of it gets reflected back into the incident bar due to the impedance mismatch and remaining is transmitted through the specimen into the transmitter bar. The incident and transmitted pulses are compressive in nature and the reflected is tensile.

The incident, reflected and transmitted strain pulses were measured by two sets of electrical resistance strain gauges. (Tokyo Sokki Kenkyujo Co.Ltd, Japan). The strain gauges were FLA-3-11 type with a gauge length of 5 mm and a gauge factor of ~2.1 (gauge resistance of ~120Ω). The gauges were mounted diametrically opposite on each of the bars with the help of an epoxy-based adhesive. The excitation and calibration voltages used are 3 V and 1.5 V. The input and output signals from the strain gauges were fed through a half-bridge circuit into an Ectron 563 strain conditioner having 200 kHz bandwidth. The amplified single ended signals were then fed into a 10-bit, 4 channel digital oscilloscope (model DSO LT-224 manufactured by LeCroy Corporation, USA) where signals are digitized and stored at sampling rate of 1Ms/s. the experimental set up. Calibration and alignment of the set up through a bar to bar test stress record for 400 mm striker at 4kg/cm^2 pressure using a 0.6mm pulse shaper. The pressure of the bar is controlled via a solenoid valve. Few of the assumptions while carrying out the experiment data analysis are [6]:

- The bar material remains elastic throughout the experiments and follows the Hooke's law.
- Plane and parallel cross sections remain plane and parallel after deformation.
- Lateral inertia effects are negligible.
- The surface strains measured by the strain gauges represent the axial strain over the entire cross-sectional area.
- The wave propagation is assumed to be one dimensional without any dispersion.

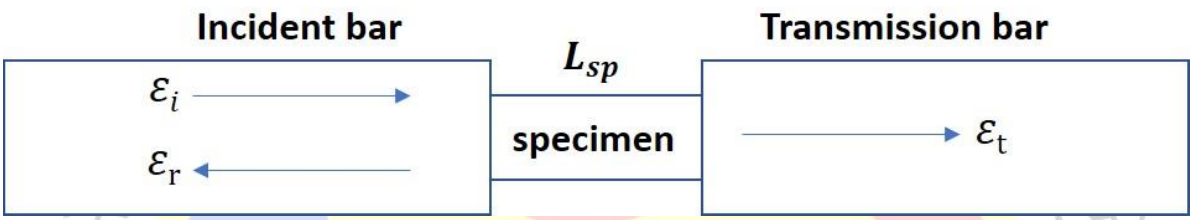

Figure 2.3 Wave interaction is SHPB apparatus for strain measurements

The basic calculations involved in SHPB tests based on one dimensional stress wave theory relates velocities of the particle at both ends of the specimen to the three measured strain pulses incidence bar (ε_i), reflected (ε_r)and transmitted bar (ε_t) in a sample of length L_{sp} as shown in Fig 2.3 to find the stress σ_s, ε_s strain and $\dot{\varepsilon}_{sp}$ strain rate of the sample is given by the following equations [6,7].

$$\sigma_s(t) = \frac{A_b}{A_{sp}} E_b \varepsilon_t(t) \quad 2.3$$

$$\varepsilon_s(t) = \frac{2C_0}{L}\int_0^t (\varepsilon_t(t))d\tau \quad 2.4$$

$$\dot{\varepsilon}_{sp} = -2\frac{C_b}{L_{sp}}\varepsilon_t(t) \quad 2.5$$

where C_0, E_b and V_{st} are density of the bar material, Elastic wave speed of the bar and striker projectile velocity respectively. The parameters of the SHPB set is listed below:

Table 2.4 Parameters of SHPB setup

Parameters	Details
Material of the bar	Maraging steel
Bar Diameter	12.5 mm
Length of incident bar	1525 mm
Length of transmitted bar	1350 mm
Length of striker	300 mm, 400 mm
Resistance of strain gauges	120 ohms
Gauge Factor	2.13 $\pm$ 1 %
Elastic of modulus, *E*	210 GPa
Elastic wave velocity of the bar, C_0	4800 m/s

References

[1] Y. Lu, Y. Dong, S. Guo, L. Jiang, H. Kang, T. Wang, B. Wen, Z. Wang, J. Jie, Z. Cao, H. Ruan, T. Li, A promising new class of high-temperature alloys: Eutectic high-entropy alloys, Sci. Rep. 4 (2014) 1–5. https://doi.org/10.1038/srep06200.

[2] Y. Zhang, X. Yang, P.K. Liaw, Alloy design and properties optimization of high-entropy alloys, JOM. 64 (2012) 830–838. https://doi.org/10.1007/s11837-012-0366-5.

[3] X. Yang, S.Y. Chen, J.D. Cotton, Y. Zhang, Phase Stability of Low-Density, Multiprincipal Component Alloys Containing Aluminum, Magnesium, and Lithium, JOM. 66 (2014) 2009–2020. https://doi.org/10.1007/s11837-014-1059-z.

[4] X. Yang, Y. Zhang, Prediction of high-entropy stabilized solid-solution in multi-component alloys, Mater. Chem. Phys. 132 (2012) 233–238. https://doi.org/10.1016/j.matchemphys.2011.11.021.

[5] M.H. Tsai, K.Y. Tsai, C.W. Tsai, C. Lee, C.C. Juan, J.W. Yeh, Criterion for sigma phase formation in Cr- and V-Containing high-entropy alloys, Mater. Res. Lett. 1 (2013) 207–212. https://doi.org/10.1080/21663831.2013.831382.

[6] M.A. Meyers, Shear Bands: Metallurgical Aspects, 1994. https://books.google.com.au/books?id=WoEDHtRTOhoC.

[7] G.C. Soares, M. Patnamsetty, P. Peura, M. Hokka, Effects of Adiabatic Heating and Strain Rate on the Dynamic Response of a CoCrFeMnNi High-Entropy Alloy, J. Dyn. Behav. Mater. 5 (2019) 320–330. https://doi.org/10.1007/s40870-019-00215-w.

Chapter 3 Strengthening Mechanisms and Deformation Behaviour of Industrially Melted Large-Scale As-Cast and Rapidly Cooled Lab Scale Suction-Cast Dual-Phase High Entropy Alloy

3.1 Introduction

In this chapter, the iron-rich high entropy alloy $Al_{0.65}CoCrFe_2Ni$ comprising of both FCC and BCC phases was designed and fabricated using induction melting at a large scale and suction casting at a small lab scale. Spinodally decomposed interdendritic regions were uniformly distributed in the industrially melted alloy, and a finer dendritic structure with smaller sized spinodal structures was observed in the alloy suction cast at lab scale. The suction cast alloy fabricated at the lab scale exhibited significantly higher compressive yield strength compared to the industrially cast alloy. The relative strengthening contributions in the alloys due to solid solution, grain boundary, dislocation interactions and interphase boundary were analysed. Dislocation hardening was the major contributor responsible for the higher strength of the SC alloy. The deformation behaviour in the alloys was examined with the help of orientation image mapping. Intense slip band formation at large strains in the industrially melted alloy indicates that cold working can be an effective technique to enhance the strength of the dual-phase high entropy alloy processed at a large scale.

3.2 Material and Methodology

The novel dual FCC-BCC phase high entropy alloy with a nominal composition of $Al_{0.65}CoCrFe_2Ni$ was designed. The theoretical values of enthalpy of mixing (ΔH_{mix}), configurational entropy (ΔS) and size effect (δ) were calculated as $-12.2636\ KJ/mol$, 1.535 R (gas constant) and 4.67%, respectively [28]. The overall combined effect (Ω) of entropy, enthalpy and size effect is calculated to be greater than 1.1 thereby conforming to all the required criteria of high entropy alloys [38–40]. The valence electron concentration (VEC) criteria of $6.4<VEC<8.5$ was also maintained at 7.626 to obtain both FCC and BCC phases in the alloy [41]. The industrial-scale alloy was prepared by vacuum induction melting setup at Mishra Dhatu Nigam Limited, (MIDHANI) Hyderabad. The vacuum induction furnace has a crucible with alumina lining and a capacity of 60 Kg. The melting was performed in an argon atmosphere of around 10^{-2} mbar for 30 minutes. Electromagnetic stirring was used to ensure the homogeneity of the melt pool. After the complete meltdown and stirring, the liquid melt was poured in a rectangular shaped mould located within the argon chamber. An appropriate riser was designed on the top of the mould to the casting to ensure casting defect-free condition. The cast was kept within the furnace chamber in the argon atmosphere for a few hours to complete solidification. The cooling rate of solidification during this processing was ~10 K/s. This initial alloy prepared at a large industrial scale under a low cooling rate is named as the IM (industrially melted) alloy in this article for convenience. For the microstructural analysis and the testing of mechanical properties, the samples were extracted from near the centre of the IM alloy to ensure uniform grain structure within the sample.

Another sample of the alloy was further fabricated from the pre-melted IM alloys at a small lab scale using Cu-suction casting. The pre-melted master alloy of around 50 g was suction cast into a copper-cooled mould to obtain cylindrical samples of diameter 6mm and length of 80mm. This processing technique involved a high cooling rate of the order of 10^3 K/s. This condition constitutes the second alloy which is designated as the SC (suction cast) alloy.

Microstructural analysis and phase identification for both the alloys IM and SC were carried out using X-ray diffraction (XRD), optical microscopy (OM) and scanning electron microscopy (SEM) techniques. The XRD analysis was performed with Cu-k_α radiation (λ=1.5406Å) operating at 50kV/160mA in Rigaku made instrument. After fine mechanical polishing, the IM alloy and the SC alloy samples were etched with 5g $K_2Cr_2O_7$ + conc. H_2SO_4 + H_2O and aqua regia respectively before observing under optical microscope and scanning electron microscope as per ASTM E3 standard. Field emission scanning electron microscope (FE-SEM) integrated with energy dispersive (EDS) detectors were used to examine the microstructure as well as elemental mapping at different locations. Oxford Instruments made electron backscatter diffraction (EBSD) probe integrated with FE-SEM was used to identify the phases and measure orientations of grains and other microstructures in both the samples. The orientation image map was generated using TSL-OIM software and ATEX software [42].

Owing to constraints in size of the alloy samples made at lab scale, quasi-static compression tests at a strain-rate of ~$10^{-4}s^{-1}$ were performed on cylindrical samples of diameter 6mm and length 6mm at room temperature using Instron 8801 universal testing machine to determine the mechanical properties of both the alloys. The hardness of the alloys was measured according to the ASTM E92 standard using the Omni Tech made micro-Vickers hardness tester under a load of 300g for 15 seconds.

3.3 Results and Discussion

In this section, the results obtained from different experimental studies to investigate the properties the properties of large scale industrially melted as-cast alloy and rapidly cooled lab-scale suction-cast alloy are presented.

3.3.1 Phase Estimation

The crystal structure of different phases of the dual-phase high entropy alloy was determined from the XRD patterns of the alloy. Fig. 3.1 represents the XRD patterns for the IM alloy and the SC alloy samples. The presence of both FCC and BCC phases can be ascertained from the 2θ peaks formed by the XRD pattern. The presence of FCC and BCC crystal structures in both the IM and the SC alloy samples conform to the prediction drawn from the VEC rule while designing the alloy.

The crystallographic planes of FCC phase in the IM alloy sample corresponding to five different XRD peaks with 2θ values of 43.95°, 50.99°, 74.87°, 90.58° and 95.82° are {111}, {200}, {220}, {311} and {222} respectively. The BCC crystal planes for the IM alloy sample corresponding to the diffraction peaks with 2θ angles 45.02°, 64.94° and 82.39° are {110}, {200} and {211} respectively. For the SC alloy, which was fabricated at a significantly higher cooling rate, the diffraction peaks with 2θ angles 44.24°, 51.24°, 74.94°, and 90.82° represent FCC crystal planes {111}, {200}, {220} and {311} respectively. The diffraction peaks of the SC alloy with 2θ angles 45.22°, 65.40°, 83.08° and 96.16° represent BCC crystal planes {110}, {200}, {211}and {220} respectively. Weak ordered B2 phase diffraction peaks were also observed corresponding to {100} plane near 35° 2θ values for both the alloys. Similar B2 ordered peaks were also reported for similar AlCoCrFeNi system in Wang *et al.* [22]. To further ascertain the presence of B2 phase in the alloys, compositional analysis has been carried out in the next section. The shift in the peaks of the SC alloy to higher angles than those of the IM alloy is due to residual thermal stress generated at a high cooling rate during the processing of the SC alloy. The lattice parameters calculated from the XRD pattern also imply the presence of higher thermal stress in SC alloy. The lattice parameters of FCC and BCC/B2 phases in the IM alloy were 3.84Å and ~2.86Å, respectively, and those in the SC alloy were 3.82 Å and ~2.83 Å, respectively. Thus, it can be ascertained that the SC phase has resulted in lattice shrinkage (decrease in d spacing) due to the presence of internal thermal stress.

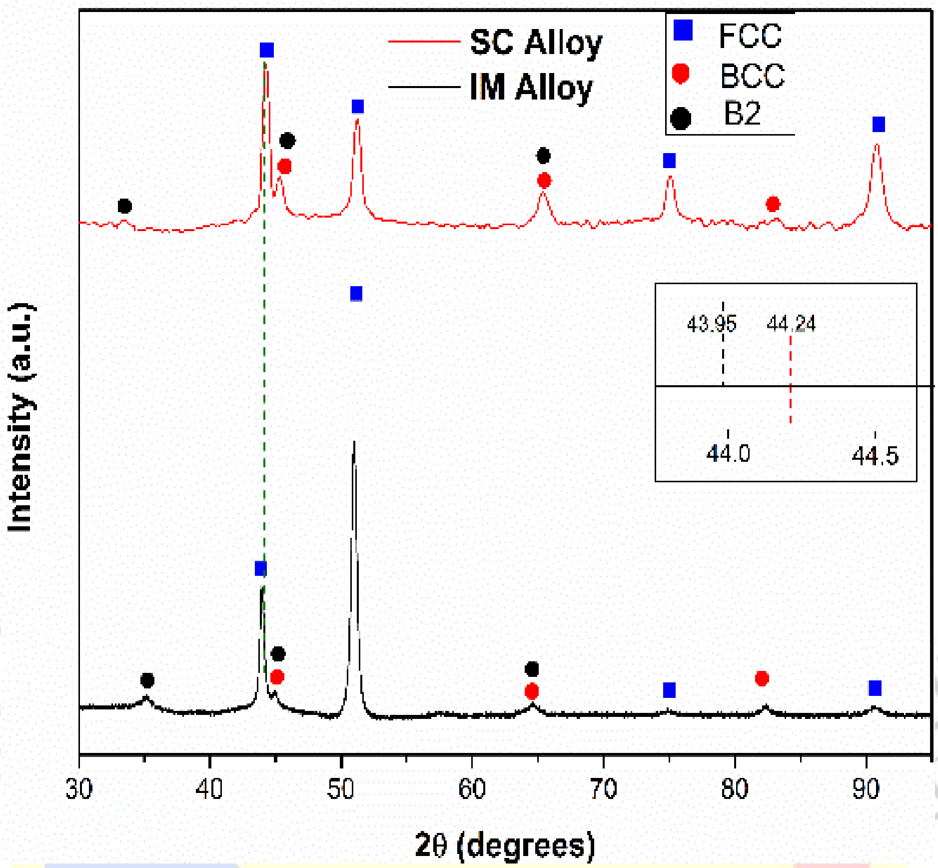

Figure 3.1 XRD pattern of IM and SC alloy samples and the inset rectangle showing the shift in the XRD pattern towards the right in the rapidly cooled SC alloy

3.3.2 Microstructural Analysis

The microstructure of the IM alloy was of near-eutectic dendritic nature, as suggested by the optical micrographs in Fig. 3.2(a). The average size of the dendrites was more than 100 µm, and the average length of the interdendritic regions was ~50 µm. The dendrites and the interdendrites formed a continuous network in the form of a cellular structure. The SEM image in Fig. 3.2(b) shows that the dendritic region of IM sample is a single bright phase, and the interdendritic region is comprised of periodic dark grey and lighter bright phases. Lv *et al.* and Wani *et al.* have also found similar structures in high entropy alloys [13,14,43]. They further claimed that these maze-like structures were formed due to spinodal decomposition (SD) of supersaturated solid solution [14,43]. Fig. 3.2(c) is a magnified image of the interdendritic region of the IM alloy sample, clearly showing a maze-like SD structure. As per the EDS elemental mapping in Fig. 3.2(d) and elemental composition in Table 3.1, the interdendritic region is rich in Al and Ni, and the dendritic region contains a high percentage of in Fe and Cr. A uniform distribution of Co was observed in both regions. Since Al stabilizes the BCC phase, it indicates the formation of the BCC phase in the interdendritic region [14]. Similar modulated SD structures comprised of ordered and disordered BCC phases have been found in $Al_{0.5}CoCrFeNi$, $AlCoCrFeNi_{2.1}$ and $Al_{0.7}CoCrFe_2Ni$ [14,44,45]. The compositional variation within the SD structure showed large fluctuation of Al, Ni, Cr and Fe atomic percentages. The bright phase within the SD structure comprised of high Ni (36.5 wt. %) and Al (14.3 wt. %) with depleted distributions of Fe (19.1 wt. %) and Cr (5.4 wt. %) can be identified as B2 phase. The dark phase in SD structure was rich in Cr (22 wt. %) with low distributions of Al (6 wt. %) and Ni (13.8 wt. %) and can be identified as A2 phase [36,46,47]. The average size of the spinodally decomposed B2 structure is close to 2 μm. The presence of multiple distinct phases in the IM alloy sample seen in the micrographs conform to the XRD results.

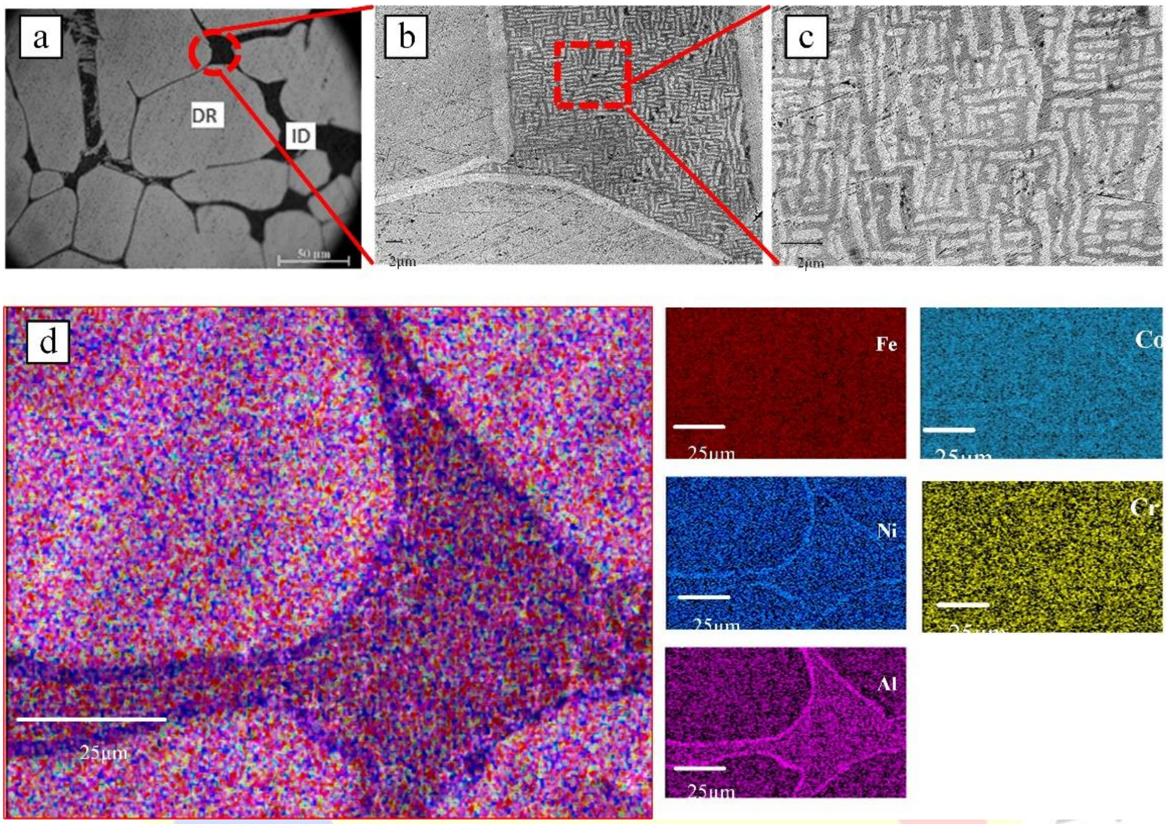

Figure 3.2 Micrographs of the IM alloy: (a) Optical micrograph, (b) SEM image showing both dendritic and interdendritic regions, (c) magnified SEM image of the interdendritic zone showing maze-like SD structure, and (d) EDS elemental mapping showing Ni and Al rich interdendritic region.

Figs. 3.3(a) and 3.3(b) show that the microstructure of the SC alloy is a mixture of eutectic lamellar dendrites and anomalous [48]. The lamellar dendritic arm spacing is finer compared to the IM alloy. The average thickness of the dendritic arm was 5 µm. The dendritic arm span of the SC alloy was much shorter than that of the IM alloy due to the very high cooling rate of processing of the SC alloy. The high cooling rate of solidification had led to potentially higher nucleation sites that reduced the size of dendrites [43]. The elemental mapping in Fig. 3.3(d) and the EDS composition in Table 3.1 clearly show that the SC alloy displayed similar Al-rich interdendritic BCC regions and the dendritic FCC region rich in Fe like that of the IM alloy.

The microstructure of the IM and the SC alloys were distinctly different. The size of the SD-region present in the SC alloy was of the order of 10 nm (Fig. 3.3(c)), which was significantly smaller compared to those of the IM alloy (Fig. 2(b)). The variation in Al in the B2 phase (16.6 at. %) and A2 phase (7.3%) is 9.3 %. Due to the sluggish diffusion of HEAs and higher cooling rate in the SC alloy, non-equilibrium solidification occurred, hindering the formation of SD regions [14].

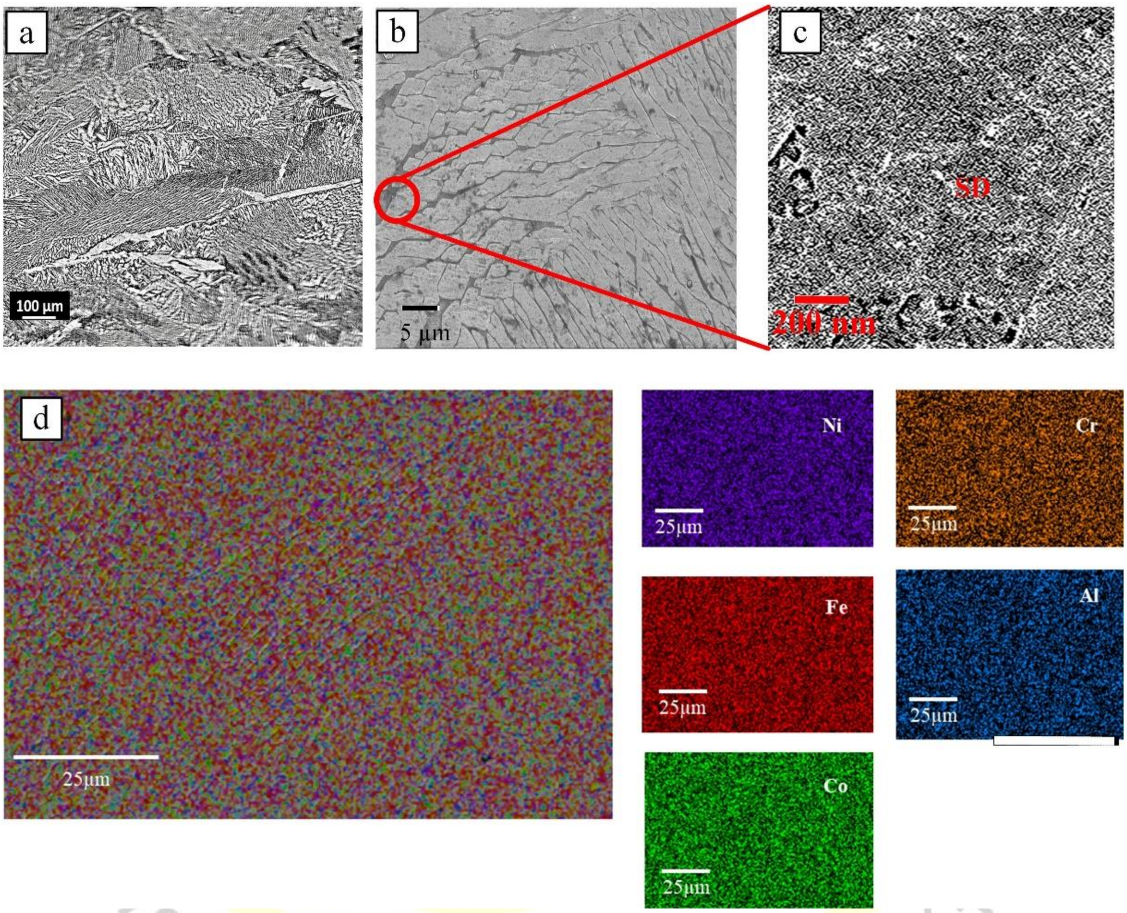

Figure 3.3 Micrographs of the SC alloy: (a) Optical micrograph, (b) SEM image, (c) SEM image of fine SD structure, and (d) EDS elemental mapping of the SC alloy

Table 3.1 Elemental composition of different phases in the IM alloy and the SC alloy

Alloy	Zones	Al (wt.%)	Co (wt.%)	Cr (wt.%)	Fe (wt.%)	Ni (wt.%)
IM alloy	Dendritic (FCC)	4	20.7	20.1	35.3	19.9
	Interdendritic (BCC)	13.9	23.7	9.4	21.3	31.7
SC alloy	Dendritic (FCC)	3	21.5	19.5	35.5	19.7
	Interdendritic (BCC)	8.8	18.1	22.8	31	19.4

3.3.3 Mechanical Properties

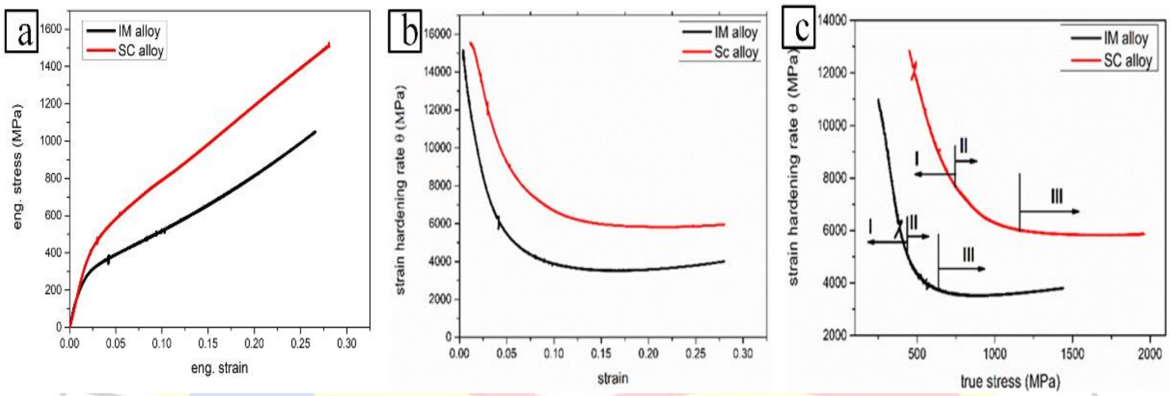

Figure 3.4 (a) Engineering stress-strain curve of the IM and the SC alloys at quasi-static loading of strain rate ~$10^{-4}s^{-1}$, (b) the strain hardening rate of both the alloys as a function of plastic strain, and (c) Kocks-Mecking (K-M) plots of both the alloys showing strain hardening rate as a function of flow stress.

The uniaxial compressive tests of the IM and the SC alloys were performed under quasi-static conditions with strain rates of the order of 10^{-4} s^{-1}. The engineering stress-strain curve for both the alloys are shown in Fig. 3.4(a). The compressive yield strength of the IM alloy sample was ~250 MPa. For the same strain rate of loading, the SC alloy sample showed an average yield strength of ~420 MPa. The increase in yield strength of the SC alloy compared to IM alloy was 68%. The as-cast IM alloy showed higher compressive yield strength than most of the single-phase FCC high entropy alloys of the AlCoCrFeNi system [14,20,49,50] . However, the yield strength of the IM alloy was lower than BCC based HEAs [12,14,31,51] The yield strengths of the IM and the SC alloy were also compared with the other dual-phase high entropy alloys having FCC and BCC phases. The yield strength of the IM alloy is comparable with arc-melted dual-phase $Al_{0.5}CoCrFeNi$ alloy [14] but lower than some other dual-phase HEAs, e.g., $Al_{0.7}CoCrFeNi$ and $Al_{0.7}CoCrFe_2Ni$ [22,29,30]. The SC alloy exhibited higher strength than suction-cast $Al_{0.5}CoCrFeNi$ alloy [14].

The IM and SC alloys showed excellent strain hardening and strain hardening rate until a strain of 28%. The strain hardening rate $\frac{d\sigma}{d\varepsilon}$, denoted by θ, was studied by plotting it as a function of true strain (ε) and flow stress (σ) (Figs. 3.4(b) and 3.4(c)). The Kocks-Mecking (K-M) curve is an excellent approach to describe the changes in the dislocation structures during different stages of strain hardening rate [52,53]. The strain hardening rate (θ) vs flow stress (σ) in Fig. 3.4(c) shows that both the alloys exhibited three stages of strain hardening. The initial elastoplastic region, in which the strain-hardening rate rapidly decreases with flow stress, is described as transient stage (stage I), and the stage with gradually decreasing strain hardening rate is known as stage II, which can be best governed by Kocks-Mecking dislocation theory. According to K-M theory, in stage II strain hardening rate, there is constant storage and annihilation of dislocation at a local level, and the slope of θ-σ curve $\left(\frac{d\theta}{d\sigma}\right)$ in this stage gives the rate of decrease of strain hardening rate with stress [52–54]. Eventually, at large stresses, the strain hardening rate (θ) become almost asymptotic and is identified as stage III. In stage II of the K-M plot, the slope of strain hardening rate (θ) for the SC alloy was lower compared to the IM alloy (Fig. 3.4(c)). The finer microstructure in the SC alloy resulted in a higher accumulation of dislocations compared to the IM alloy. Previous literature has reported that the Hall-Petch effect and Taylor dislocation strengthening contributions are significant in both the elastic-plastic stage (transient/stage I) and the plastic stage (stage II) [54–56]. However, the strain hardening rate in the IM alloy displayed an increasing slope at strains greater than 15% in Fig. 3.4(b) and at stresses greater than 750 MPa in Fig. 3.4(c) while that of the SC alloy followed an asymptotic path. This implies the initiation of another deformation mechanism in the IM alloy at large strains, which will be further discussed in the following sections.

Table 3.2 Micro-Vickers Hardness

Material	Average Hardness
IM alloy (Interdendritic)	128 HV
IM alloy (Dendritic)	94 HV
SC alloy	160.5 HV

The average hardness values of the dendritic zone and the interdendritic zone in the IM alloy sample were 94HV and 128 HV, respectively. This indicates the presence of a softer FCC phase in the dendritic zone and harder spinodally decomposed BCC phases in the interdendritic zone. The average hardness of the suction cast (SC) sample was 160.5 HV [14].

3.3.4 Strengthening Mechanisms

The primary strengthening mechanisms involved in dual-phase HEAs can be categorized into four broad mechanisms: solid solution strengthening, grain boundary strengthening, dislocation hardening, and precipitation strengthening. The strength of a polycrystalline high entropy alloy can be cumulatively written as the summation of the above-mentioned strengthening mechanisms.

$$\sigma_{0.2} = \sigma_0 + \Delta\sigma_{ss} + \Delta\sigma_D + \Delta\sigma_{GB} + \Delta\sigma_{ppt} \qquad 3.1$$

,where σ_0 is the lattice friction stress, $\Delta\sigma_{ss}$ is the solid solution strengthening, $\Delta\sigma_D$ is the dislocation hardening, $\Delta\sigma_{GB}$ is the grain boundary contribution to strength, and $\Delta\sigma_{ppt}$ is the strengthening due to the presence of precipitation [36,57,58]. The lattice friction stress σ_0, which is an intrinsic property of a material, is calculated to be ~114 MPa applying the rule of mixture taking the elemental lattice friction stress values as given in the table below [59]:

Table 3.3 Individual Frictional Stress and Elastic Modulus of the elements

Element	σ_0 (frictional stress) (MPa)	Elastic modulus (GPa)
Al	16	70
Co	10.3	211
Cr	454	131
Fe	100	204
Ni	22	191

Similarly, the elastic modulus of the alloys is found to be ~175 GPa.

(a) Solid solution strengthening

High entropy alloys inherently possess high solid solution strengthening due to the difference in atomic size among its principal elements. However, it is a difficult process to distinguish the solute and the solvent in HEAs. The extent of the solubility of large atoms in the alloy determines the strength of solid solution strengthening [60]. Since the dendritic FCC region is the primary phase in both the alloys, the solid solution strengthening based on the solubility of atoms in the FCC phase have been determined to estimate solid solution strengthening.

The mismatch in atomic sizes gives an excellent estimate of solid solution strengthening in an alloy as the amount of total atomic size mismatch is directly proportional to the solubility of the atoms. The atomic size mismatch can be calculated as [57]:

$$\delta = \sqrt{\sum_{i=1}^{N} C_i \left(1 - \frac{r_i}{\sum_{i=1}^{N} C_i r_i}\right)^2} \qquad 3.2$$

,where N is the number of components, C_i is the atomic percentage of the *ith* element in the primary phase/matrix, i.e. dendritic FCC in this case, r_i is the atomic radius of the *ith* element, and $\sum_{i=1}^{N} C_i r_i$ is the average atomic radius of the dendritic FCC region. The average nominal metallic radius of the FCC phase for the IM alloy and the SC alloy was calculated to be 1.22 Å and 1.26 Å, respectively. The atomic size mismatch δ in the primary FCC phase of the IM alloy and the SC alloy was calculated as 0.897 and 0.5847, respectively. The amount of atomic size mismatch is directly related to the solid solution strengthening, and hence, it indicates that the IM alloy possessed more solid solution strengthening than the SC alloy.

In $Al_xCoCrFeNi$ system, solid solution strengthening primarily depends on the lattice distortion based on compositional variation. Considering Al atoms as solute and the rest of the elements (Co, Cr, Fe, Ni) as the solvent, the Gypen L A formula can be used to determine the solid solution strengthening as given below [61]:

$$\Delta\sigma_{ss} = (\sum(k_i.\sqrt{c_i})^{\frac{1}{p}})^p \qquad 3.3$$

where k_i is the strengthening coefficient of solute i, c_i is the atomic percentage of solute i, and the value of p is ½. The average atomic percentage of Al in the FCC dendritic region for the IM alloy and the SC alloy was 8.4 at.% and 7.4 at.%, respectively. The value of k_{Al} = 225MPa/(at. %)$^{1/2}$ was adopted [61]. Thus, the total solid solution strengthening in the case of the IM alloy and the SC alloy was calculated as ~65 MPa and ~61MPa, respectively. Both atomic mismatch criteria and Gypen L A estimation predicted that solid solution strengthening in the IM alloy was higher than the SC alloy.

(b) Grain boundary strengthening

The strength of a material is greatly influenced by average grain size. The smaller the grain size, the greater is the number of obstacles that the dislocations have to overcome. The classic Hall-Petch equation relates the grain size to the yield strength of the material [62].

$$\sigma_y = \sigma_0 + \frac{k_y}{d^{\frac{1}{2}}} \qquad 3.4$$

where σ_0 is the lattice friction stress, k_y is the strengthening coefficient, and d is the grain diameter. The increase in yield strength due to refinement in grain size can be further derived from the above equation for the IM alloy and the SC alloy as:

$$\Delta\sigma_{GB} = k_y(d_{IM}^{-\frac{1}{2}} - d_{SC}^{-\frac{1}{2}}) \quad 3.5$$

The average grain size of the SC alloy was found to be 153.6 µm, and that of the IM alloy was approximately 1500 µm. The value of k_y for the FeMnCoCrNi system can be adopted as 226 MPa.µm$^{1/2}$ [63]. Therefore, the difference in strength increment, due to grain boundary strengthening, between the SC alloy and the IM alloy was evaluated as ~13 MPa.

(c) Dislocation hardening

The movements of dislocations and the interactions among them impede their mobility, which contributes to the hardening of the material. The Bailey-Hirsch formula lays down a relationship between dislocation density and dislocation hardening, as given below [63].

$$\Delta\sigma_D = M\alpha Gb\rho^{0.5} \quad 3.6$$

where M is the Taylor factor and is equal to 3.06 for FCC phase, α=1 is a correcting constant [64], the Burgers vector is given by $b = \frac{1}{\sqrt{2}}a_{FCC}$, G is the shear modulus which is taken as 84 GPa [65] and ρ is the dislocation density (in m^{-2}).

The Williamson-Hall method gives a reasonable estimate of the dislocation density, which considers the effects of both microstrain and grain size. The FWHM (full width half maximum) or the true XRD peak broadening β of the FCC-phase peaks has contributions from both microstrain (β_S) and grain size (β_G). The Williamson-Hall equation is given by [61,63]:

$$\beta = \beta_G + \beta_s \tag{3.7}$$

$$\beta_G = K\lambda/(D\ cos\theta) \tag{3.8}$$

$$\beta_s = 4\varepsilon\ sin\theta \tag{3.9}$$

where K=0.9 is a constant, λ=0.15406 nm is the wavelength of Cu k_α-radiation, D is the grain size, and ε is the microstrain. By rearranging the Williamson equation, the microstrain ε can be given by the slope of the following equation:

$$\beta cos\theta = \frac{K\lambda}{D} + 4sin\theta.\varepsilon \tag{3.10}$$

The FWHM (β) was calculated using Gaussian fit and eliminating the instrument error. Thus, the microstrain ε was evaluated from Eq. (10) by plotting $\beta cos\theta$ vs $4sin\theta$ as shown in Fig. 4.5, and the microstrain values for the IM alloy and the SC alloy were ~0.0001 and 0.269, respectively. The microstrain is directly related to the dislocation density as given below [63]:

$$\rho = (2\sqrt{3}\ \varepsilon)/(D\ b) \tag{3.11}$$

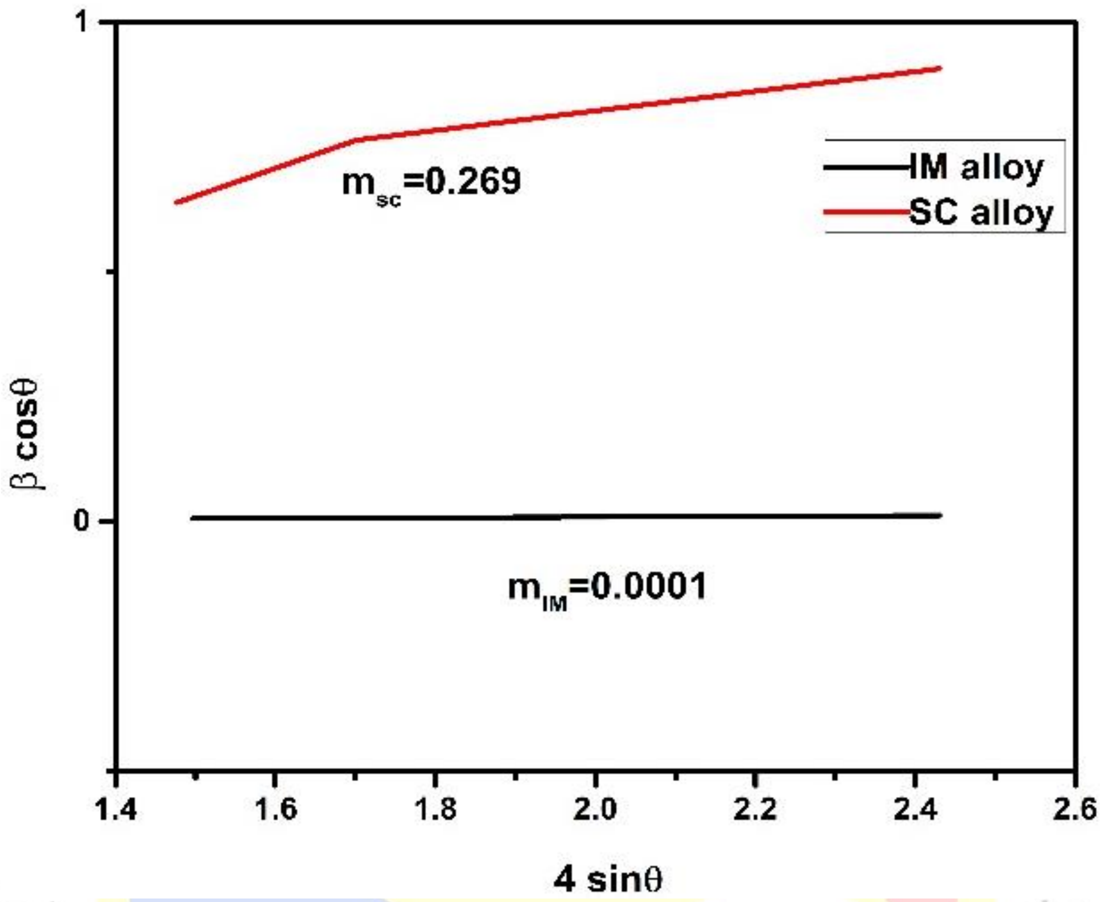

Figure 3.5 Linear relationship between $\beta cos\theta$ and 4 $sin\theta$

The dislocation density calculated for the IM alloy was too low, and hence, neglected. The dislocation density for the SC alloy calculated from the above equation was 2.24×10^{13} m^{-2}. Thus, the dislocation strengthening $\Delta\sigma_D$ using Eq. 6 for the SC alloy was ~262 MPa and that for the IM alloy was negligible. Thus, it suggests that the higher cooling rate of solidification in the SC alloy was the major cause of significant microstrain resulting in high dislocation hardening.

(d) Spinodal decomposition strengthening

The presence of interdendritic interphase boundaries within the grains also contribute to the strengthening of the material primarily due to modulus mismatch, change in lattice parameter and difference in stacking fault. The EBSD phase maps in Fig. 6 confirm that the dendritic regions and the interdendritic regions comprise of FCC and BCC phases, respectively, for both the IM alloy and the SC alloy. The phase percentage of the interdendritic BCC phase in the IM alloy (~15%) was higher than the SC alloy (~12 %).

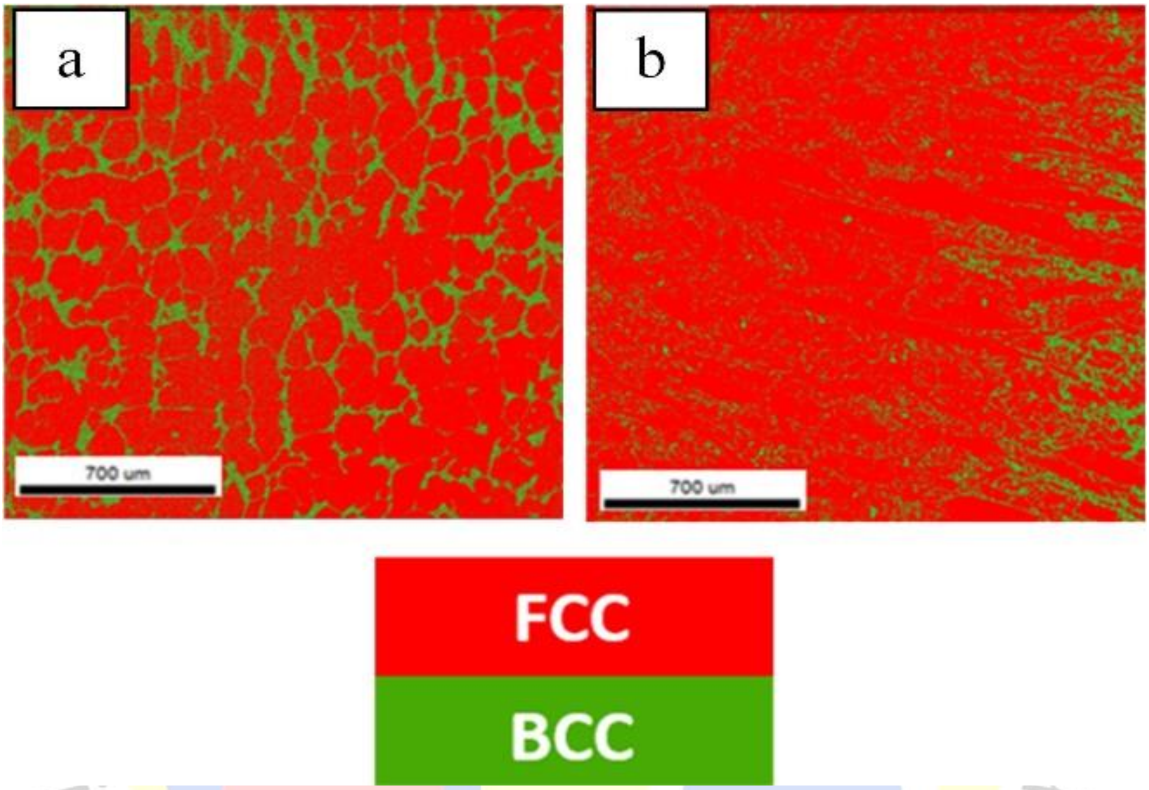

Figure 3.6 EBSD Phase maps of (a) IM alloy and (b) SC alloy with red colour representing FCC phase and green colour representing BCC phase

In addition, the presence of spinodally decomposed structures in the interdendritic BCC phase of the IM alloy and the SC alloy as seen in the SEM images of Fig. 3.2(c) and 3.3(c), respectively, contributed to spinodal strengthening. These strength contributions are similar to precipitation hardening [63], which enhance the strength of the material, *e.g.*, in high entropy alloy $Al_{0.5}Cr_{0.9}FeNi_{2.5}V_{0.2}$ [36]. Therefore, determining the spinodal strengthening is essential for the prediction of the overall strength of both the alloys. The strengthening contributions due to spinodal effects are due to lattice misfit and modulus differential, which is given by [36,57,58,61,63]:

$$\Delta\sigma_{SD} = f_{SD} * (\Delta\sigma_{\varepsilon} + \Delta\sigma_{G}) = f_{SD} * M * (\frac{0.5A\eta E}{1-\vartheta} + \frac{0.65\Delta Gb}{\lambda}) \quad 3.12$$

where f_{SD} is the percentage fraction of spinodal decomposition structures present in the alloys, A is the amplitude of atomic modulation (of Al atoms in these two alloys), ŋ is the variation in the lattice parameters of BCC/B2 interdendritic SD region, M = 2.73 is the Taylor factor for BCC phase, $\vartheta = 0.3$ is the Poisson's ratio for BCC phase, $\Delta G = 3\ GPa$ is the difference in shear modulus [61], λ is the average feature size of the SD structure, and E =175 GPa is the elastic modulus calculated using the rule of mixture, b = $\frac{\sqrt{3}}{2}a_{B2}$ is the modulus of Burgers vector for B2 phase with lattice parameter a_{B2}. The lattice misfit between the B2 and BCC phases is calculated by the following equations [61]:

$$\eta = \frac{d(lna)}{dC} = \frac{1}{a}\frac{da}{dC} \quad 3.13$$

$$\frac{da}{dC} = 2\left(\frac{a_{B2} - a_{BCC}}{a_{B2} + a_{BCC}}\right) \quad 3.14$$

A relatively high lattice misfit is required for an alloy to exhibit spinodal decomposition-based structures. High entropy alloy system AlCoCrFeNi having a similar spinodal structure has the lattice misfit of more than 0.5% [22,50]. The lattice misfit for the IM alloy was 0.91%, and for the SC alloy was 0.85%. Table 3.4 enlists the values of all the parameters associated with spinodal strengthening for each alloy. The value of $\Delta\sigma_{SD}$ was calculated from the Eq. 3.12 were ~77 MPa and ~68 MPa in the IM alloy and the SC alloy, respectively.

Table 3.5 shows the individual strength increments in both the alloys from all the strengthening effects- solid solution, grain boundary, dislocation interactions and spinodal decomposition. The yield strength predicted from the strengthening model in the IM alloy and the SC alloy is in good agreement with the experimental results. Therefore, the strength in the IM alloy is derived mostly from solid solution strengthening and spinodal strengthening, and the strength in the SC alloy is primarily contributed by the dislocation hardening. The deviation of predicted strength from the actual strength may have occurred due to the formation of defects, e.g., shrinkage cavities and impurities, during the alloy processing. Another reason for the difference in predicted and experimental strength is that the values considered for some of the material constants, k_y, G, ΔG *etc.*, were borrowed from established conventional alloys or HEAs with similar compositions [60,63,64,66]. The likelihood of any substructure formation and dislocation density accumulation during compression is further investigated in the next section to understand the plastic deformation behaviour of both alloys.

Table 3.4 Parameters used for spinodal decomposition strengthening $\Delta\sigma_{SD}$

Alloy	E (GPa)	$\frac{da}{dC}$ (%)	A (%)	a_{B2} (nm)	b (nm)	λ (nm)	Fraction %	$\Delta\sigma_{SD}$ (MPa)
IM	175	0.91	4.15	0.284	0.246	2000	15	77
SC	174	0.87	4.65	0.288	0.248	15	12	68

Table 3.5 Strength contributions of each strengthening mechanism

Alloy	$\Delta\sigma_{ss}$ (MPa)	$\Delta\sigma_{GB}$ (MPa)	$\Delta\sigma_{D}$ (MPa)	$\Delta\sigma_{SD}$ (MPa)	σ_0 (MPa)	σ_{total} (MPa)	$\sigma_{experimenntal}$ (MPa)
IM	65	5	0	77	114	261	250
SC	61	18	262	68	114	523	420

3.3.5 Deformation Mechanisms

The IPF image in Fig 3.7 (a) shows that the undeformed IM alloy sample possessed large grains of the order of 1000 μm. The interdendritic region was recognized as the BCC phase (as mentioned in the previous section) that spread uniformly in the form of a cellular network, and the dendritic region was identified as the FCC phase in the EBSD phase map of Fig. 3.7(c). The grain boundaries and heterogeneous phase boundaries were the microstructural discontinuities in the IM alloy. Interdendritic SD structures created highly misoriented heterogeneous phase boundaries with the FCC dendritic region, which can cause dislocation slip incompatibility across the boundaries. The misorientation between the dendritic and the interdendritic regions was as high as 60˚, and the misorientation across the grain boundaries was 15˚-20˚ in the IM alloy, as seen in the misorientation vs distance plots of Figs. 3.7(d) and 7(e). The highly misoriented intragranular FCC-BCC boundaries in the IM alloy led to superior mechanical properties compared to other single-phase FCC high entropy alloys despite the dual-phase IM alloy having a larger grain size [20,49].

The IPF image of the undeformed SC alloy in Fig. 3.8(a) shows a lamellar structure primarily with a wide variation in grain size ranging from ~50 µm in smaller grains to more than 500 µm in elongated grains. The average grain size of the SC structure was 153.6 ± 3 µm. Although the SC alloy has a lower volume fraction of the BCC phase compared to the IM alloy, the finer BCC phases in the SC alloy were distributed non-uniformly in large number (Fig. 3.8(c)) unlike the IM alloy. High angle grain boundaries (HAGB) were observed throughout the SC alloy sample. The misorientation angles calculated across grain boundaries and FCC-BCC phase boundaries were significantly high with angles measured above 50˚ as shown in Fig. 3.8(d) and 3.8(e). Thus, due to its finer grain size and a larger number of heterogeneous phase boundaries, the SC alloy showed a higher distribution of high angle misorientation barriers compared to the IM alloy resulting in higher strength.

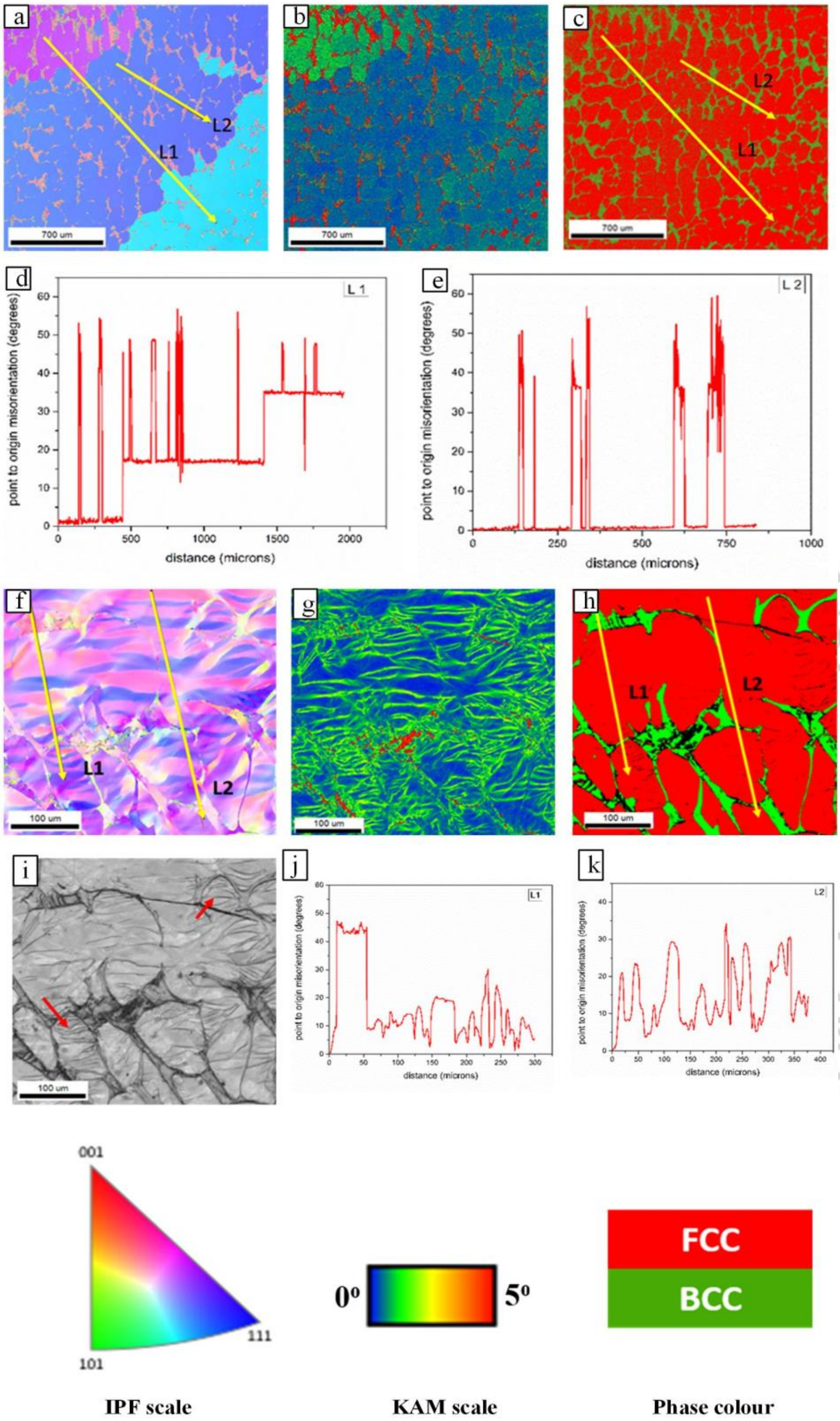

Figure 3.7 (a) IPF map (b) KAM map and (c) phase map of undeformed IM alloy; (f) IPF map (g) KAM map (h) phase map and (i) band contrast map of deformed IM alloy; misorientation vs distance plots of undeformed IM alloy (d, e) and deformed IM alloy (j, k). The IPF and KAM scale and phase color are shown at the

bottom of the figure.

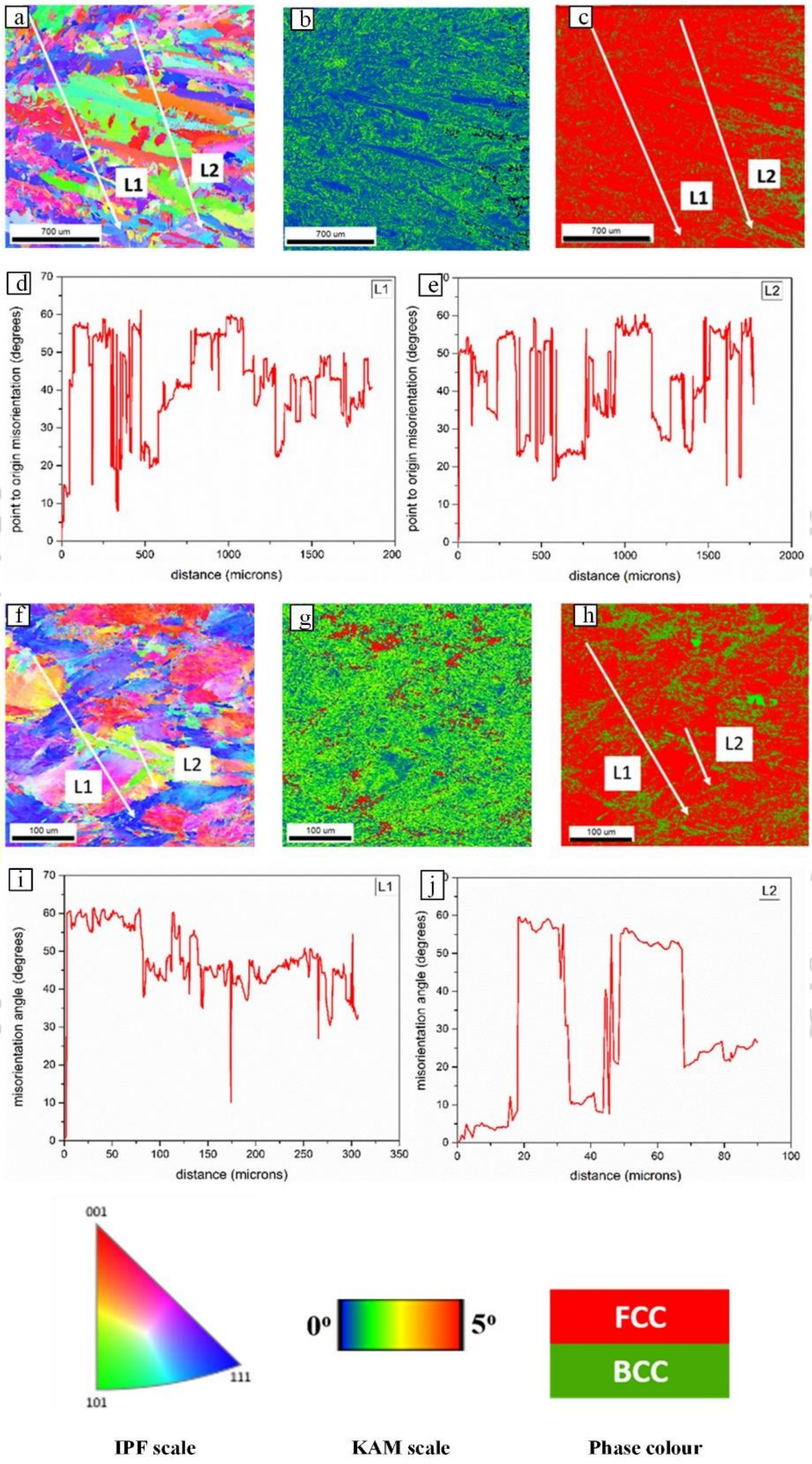

Figure 3.8 (a) IPF map (b) KAM map and (c) phase map of undeformed SC alloy; (f) IPF map (g) KAM map and (h) phase map of deformed SC alloy; misorientation vs distance plots of undeformed IM alloy (d, e) and

deformed IM alloy (i, j). The IPF and KAM scale and phase color are shown at the bottom of the figure.

The post-deformation analysis through IPF and misorientation vs distance plots having reference of point to origin of the IM and SC alloys are shown in Fig. 3.7 (f, j, k) and Fig 3.8 (f, i, j), respectively. The IPF image of the deformed IM alloy, in Fig. 3.7(f), shows many differential colour bands in the FCC matrix of the grain indicating intense slip activity. Slip band formation is a phenomenon that results out of the planar slip, and it occurs typically in HEAs due to their high lattice friction stress [67,68]. Slip band formation indicates intense slip activity, and the presence of profuse slip bands can contribute to a significant strengthening of the material by creating a zone of high dislocation density [37]. The band contrast map in Fig. 3.7(i) clearly shows the boundaries of the intragranular slip bands. The arrows drawn in the band contrast map displayed the high distribution of the slip band in regions enclosed by harder BCC phases (Fig 3.7(i)). The harder BCC phases restricted the plastic deformation of the enclosed FCC regions leading to high lattice rotation and hence slip band formation [37]. Figs. 3.7(j) and 3.7(k) clearly showed that the slip band boundaries were inclined in the <111> parallel to the compression direction and exhibited high misorientation, with a few of them exhibiting misorientation higher than 20˚. The absence of misorientation higher than 60° within the FCC dendritic region negate the formation of any twin boundaries and confirms the bands formed to be entirely due to slip band formation [69]. These slip band boundaries were higher in numbers than the grain boundaries and FCC-BCC phase boundaries, and hence, the strengthening contributions of the slip band boundaries were significant at strains higher than 15% in the IM alloy. This confirms the increase in strain hardening rate at large strains in the IM alloy as observed in the strain hardening rate plots as a function of true strain and flow stress in Figs. 3.4(b) and 3.4 (c) of the previous section. Thus, cold working can be used to enhance the strength of the IM alloy through slip band strengthening for high strength application. In contrast, the deformed SC alloy sample did not undergo substantial lattice rotation within grains to form slip bands, as seen from the IPF image in Fig. 83.(f) and misorientation vs distance plots in Figs. 3.8(i) and 3.8(j). Instead, the severe fluctuations in the SC alloy misorientation over a distance, as seen in the above-mentioned plot, is primarily due to the fine interdendritic regions within the eutectic lamellar structure observed distinctly in Fig 3.3(a) and (b).

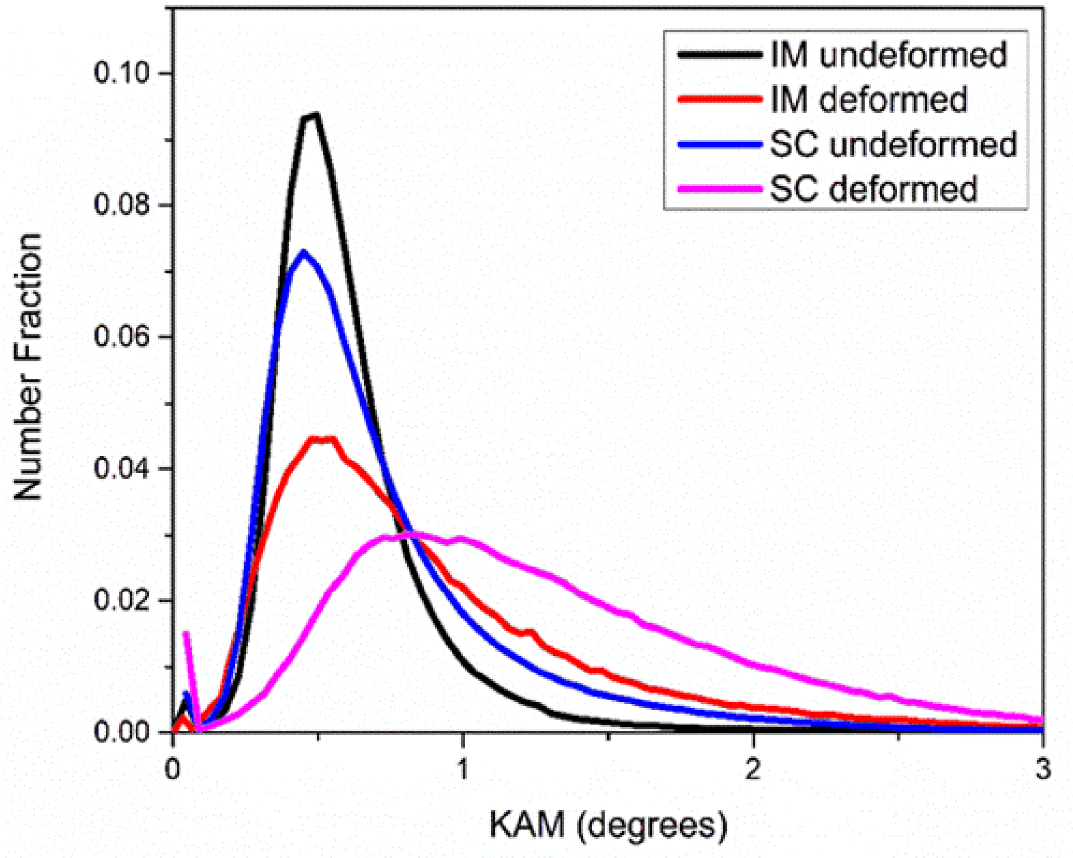

Figure 3.9 Number fraction vs KAM plots for undeformed and deformed IM and SC alloys

The KAM maps represent local misorientation and help in determining the extent of strain absorbed at different regions to locate the sites of dislocation accumulation. The angular scale at a pixel in the KAM map measured its average misorientation with five neighbouring pixels. The microstructural effects on plastic deformation is related to the generation of geometrically necessary dislocations (GNDs) in the material. The KAM maps are good indicators of GNDs [70,71], and the empirical relation between GNDs and KAM is $\rho_{GND} =$

$\frac{\alpha\, KAM}{bx}$, where ρ_{GND} is the density of GNDs, b is the magnitude of Burgers vector, α depends on the type of the grain boundary, and x is the scan-step size [72].

The KAM values of the undeformed IM alloy sample were higher at the interdendritic BCC region compared to dendritic regions as seen in Fig. 3.7(b). Fig. 3.7(g) shows high KAM values at the slip band boundaries of the deformed IM alloy sample. The high lattice rotation in the slip band regions resulted in high GNDs at the band boundaries, which can be inferred from high KAM values [62]. The KAM maps in Fig. 3.8(b) show that SC alloy had higher KAM values at the grain boundaries and the BCC-FCC phase before deformation. After the deformation, the KAM values were uniformly distributed across and within the grains of the SC alloy (Fig. 3.8(g)). Due to the absence of a network of large interdendritic regions and the presence of finer grains, the SC alloy exhibited a more homogeneous deformation compared to the IM alloy. The comparative KAM analysis of the IM and the SC alloys is shown in Fig. 3.9 through the number fraction vs KAM values. High microstrain produced in the SC alloy during alloy formation, which results in residual thermal stress in the alloy, led to overall broader number fraction vs KAM curve and higher values of KAM distribution as compared to the IM alloy [73]. Thus, the high microstrain developed in the SC alloy was the dominant factor in strengthening the alloy by high dislocation interactions.

3.4 Summary

The dual-phase high entropy alloy $Al_{0.65}CoCrFe_2Ni$ having both FCC and BCC phases was designed and fabricated using industrially melted large-scale and lab-scale methods having two different cooling rates of 10 K/s and 10^3 K/s, respectively. The mechanical properties, strengthening effects and deformation behaviour observed are summarized below.

(a) The yield strength and hardness improved significantly at a high cooling rate of solidification.

(b) The IM alloy exhibits higher spinodal strengthening, and the SC alloy shows higher grain boundary strengthening. However, the major strengthening contributor of high-strength SC alloy is dislocation hardening resulting from microstrain produced at a high cooling rate of alloy formation.

(c) The slip band formation in the IM alloy observed in orientation image maps is in good agreement with the increase in strain hardening rate at large strains.

This study is instrumental in understanding the difference in strengthening mechanisms involved in high entropy alloys processed at lab scale and industrial scale. The large-scale processing technique requires a higher cooling rate of solidification to achieve improved mechanical properties. In addition, cold working can be used to induce slip band formation to strengthen the industrially prepared high entropy alloy for potential high strength application.

References

[1] M.H. Tsai, J.W. Yeh, High-entropy alloys: A critical review, Mater. Res. Lett. 2 (2014) 107–123. https://doi.org/10.1080/21663831.2014.912690.

[2] C.T. Wang, Y. He, Z. Guo, X. Huang, Y. Chen, H. Zhang, Y. He, Strain Rate Effects on the Mechanical Properties of an AlCoCrFeNi High-Entropy Alloy, Met. Mater. Int. 27 (2021) 2310–2318. https://doi.org/10.1007/s12540-020-00920-5.

[3] X. Chen, D. Gao, Y. Zhang, J.X. Hu, Y. Liu, F. Xiang, Evolution of Microstructures and Compressive Properties in Al0.5CrFeNi2.1Mn0.8Tix High Entropy Alloys, Met. Mater. Int. 27 (2021) 118–126. https://doi.org/10.1007/s12540-020-00620-0.

[4] C.J. Tong, M.R. Chen, S.K. Chen, J.W. Yeh, T.T. Shun, S.J. Lin, S.Y. Chang, Mechanical performance of the AlxCoCrCuFeNi high-entropy alloy system with multiprincipal elements, Metall. Mater. Trans. A Phys. Metall. Mater. Sci. 36 (2005) 1263–1271. https://doi.org/10.1007/s11661-005-0218-9.

[5] W.H. Liu, Y. Wu, J.Y. He, T.G. Nieh, Z.P. Lu, Grain growth and the Hall-Petch relationship in a high-entropy FeCrNiCoMn alloy, Scr. Mater. 68 (2013) 526–529. https://doi.org/10.1016/j.scriptamat.2012.12.002.

[6] M.R. Chen, S.J. Lin, J.W. Yeh, S.K. Chen, Y.S. Huang, C.P. Tu, Microstructure and properties of Al0.5CoCrCuFeNiTix (x = 0-2.0) high-entropy alloys, in: Mater. Trans., 2006: p. Vol.47 No. 5 1396-1401. https://doi.org/10.2320/matertrans.47.1395.

[7] M.H. Chuang, M.H. Tsai, W.R. Wang, S.J. Lin, J.W. Yeh, Microstructure and wear behavior of AlxCo 1.5CrFeNi1.5Tiy high-entropy alloys, Acta Mater. 59 (2011) 6308–6317. https://doi.org/10.1016/j.actamat.2011.06.041.

[8] J.W. Yeh, Recent progress in high-entropy alloys, Ann. Chim. Sci. Des Mater. 31 (2006) 633–648. https://doi.org/10.3166/acsm.31.633-648.

[9] J.W. Yeh, Alloy design strategies and future trends in high-entropy alloys, JOM. 65 (2013) 1759–1771. https://doi.org/10.1007/s11837-013-0761-6.

[10] Y. Lu, X. Gao, L. Jiang, Z. Chen, T. Wang, J. Jie, H. Kang, Y. Zhang, S. Guo, H. Ruan, Y. Zhao, Z. Cao, T. Li, Directly cast bulk eutectic and near-eutectic high entropy alloys with balanced strength and ductility in a wide temperature range, Acta Mater. 124 (2017) 143–150. https://doi.org/10.1016/j.actamat.2016.11.016.

[11] J.J. Licavoli, M.C. Gao, J.S. Sears, P.D. Jablonski, J.A. Hawk, Microstructure and Mechanical Behavior of High-Entropy Alloys, J. Mater. Eng. Perform. 24 (2015) 3685–3698. https://doi.org/10.1007/s11665-015-1679-7.

[12] F.J. Wang, Y. Zhang, G.L. Chen, H.A. Davies, Cooling Rate and Size Effect on the Microstructure and Mechanical Properties of AlCoCrFeNi High Entropy Alloy, J. Eng. Mater. Technol. 131 (2009) 034501-1–3. https://doi.org/10.1115/1.3120387.

[13] L. Ma, C. Li, Y. Jiang, J. Zhou, L. Wang, F. Wang, T. Cao, Y. Xue, Cooling rate-dependent microstructure and mechanical properties of AlxSi0.2CrFeCoNiCu1−xhigh entropy alloys, J. Alloys Compd. 694 (2017) 61–67. https://doi.org/10.1016/j.jallcom.2016.09.213.

[14] Y. Lv, R. Hu, Z. Yao, J. Chen, D. Xu, Y. Liu, X. Fan, Cooling rate effect on microstructure and mechanical properties of AlxCoCrFeNi high entropy alloys, Mater. Des. 132 (2017) 392–399. https://doi.org/10.1016/j.matdes.2017.07.008.

[15] C.Y. Hsu, T.S. Sheu, J.W. Yeh, S.K. Chen, Effect of iron content on wear behavior of AlCoCrFexMo0.5Ni high-entropy alloys, Wear. 268 (2010) 653–659. https://doi.org/10.1016/j.wear.2009.10.013.

[16] Y. Yin, Q. Tan, T. Wang, D. Kent, N. Mo, M. Bermingham, H. Li, M.X. Zhang, Eutectic modification of Fe-enriched high-entropy alloys through minor addition of boron, J. Mater. Sci. 55 (2020) 14571–14587. https://doi.org/10.1007/s10853-020-05025-3.

[17] T.T. Shun, Y.C. Du, Microstructure and tensile behaviors of FCC Al0.3CoCrFeNi high entropy alloy, J. Alloys Compd. 479 (2009) 157–160. https://doi.org/10.1016/j.jallcom.2008.12.088.

[18] T. Yang, S. Xia, S. Liu, C. Wang, S. Liu, Y. Zhang, J. Xue, S. Yan, Y. Wang, Effects of AL addition on microstructure and mechanical properties of AlxCoCrFeNi High-entropy alloy, Mater. Sci. Eng. A. 648 (2015) 15–22. https://doi.org/10.1016/j.msea.2015.09.034.

[19] C. Li, J.C. Li, M. Zhao, Q. Jiang, Effect of aluminum contents on microstructure and properties of Al xCoCrFeNi alloys, J. Alloys Compd. 504 (2010) 515–518. https://doi.org/10.1016/j.jallcom.2010.03.111.

[20] Z. Li, S. Zhao, H. Diao, P.K. Liaw, M.A. Meyers, High-velocity deformation of Al0.3 CoCrFeNi high-entropy alloy: Remarkable resistance to shear failure, Sci. Rep. 7 (2017) 1–8. https://doi.org/10.1038/srep42742.

[21] Z. Tang, T. Yuan, C.W. Tsai, J.W. Yeh, C.D. Lundin, P.K. Liaw, Fatigue behavior of a wrought Al0.5CoCrCuFeNi two-phase high-entropy alloy, Acta Mater. 99 (2015) 247–258. https://doi.org/10.1016/j.actamat.2015.07.004.

[22] Q. Wang, Y. Ma, B. Jiang, X. Li, Y. Shi, C. Dong, P.K. Liaw, A cuboidal B2 nanoprecipitation-enhanced body-centered-cubic alloy Al0.7CoCrFe2Ni with prominent tensile properties, Scr. Mater. 120 (2016) 85–89. https://doi.org/10.1016/j.scriptamat.2016.04.014.

[23] M.A. Hemphill, T. Yuan, G.Y. Wang, J.W. Yeh, C.W. Tsai, A. Chuang, P.K. Liaw, Fatigue behavior of Al 0.5CoCrCuFeNi high entropy alloys, Acta Mater. 60 (2012) 5723–5734. https://doi.org/10.1016/j.actamat.2012.06.046.

[24] F. Otto, A. Dlouhý, K.G. Pradeep, M. Kuběnová, D. Raabe, G. Eggeler, E.P. George, Decomposition of the single-phase high-entropy alloy CrMnFeCoNi after prolonged anneals at intermediate temperatures, Acta Mater. 112 (2016) 40–52. https://doi.org/10.1016/j.actamat.2016.04.005.

[25] F. Otto, Y. Yang, H. Bei, E.P. George, Relative effects of enthalpy and entropy on the phase stability of equiatomic high-entropy alloys, Acta Mater. 61 (2013) 2628–2638. https://doi.org/10.1016/j.actamat.2013.01.042.

[26] F. He, Z. Wang, Q. Wu, J. Li, J. Wang, C.T. Liu, Phase separation of metastable CoCrFeNi high entropy alloy at intermediate temperatures, Scr. Mater. 126 (2017) 15–19. https://doi.org/10.1016/j.scriptamat.2016.08.008.

[27] T. Guo, J. Li, J. Wang, W.Y. Wang, Y. Liu, X. Luo, H. Kou, E. Beaugnon, Microstructure and properties of bulk Al0.5CoCrFeNi high-entropy alloy by cold rolling and subsequent annealing, Mater. Sci. Eng. A. 729 (2018) 141–148. https://doi.org/10.1016/j.msea.2018.05.054.

[28] Y. Lu, Y. Dong, S. Guo, L. Jiang, H. Kang, T. Wang, B. Wen, Z. Wang, J. Jie, Z. Cao, H. Ruan, T. Li, A promising new class of high-temperature alloys: Eutectic high-entropy alloys, Sci. Rep. 4 (2014) 1–5. https://doi.org/10.1038/srep06200.

[29] G. Liu, L. Liu, X. Liu, Z. Wang, Z. Han, G. Zhang, A. Kostka, Microstructure and mechanical properties of Al0.7CoCrFeNi high-entropy-alloy prepared by directional solidification, Intermetallics. 93 (2018) 93–100. https://doi.org/10.1016/j.intermet.2017.11.019.

[30] Q. Wang, T. Gao, H. Du, Q. Hu, Q. Chen, Z. Fan, L. Zeng, X. Liu, Hot compression behaviors and microstructure evolutions of a cast dual-phase NiCoFeCrAl0.7 high-entropy alloy, Intermetallics. 138 (2021) 107314. https://doi.org/10.1016/j.intermet.2021.107314.

[31] L. Wang, C. Yao, J. Shen, Y. Zhang, T. Wang, Y. Ge, L. Gao, G. Zhang, Microstructures and room temperature tensile properties of as-cast and directionally solidified AlCoCrFeNi2.1 eutectic high-entropy alloy, Intermetallics. 118 (2020) 106681. https://doi.org/10.1016/j.intermet.2019.106681.

[32] J. Yi, L. Yang, L. Wang, M. Xu, Novel, Equimolar, Multiphase CoCuNiTiV High-Entropy Alloy: Phase Component, Microstructure, and Compressive Properties, Met. Mater. Int. 27 (2021) 2387–2394. https://doi.org/10.1007/s12540-020-00923-2.

[33] P. Sathiyamoorthi, H.S. Kim, High-entropy alloys with heterogeneous microstructure: Processing and mechanical properties, Prog. Mater. Sci. 123 (2022) 100709.

https://doi.org/10.1016/j.pmatsci.2020.100709.

[34] Y. Lu, Y. Dong, H. Jiang, Z. Wang, Z. Cao, S. Guo, T. Wang, T. Li, P.K. Liaw, Promising properties and future trend of eutectic high entropy alloys, Scr. Mater. 187 (2020) 202–209. https://doi.org/10.1016/j.scriptamat.2020.06.022.

[35] X. Jin, Y. Liang, J. Bi, B. Li, Enhanced strength and ductility of Al0.9CoCrNi2.1 eutectic high entropy alloy by thermomechanical processing, Materialia. 10 (2020) 100639. https://doi.org/10.1016/j.mtla.2020.100639.

[36] I. Basu, J.T.M. De Hosson, Strengthening mechanisms in high entropy alloys: Fundamental issues, Scr. Mater. 187 (2020) 148–156. https://doi.org/10.1016/j.scriptamat.2020.06.019.

[37] D.L. Foley, S.H. Huang, E. Anber, L. Shanahan, Y. Shen, A.C. Lang, C.M. Barr, D. Spearot, L. Lamberson, M.L. Taheri, Simultaneous twinning and microband formation under dynamic compression in a high entropy alloy with a complex energetic landscape, Acta Mater. 200 (2020) 1–11. https://doi.org/10.1016/j.actamat.2020.08.047.

[38] Y. Zhang, X. Yang, P.K. Liaw, Alloy design and properties optimization of high-entropy alloys, JOM. 64 (2012) 830–838. https://doi.org/10.1007/s11837-012-0366-5.

[39] X. Yang, S.Y. Chen, J.D. Cotton, Y. Zhang, Phase Stability of Low-Density, Multiprincipal Component Alloys Containing Aluminum, Magnesium, and Lithium, JOM. 66 (2014) 2009–2020. https://doi.org/10.1007/s11837-014-1059-z.

[40] X. Yang, Y. Zhang, Prediction of high-entropy stabilized solid-solution in multi-component alloys, Mater. Chem. Phys. 132 (2012) 233–238. https://doi.org/10.1016/j.matchemphys.2011.11.021.

[41] M.H. Tsai, K.Y. Tsai, C.W. Tsai, C. Lee, C.C. Juan, J.W. Yeh, Criterion for sigma phase formation in Cr- and V-Containing high-entropy alloys, Mater. Res. Lett. 1 (2013) 207–212. https://doi.org/10.1080/21663831.2013.831382.

[42] Website, www.atex-software.eu, (n.d.). http://www.atex-software.eu/ (accessed December 25, 2021).

[43] I.S. Wani, T. Bhattacharjee, S. Sheikh, P.P. Bhattacharjee, S. Guo, N. Tsuji, Tailoring nanostructures and mechanical properties of AlCoCrFeNi2.1 eutectic high entropy alloy using thermo-mechanical processing, Mater. Sci. Eng. A. 675 (2016) 99–109. https://doi.org/10.1016/j.msea.2016.08.048.

[44] Y. Zhang, S.G. Ma, J.W. Qiao, Morphology transition from dendrites to equiaxed grains for AlCoCrFeNi high-entropy alloys by copper mold casting and bridgman solidification, Metall. Mater. Trans. A Phys. Metall. Mater. Sci. 43A (2012) 2625–2630. https://doi.org/10.1007/s11661-011-0981-8.

[45] W.R. Wang, W.L. Wang, S.C. Wang, Y.C. Tsai, C.H. Lai, J.W. Yeh, Effects of Al addition on the microstructure and mechanical property of Al xCoCrFeNi high-entropy alloys, Intermetallics. 26 (2012) 44–51. https://doi.org/10.1016/j.intermet.2012.03.005.

[46] S. Das, S.K. Nishad, P.S. Robi, A New High-Entropy Alloy of Al–Fe–Co–Ni–Cu Possessing Single Face-Centered Cubic Crystal Structure and Excellent Mechanical Properties at Room Temperature, Phys. Status Solidi Appl. Mater. Sci. 218 (8) (2021) 2000825. https://doi.org/10.1002/pssa.202000825.

[47] I. Basu, V. Ocelík, J.T.M. De Hosson, Size dependent plasticity and damage response in multiphase body centered cubic high entropy alloys, Acta Mater. 150 (2018) 104–116. https://doi.org/10.1016/j.actamat.2018.03.015.

[48] A. Shafiei, Design of Eutectic High Entropy Alloys in Al–Co–Cr–Fe–Ni System, Met. Mater. Int. 27 (2021) 127–138. https://doi.org/10.1007/s12540-020-00655-3.

[49] N. Kumar, Q. Ying, X. Nie, R.S. Mishra, Z. Tang, P.K. Liaw, R.E. Brennan, K.J. Doherty, K.C. Cho, High strain-rate compressive deformation behavior of the Al0.1CrFeCoNi high entropy alloy, Mater. Des. 86 (2015) 598–602. https://doi.org/10.1016/j.matdes.2015.07.161.

[50] Y. Ma, B. Jiang, C. Li, Q. Wang, C. Dong, P.K. Liaw, F. Xu, L. Sun, The BCC/B2 morphologies in AlxNiCoFeCr high-entropy alloys, Metals (Basel). 7 (2017) 57. https://doi.org/10.3390/met7020057.

[51] Y. Lv, R. Hu, Z. Yao, J. Chen, D. Xu, Y. Liu, X. Fan, Cooling rate effect on microstructure and mechanical properties of AlxCoCrFeNi high entropy alloys, Mater. Des. (2017).

https://doi.org/10.1016/j.matdes.2017.07.008.

[52] H. Mecking, U.F. Kocks, Kinetics of flow and strain-hardening, Acta Metall. 29 (1981) 1865–1875. https://doi.org/10.1016/0001-6160(81)90112-7.

[53] U.F. Kocks, Laws for work-hardening and low-temperature creep, J. Eng. Mater. Technol. Trans. ASME. 98 (1976) 76–85. https://doi.org/10.1115/1.3443340.

[54] U.F. Kocks, H. Mecking, Physics and phenomenology of strain hardening: The FCC case, Prog. Mater. Sci. 48 (2003) 171–273. https://doi.org/10.1016/S0079-6425(02)00003-8.

[55] N. Afrin, D.L. Chen, X. Cao, M. Jahazi, Strain hardening behavior of a friction stir welded magnesium alloy, Scr. Mater. 57 (2007) 1004–1007. https://doi.org/10.1016/j.scriptamat.2007.08.001.

[56] N.R. Risebrough, E. Teghtsoonian, THE LINEAR HARDENING OF CADMIUM, Can. J. Phys. 45 (1967) 591–605. https://doi.org/10.1139/p67-051.

[57] Y. Zhang, Q. Shen, X. Chen, S. Jayalakshmi, R.A. Singh, S. Konovalov, V.B. Deev, E.S. Prusov, Strengthening mechanisms in cocrfenix0.4 (al, nb, ta) high entropy alloys fabricated by powder plasma arc additive manufacturing, Nanomaterials. 11 (2021) 1–14. https://doi.org/10.3390/nano11030721.

[58] I. Basu, V. Ocelík, J.T.M. De Hosson, BCC-FCC interfacial effects on plasticity and strengthening mechanisms in high entropy alloys, Acta Mater. 157 (2018) 83–95. https://doi.org/10.1016/j.actamat.2018.07.031.

[59] R. Sriharitha, B.S. Murty, R.S. Kottada, Alloying, thermal stability and strengthening in spark plasma sintered AlxCoCrCuFeNi high entropy alloys, J. Alloys Compd. 583 (2014) 419–426. https://doi.org/10.1016/j.jallcom.2013.08.176.

[60] Y. Ma, J. Hao, J. Jie, Q. Wang, C. Dong, Coherent precipitation and strengthening in a dual-phase AlNi2Co2Fe1.5Cr1.5 high-entropy alloy, Mater. Sci. Eng. A. 764 (2019) 138241. https://doi.org/10.1016/j.msea.2019.138241.

[61] Q. Tian, G. Zhang, K. Yin, W. Wang, W. Cheng, Y. Wang, The strengthening effects of relatively lightweight AlCoCrFeNi high entropy alloy, Mater. Charact. 151 (2019) 302–309. https://doi.org/10.1016/j.matchar.2019.03.006.

[62] A.A. Tiamiyu, V. Tari, J.A. Szpunar, A.G. Odeshi, A.K. Khan, Effects of grain refinement on the quasi-static compressive behavior of AISI 321 austenitic stainless steel: EBSD, TEM, and XRD studies, Int. J. Plast. 107 (2018) 79–99. https://doi.org/10.1016/j.ijplas.2018.03.014.

[63] J.Y. He, H. Wang, H.L. Huang, X.D. Xu, M.W. Chen, Y. Wu, X.J. Liu, T.G. Nieh, K. An, Z.P. Lu, A precipitation-hardened high-entropy alloy with outstanding tensile properties, Acta Mater. 102 (2016) 187–196. https://doi.org/10.1016/j.actamat.2015.08.076.

[64] R.S. Ganji, P. Sai Karthik, K. Bhanu Sankara Rao, K. V. Rajulapati, Strengthening mechanisms in equiatomic ultrafine grained AlCoCrCuFeNi high-entropy alloy studied by micro- and nanoindentation methods, Acta Mater. 125 (2017) 58–68. https://doi.org/10.1016/j.actamat.2016.11.046.

[65] Z. Wu, H. Bei, G.M. Pharr, E.P. George, Temperature dependence of the mechanical properties of equiatomic solid solution alloys with face-centered cubic crystal structures, Acta Mater. 81 (2014) 428–441. https://doi.org/10.1016/j.actamat.2014.08.026.

[66] R.K. Song, L.J. Wei, C.X. Yang, S.J. Wu, Phase formation and strengthening mechanisms in a dual-phase nanocrystalline CrMnFeVTi high-entropy alloy with ultrahigh hardness, J. Alloys Compd. 744 (2018) 552–560. https://doi.org/10.1016/j.jallcom.2018.02.029.

[67] F. Otto, A. Dlouhý, C. Somsen, H. Bei, G. Eggeler, E.P. George, The influences of temperature and microstructure on the tensile properties of a CoCrFeMnNi high-entropy alloy, Acta Mater. 61 (2013) 5743–5755. https://doi.org/10.1016/j.actamat.2013.06.018.

[68] Z. Wang, I. Baker, Z. Cai, S. Chen, J.D. Poplawsky, W. Guo, The effect of interstitial carbon on the mechanical properties and dislocation substructure evolution in Fe40.4Ni11.3Mn34.8Al7.5Cr6 high entropy alloys, Acta Mater. 120 (2016) 228–239. https://doi.org/10.1016/j.actamat.2016.08.072.

[69] T. Liu, Y. Gao, H. Bei, K. An, In situ neutron diffraction study on tensile deformation behavior of

carbon-strengthened CoCrFeMnNi high-entropy alloys at room and elevated temperatures, J. Mater. Res. 33 (2018) 3192–3203. https://doi.org/10.1557/jmr.2018.180.

[70] P.J. Konijnenberg, S. Zaefferer, D. Raabe, Assessment of geometrically necessary dislocation levels derived by 3D EBSD, Acta Mater. 99 (2015) 402–414. https://doi.org/10.1016/j.actamat.2015.06.051.

[71] R. Sonkusare, A. Swain, M.R. Rahul, S. Samal, N.P. Gurao, K. Biswas, S.S. Singh, N. Nayan, Establishing processing-microstructure-property paradigm in complex concentrated equiatomic CoCuFeMnNi alloy, Mater. Sci. Eng. A. 759 (2019) 415–429. https://doi.org/10.1016/j.msea.2019.04.096.

[72] A. Das, S. Tarafder, S. Sivaprasad, D. Chakrabarti, Influence of microstructure and strain rate on the strain partitioning behaviour of dual phase steels, Mater. Sci. Eng. A. 754 (2019) 348–360. https://doi.org/10.1016/j.msea.2019.03.084.

[73] J. Xu, J. Li, D. Shan, B. Guo, Strain softening mechanism at meso scale during micro-compression in an ultrafine-grained pure copper, AIP Adv. 5 (2015) 097147. https://doi.org/10.1063/1.4931382.

Chapter 4 High strain rate deformation of industrially melted as-cast dual-phase high entropy alloy

4.1 Introduction

In this study, the strain rate effects of a dual-phase HEA $Al_{0.65}CoCrFe_2Ni$ having FCC and BCC/B2 phases fabricated at large scale under industrial conditions was investigated. for the alloy was designed with high Fe content for improved plasticity, inhibition of sigma phases and cost effectiveness[1]. The stress-strain response and strain-hardening behaviour of the as-cast alloy under high strain rate loading at room temperature and high temperature were examined. The deformation substructures and strain partitioning in the dual-phase HEA under high strain rate loading were analysed using orientation image mapping (OIM). Further, the dislocation interactions under dynamic loading were also studied using transmission electron microscopy (TEM). The plasticity behaviour under high strain rate was predicted using Johnson Cook (J-C) constitutive model. This chapter is instrumental in understanding the nature of large as-cast alloy under dynamic loading as well as lay foundation for necessary adjustments for similar strain rate of loadings.

4.2 Choice of the experimental conditions

The high entropy alloy $Al_{0.65}CoCrFe_2Ni$ was designed to have both FCC and BCC phases maintaining a high Fe content. The enthalpy of mixing (ΔH_{mix}), configurational entropy (ΔS) and size effect (δ) of the alloy were calculated as $-12.264\ KJ/mol$, 1.535 R (gas constant) and 4.67%, respectively. The overall combined effect (Ω) of entropy, enthalpy and size effect was calculated to be greater than 1.1. The design considerations were made in such a way that all the above theoretical values adhered to the definition of high entropy alloy[2–4]. The valence electron concentration (VEC) criteria of 6.4<VEC<8.5 required for dual FCC-BCC phase HEAs was also maintained (VEC=7.626) to obtain both FCC and BCC phases in the alloy [5,6]. The as-cast alloy was prepared in an industrial-scale vacuum induction melting setup at Mishra Dhatu Nigam Limited, (MIDHANI) Hyderabad. The furnace consisted of a 60kg crucible having alumina lining. The melting was performed in an argon atmosphere of 10^{-2} mbar for half an hour. Electromagnetic stirring was used to maintain the homogeneity of the melt pool. After the complete meltdown and stirring, the liquid melt was poured in a rectangular shaped mould located inside the argon chamber. An appropriate riser was designed and attached on the top of the mould of the cast to ensure defect-free condition. The cast was placed in the furnace chamber under argon atmosphere for a few hours to complete solidification. The cooling rate of solidification during this processing was ~10 K/s. The slow cooling of solidification ensured low residual thermal stress as reported in a previous work published by the authors [7].

Microstructural evaluation and phase identification for the alloy were exercised using X-ray diffraction (XRD) and scanning electron microscopy (SEM) techniques. The XRD analysis have been performed with Cu-k_α radiation (λ=1.5406 $A°$) operating at 50kV/160mA in a Rigaku made instrument. Field emission scanning electron microscope (FE-SEM) make Zeiss model Sigma integrated with energy dispersive spectroscopy (EDS) detectors make Oxford have been used to examine the microstructure as well as elemental mapping at different locations. Oxford Instruments made electron backscatter diffraction (EBSD) probe integrated with FE-SEM were used to identify the phases and grains and substructures in the alloy before and after deformation under dynamic loading. The orientation image maps have been generated using TSL-OIM software and ATEX software [8]. Transmission electron microscopy technique was also employed to find any probable ordered phase and deformation substructure present in the alloy.

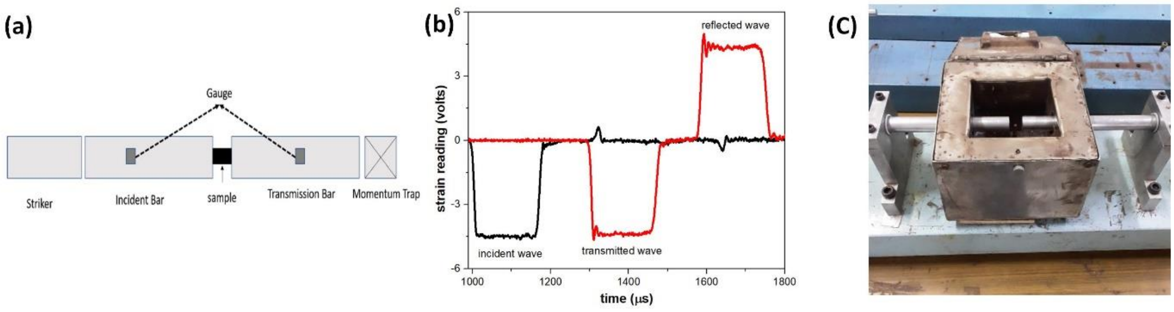

Figure 4.1 (a) Schematic illustration of SHPB setup used for high strain rate compression test, (b) typical wave forms of incident, transmitted and reflected signals obtained during the test and (c) specimen inside a furnace attached to the SHPB setup for high strain rate tests at high temperatures

A cylindrical sample of the alloy having dimensions of 6 mm diameter and 6 mm height was compressed under quasi-static conditions at strain rates ~ 10^{-4} s^{-1} and 10^{-2} s^{-1} at room temperature using Instron 8801 universal testing machine. The high strain rate deformation behaviour was tested using a split Hopkinson pressure bar (SHPB) setup at Indian Institute of Technology Kanpur. The dimensions of the cylindrical samples were 6mm diameter and 5 mm height. The schematic of the SHPB set up is shown in Fig 4.1(a). The two half-bridge strain gauges were mounted in a diametrically opposite arrangement on the incident bar and the transmission bar. The wave form recorded in the oscilloscope generated by an impact on the alloy sample at a strain rate 2350 s^{-1} is displayed in Fig 4.1(b). The engineering stress (σ_S), engineering strain (ε_S) and strain rate ($\dot{\varepsilon}_S$) under high strain rate loading conditions follow the one-dimensional elastic wave theory and are given by the equations given in previous section Eq. 2.3, 2.4 and 2.5 [9].

The high strain rate tests under high temperature conditions were performed by placing a furnace in between the incident bar and the transmitted bar as shown in Fig. 4.1(c). The temperatures at which the dynamic deformation conducted were 373 K, 423 K and 473 K, and the time taken by the furnace to reach the respective temperatures were 18 minutes, 26 minutes and 34 minutes. At least three samples were tested for each of the compression tests under quasi-static, high strain rate and high-temperature high strain rate conditions.

4.3 Results and discussion

Experiments are carried out to investigate the effects of high strain rate loading on the as-cast alloy samples and associated deformation mechanisms.

4.3.1 Phase and Microstructural Analysis

The XRD analysis of the as-cast alloy in Fig. 4.2(a) confirmed the presence of both FCC phase and BCC/B2 phase. The lattice parameter for FCC phase was 3.84 Å and that of the BCC/B2 phase was 2.86 Å. The microstructure of the alloy was of dendritic nature as seen in Fig. 2(b) with the interdendritic region having maze like spinodal decomposition (SD) based structure (Fig. 4.2(c)). The IPF map obtained from EBSD analysis in Fig. 4.2(d) revealed that the size of the grains was of the order of 1000 μm. The phase map shown in Fig. 4.2(e) corroborated the XRD results and displayed the presence of FCC phase (area fraction ~84%) in the dendritic region and BCC phase in the interdendritc region (area fraction ~15%) of the alloy respectively. The EDS analysis at different locations of the alloy including the SD structure is shown in Fig. 4.2(f). The bright dendritic FCC region, i.e. spectrum 1, is rich in Fe and Cr with low percentages of Al and Ni, whereas the BCC-based interdendritic region, i.e. spectrum 2, is rich in Ni and Al with low percentages of Fe and Cr. Within the interdendritic SD structure, the bright region consists of high Ni and Al and the dark region consists of high Fe and Cr. The spatial fluctuation of composition of the interdendritic BCC region is as per the definition of spinodal structure [7,10,11] and similar microstructures were also observed in AlCoCrFeNi equimolar alloys [12,13]. Figs. 4.2(g) and 4.2(h) represent dark-field TEM image and the corresponding selected area electron diffraction (SAED) pattern of the as-cast alloy, respectively. The dark-field image of the spinodally decomposed interdendritic region (Fig. 4.2(g)) and its SAED pattern (Fig. 4.2(h)) confirm that the dark regions correspond to the BCC phase and the brighter regions resulting from weak (100) diffraction correspond to the B2 phase, which reaffirms the XRD findings of Fig. 4.2(a).

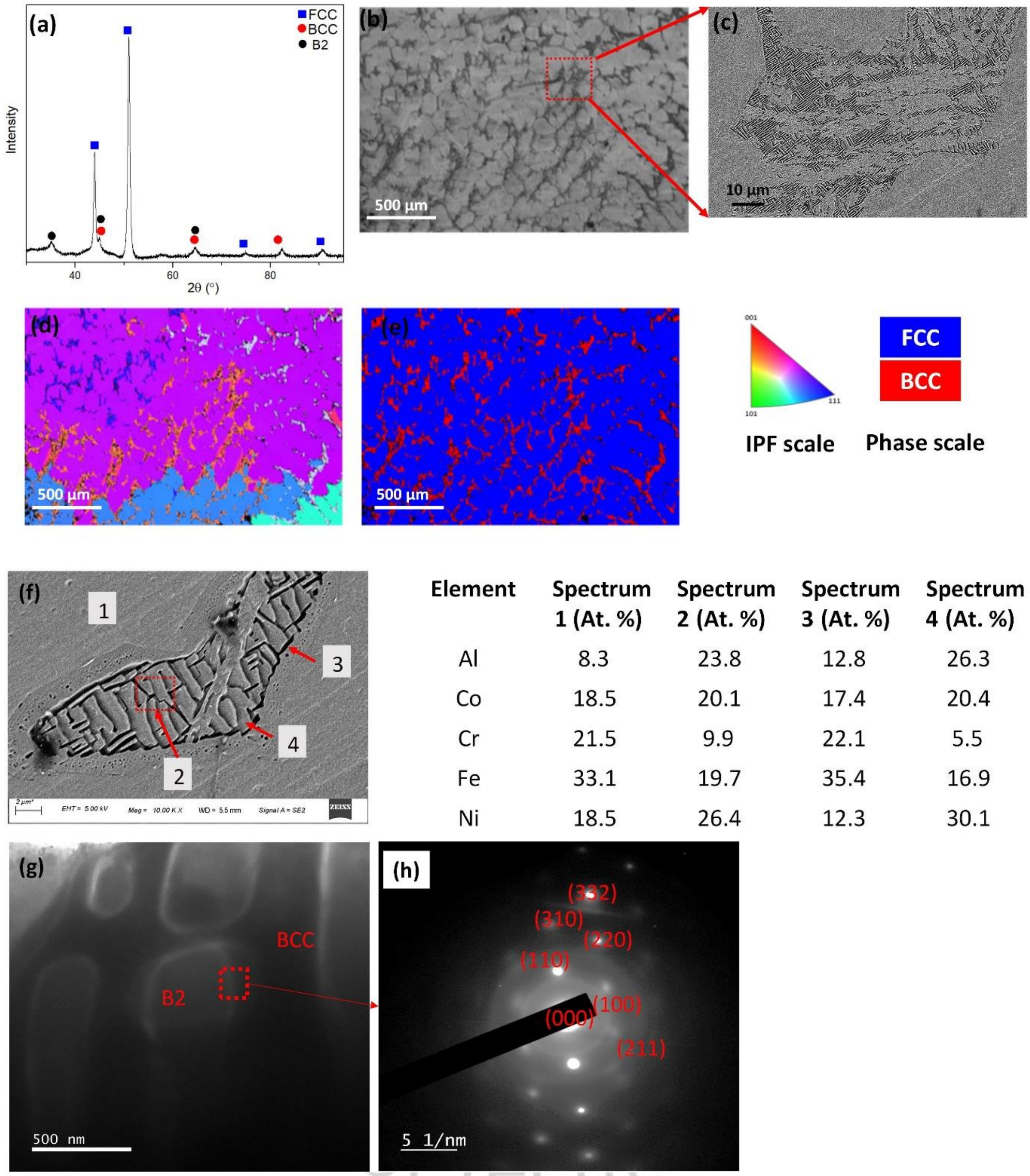

Element	Spectrum 1 (At. %)	Spectrum 2 (At. %)	Spectrum 3 (At. %)	Spectrum 4 (At. %)
Al	8.3	23.8	12.8	26.3
Co	18.5	20.1	17.4	20.4
Cr	21.5	9.9	22.1	5.5
Fe	33.1	19.7	35.4	16.9
Ni	18.5	26.4	12.3	30.1

Figure 4.2 (a) the XRD pattern of as-cast alloy, (b,c) SEM and magnified SEM images of as-cast alloy showing the dendritic microstructure and the interdendritic spinodal structure, (d) IPF image of the alloy, (e) phase map showing FCC dendritic region and BCC interdendritic region, (f) the elemental composition at different locations in the dendritic and interdendritic regions obtained from EDS analysis, and (g,h) TEM dark-field (DF) image of the interdendritic region and its corresponding SAED pattern showing the presence of

BCC phase and ordered B2 phase.

4.3.2 Mechanical Response

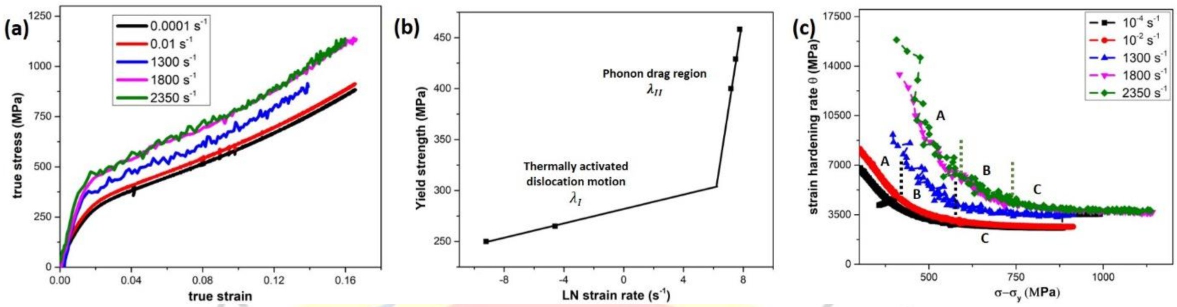

Figure 4.3 Stress strain plots from quasi static compression testing and dynamic deformation using SHPB (b) Varying yield strength with strain rates indicating two distinct regions (c) Kocks-Mecking (K-M) plots showing the variation of strain hardening rate (θ) with flow stress

The quasi-static and the high strain rate stress-strain responses of the as-cast alloy $Al_{0.65}CoCrFe_2Ni$ are compared under a range of strain rates is shown in Fig. 4.3(a). The quasi-static yield strengths of the alloy at strain rates of ~10^{-4} s^{-1} and ~10^{-2} s^{-1} were 250±5 MPa and 265±12 MPa, respectively. The high strain rate compression tests using SHPB were conducted at strain rates of ~1300 s^{-1}, ~1800 s^{-1} and ~2350 s^{-1}, and the respective yield strengths were 400±5 MPa, 429 ±15 MPa and 458±8 MPa. The specimens exhibited considerable ductility without failure under all strain rates. The serrated behavior of stress-strain curve was observed at high strain rate loading, which is a phenomenon of plastic instability that occurs during high temperature deformation or high strain rate deformation. In particular, during a high strain rate deformation, the complex wave interactions, solute-dislocation interaction, local fluctuation of stress and segregation of elemental composition [14–16]. The increase in average yield strength with increase in strain rate from 10^{-4} s^{-1} to 2350 s^{-1} was more than 80 %, exhibiting excellent strain rate hardening, which is typical of low stacking fault energy (SFE) alloys like 304L SS and Cu_xAl_y alloys [17].

The slope of the semi-logarithmic yield strength vs. strain rate plot, $\lambda = \frac{\partial \sigma}{\partial \, In \dot{\varepsilon}}$, shown in Fig

4.3(b), shows significantly higher strain rate hardening in the high strain rate region compared to quasi-static loading. The slope in the quasi-static region (λ_I) and in the dynamic region (λ_{II}) were calculated as 3.65 and 90.31, respectively. The difference in strain rate hardening of the alloy under quasi-static and high strain rate loading can be explained on the basis of dislocation activities in the alloy. Generally, the long-range and short-range barriers resist dislocation movements and hinder plastic deformation. Under quasi-static loading, due to the difference in size of the solute atoms in HEAs, the distorted lattice acts as short range barriers to restrict dislocation movements [18,19]. These short-range barriers can be overcome by reaching the thermal activation energy. For the lower slope in the quasi-static region, the thermal-activation dislocation theory was employed to understand the low strain rate sensitivity. The equation for thermal activation energy (ΔG), i.e. Gibbs free energy, is given below in the following equation[20,21]:

$$\Delta G = kT \left(ln \frac{\dot{\varepsilon}_0}{\dot{\varepsilon}}\right) \qquad 4.1$$

where $\dot{\varepsilon}_0$ is the reference strain rate, $\dot{\varepsilon}$ is the strain rate, k is the Boltzmann constant and T is the temperature.

Eq. 4.1 ascertain that the higher is the strain rate $\dot{\varepsilon}$, the lower is the thermal activation energy ΔG needed for the dislocation to overcome the barriers. Furthermore, the activation volume (V^*) is related to the Gibbs free energy as $V^* = \frac{\partial \, \Delta G}{\partial \, \tau^*}$, where τ^* is the effective thermal component of shear. Using Von Mises criterion for yielding, i.e., the relation between shear stress and normal stress $\tau = \frac{\sigma}{\sqrt{3}}$, the activation volume can be expressed as [17,22]

$$V^* = \sqrt{3}\, kT \frac{\partial\, ln\dot{\varepsilon}}{\partial\sigma} = \sqrt{3}\, kT \frac{\partial\, ln\sigma}{m\, \partial\sigma} \qquad 4.2$$

where m is the logarithmic strain rate sensitivity (SRS) (m= $\frac{\partial\, ln\sigma}{\partial\, In\dot{\varepsilon}}$).

Thus, the activation volume for HEAs derived from the above Eq. 4.2, lie between (1-100 b^3) which is significantly smaller compared to conventional FCC metals such as Cu, Cu-Zn [23,24]. The smaller activation volume is attributed to high lattice friction stress and solid solution pinning effect. This contributes to high dislocation interactions resulting in substructures formation [17,23].

The quasi-static deformation process involves thermal activation of dislocation movement. However, for dynamic deformations, the viscoelastic phonon-drag effect play the dominant role in the deformation process because of the following reasons[20,25,26]:

(a) Instantaneous increase in temperature at dynamic deformation will reduce the activation energy ΔG significantly.

(b) Dynamic deformation is transient in nature and hence cannot fully utilize the thermal activation energy.

Armstrong *et al.* has proposed the Orowan model to accurately determine the plastic behaviour of the metals under shock wave loading, which can be expressed as [25–27]:

$$\frac{d\varepsilon}{dt} = \frac{1}{m}.\rho b v = \frac{1}{m}.\frac{d\rho}{dt} b\Delta x_d \qquad 4.3$$

where $\frac{d\varepsilon}{dt}$ is the strain rate; m is the orientation factor, b is the Burgers vector, ρ is the mobile dislocation density, v is the dislocation velocity and Δx_d is the separation between dislocation generation. From Eq. 4.3, it can be inferred that higher strain rate of loading leads to higher dislocation velocity. The dislocation velocity at very high strain rates approach the shear wave velocity. The dislocation velocity is related to the frictional force (f) per unit length and the shear stress (τ) during high strain rate loading as given below.

$$f = b\tau = \eta v \tag{4.4}$$

,where η is the drag coefficient. This phonon-drag effect, which becomes operative in the high strain rate deformation, leads to a significant rise in the yield stresses.

The high lattice distortions inherently present in the HEAs also develop local elastic stress field, which interacts with the dislocation stress field, and these interactions impede the dislocation movements under high strain rate loading[28]. The higher strength and the higher strain hardening rate under high strain rate loading can be understood with the help of Taylor equation as given below.

$$v = A\sigma^m \tag{4.5}$$

,where A and m are material constants.

The overall strain rate sensitivity (SRS) of the as-cast alloy, m= $\frac{\partial\, ln\sigma}{\partial\, In\dot{\varepsilon}}$, at a strain of 0.02 was calculated as 0.035 considering two strain rates, 0.0001s^{-1} and 2350s^{-1}, across quasi-static and dynamic loading conditions. Similarly, the strain rate sensitivity in the quasi-static range (m_s) was 0.033 and in the dynamic loading (m_d) was 0.275. The SRS(m) of the as-cast alloy was higher than conventional FCC metals like Al, Ni, Cu, 304 L *etc.*[17,23] . The SRS(m) reported by Li *et al.* in single-phase FCC-based HEA $Al_{0.3}CoCrFeNi$ was 0.053 [26]. The SRS for single-phase FCC-based HEA $Al_{0.1}CoCrFeNi$ was 0.033 and 0.009 in the as-cast and the cold-rolled conditions of the alloy, respectively, as per the findings of Gangireddy *et al.* [19,25]. The SRS for the Co-free FCC-BCC based dual-phase $AlCrCuFeNi_2$ was estimated as 0.0124 [29]. For dual-phase alloy $Al_{0.6}CoCrFeMnNi$ having FCC and BCC phases, having a similar dendritic microstructure as the alloy under the current study, the SRS was evaluated as 0.029 [9]. A hypo-eutectic alloy $Al_{0.7}CoCrFeNi$ having FCC and BCC phases with lamellar microstructure exhibited an SRS of 0.018 [30]. Therefore, the overall SRS, i.e., calculated across quasi-static and dynamic loading conditions, of the as-cast alloy investigated in the current research work was the highest among all previously-studied dual-phase FCC-BCC alloys of AlCoCrFeNi system. The dynamic SRS (m_d) of the alloy under investigation proved to be higher than most of the FCC-based HEAs studied under high strain rate loading conditions [25,31,32].

In general, the strain rate sensitivity depends on the relative contributions of temperature-dependent strengthening factors that influence slip and dislocation activities. The microstructure of a material largely influences the dislocation motion and the SRS of the material. However, the dislocation hindrances are caused by both long-range athermal obstacles and short-range thermal obstacles. The relative dominance of the above two types of obstacles eventually impacts the value of SRS. The mechanical threshold stress (MTS) model formulates the total stress (σ) required for deformation as [19,33]:

$$\sigma = \sigma_{thermal} + \sigma_{athermal} \qquad 4.6$$

The thermal contributions of stress are from the frictional stress σ_{fs}, Peierls Nabarro (σ_{P-N}) stress and the solid solution strengthening (σ_{ss}). The higher values of these stress contributors increase the SRS values of an alloy system. The athermal barriers in the form of grain boundaries (σ_{GB}), dislocation density (σ_{DIS}) and twin boundaries (σ_{TW}) adversely impact the SRS of a material. The solid solution strengthening was one of the dominant strengthening mechanisms in the as-cast alloy as reported in a previous work published by the authors [7]. In addition, the large grain size of the as-cast alloy, which led to lower number of long-range athermal obstacles in the form of grain boundaries, resulted in excellent strain rate sensitivity. However, the SRS of the alloy was less than single-phase FCC based alloy $Al_{0.3}CoCrFeNi$ due to the presence of BCC/B2 spinodally-decomposed interdendritic region that created reasonable number of long-range interphase boundaries [33].

The Kocks-Mecking (K-M) plot of strain hardening rate ($\theta = \frac{d\sigma}{d\epsilon}$) vs flow stress ($\sigma - \sigma_y$) is presented in Fig. .3(c). The plot consists of three stages of strain hardening rate in all the cases of loading. Stage A is a rapidly decreasing strain hardening rate with stress, which is a transition region from elastic to plastic, stage B is the gradually decreasing strain hardening rate with stress, which is usually governed by dislocation slip, and finally stage C is the region of constant strain hardening rate with stress resulting from dynamic recovery. The dynamic strain hardening rate in stage A ended at higher values, $\theta = 4621$ MPa for strain rate of 2350 s^{-1}, than the quasi-static condition, $\theta = 2694$ MPa for strain rate of 10^{-4} s^{-1}, because of the phonon drag which became activated at high strain rates as mentioned in Eq. 7 and Eq. 8. In addition, the various substructure formation associated with dynamic loading could be the reasons for higher strain hardening rate compared to quasi-static loading [24,34]. However, slip was the dominant deformation mechanism in both quasi-static and dynamic compression tests. To further investigate the appropriate reasons, the post-deformation microstructures are analysed in the next section.

The flow stress as a function of temperature under dynamic loading was studied by varying the temperature from room temperature to 473 K at a strain rate of ~1800 s^{-1} (Fig 4.4 (a)). The flow stresses corresponding to a strain $\varepsilon = 0.02$ with varying temperatures were considered to evaluate the thermal softening effects through the temperature sensitivity parameter ($\eta_a = \left|\frac{\sigma_2-\sigma_1}{T_2-T_1}\right|$) (Table. 4.1).

Table 4.1 Temperature sensitivity parameter for the alloy at high strain rate

Strain rate (s^{-1})	Temperature (K)	Temperature sensitivity η_a (MPa/K)
~1800	$T_1 = 298$, $T_2 = 373$	1.04
	$T_1 = 373$, $T_2 = 423$	0.925
	$T_1 = 423$, $T_2 = 473$	0.635

The flow stress of the alloy decreased monotonically with temperature at strain rate ~1800 s^{-1} as shown in Fig 4.4(b) due to thermal softening effects. Table 4.1 clearly shows that the thermal sensitivity parameter decreases with an increase in temperature. This is because the dominance of phonon drag, which becomes activated at high strain rate, increases as the temperature increases for the range of temperature studied [20,35–37].

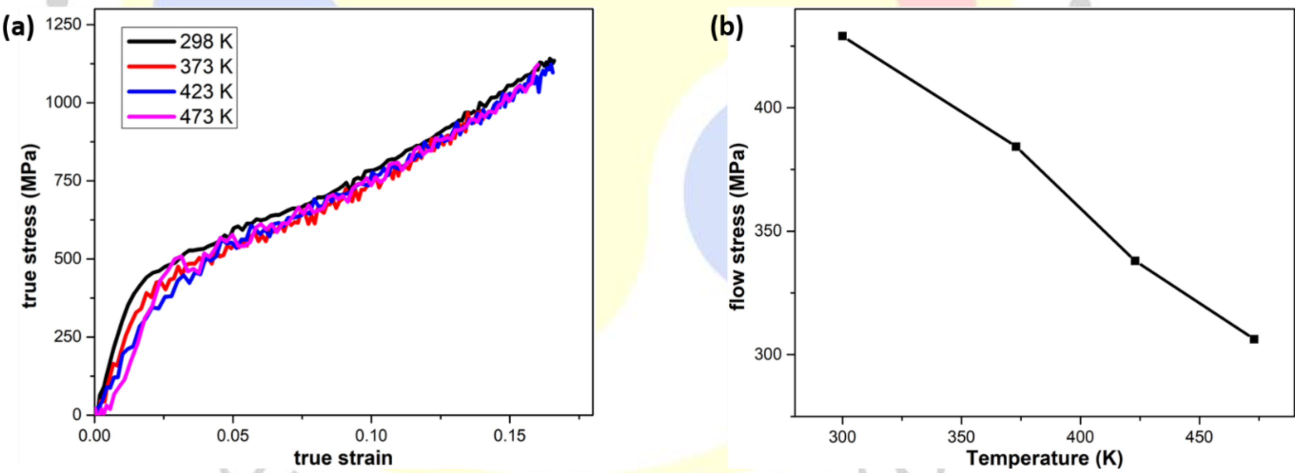

Figure 4.4 (a) Stress-strain curve at a strain rate of 1800 s^{-1} with varying temperature range, and (b) temperature vs flow stress at a strain $\varepsilon = 0.02$ and a strain rate of 1800 s^{-1}.

Therefore, the current as-cast alloy has shown excellent resistance to thermal softening under high strain rate loading. The serration behaviour at large strains indicated the continuous competition of strain hardening behaviour and thermal softening effect delaying the adiabatic shear localization, which is a major failure mechanism under high strain rate deformation. The other possible causes of serration can be due complex wave interactions while carrying out test in split Hopkinson bar or due to the inherent tendency of high entropy alloys towards compositional fluctuations at such high strain rate of deformation [14,15,38,39].

4.3.3 Constitutive Model

The visco-plasticity of metallic materials involves the competition between strain hardening and thermal softening. The strain hardening effect increases the flow stress while the thermal softening decreases it. The thermal softening effect becomes significant when the rate of heat generation during plastic deformation is greater than the rate of heat dissipation. Due to rapid deformation process under high strain rate loading, the generated heat during deformation does not get enough time to dissipate. The fraction of plastic work converted into heat contributes to the adiabatic temperature rise, which can be expressed by the following equation [9,25,26]:

$$\Delta T = T - T_0 = \frac{\beta}{\rho C_p}\int_0^{\varepsilon_p} \sigma \, d\varepsilon \qquad 4.7$$

where ΔT is the rise in the temperature, T is the instantaneous temperature, and T_0 is the initial temperature (T_0 in this case is 298K). In addition, ρ (7.79 g/cm^3) and C_p(479.79J/kg K) are the density and the heat capacity of the alloy, respectively, and they were evaluated by the rule of mixture [40]. The fraction of plastic energy converted into heat (β) is usually taken as 0.9. The rise in temperature with true strain is shown in Fig 4.5(a).

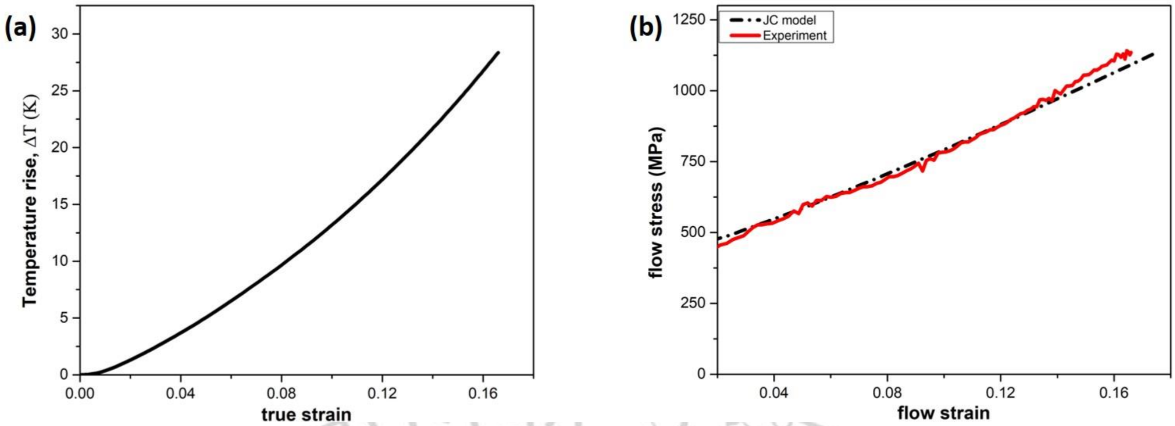

Figure 4.5 (a) high strain rate deformation induced temperature rise as a function of plastic strain at strain rate of 1800 s^{-1}- (b) JC model prediction of experimental results with reference strain rate of 1300 s^{-1}

The rise in temperature (ΔT), which is evaluated using Eq. 4.7, increased with oncreasing strain rate Table 4.2.

Table 4.2 Rise in temperature with plastic strain at each strain rates

Strain rate (s^{-1})	Rise in temperature ΔT (K)	Instantaneous temperature T (K)
1300	23.22	323.22
1800	28.35	328.35
2350	34.23	334.23

Johnson Cook (J-C) model is one of the most widely used constitutive models of predicting plasticity of metals and alloys under high strain rate loading. The J-C model expresses the flow stress (σ) as a function of strain (ε), strain rate ($\dot{\varepsilon}$) and temperature (T). The following empirical J-C model equation is adopted [9]:

$$\sigma = (A + B\varepsilon^n)(1 + C\ln\frac{\dot{\varepsilon}}{\dot{\varepsilon}_0})(\frac{T_m - T}{T_m - T_r})^\gamma \qquad 4.8$$

where A, B, C and n are experimental parameters and γ is the thermal softening parameter. The ambient or initial temperature ($T_0 = 298$ K), is taken as the reference temperature(T_r).

The reference strain rate $\dot{\varepsilon}_0$ is taken as 1300s^{-1} and T is the instantaneous temperature during dynamic deformation, which is obtained using Eq.4.7 and listed in Table 4.2. The melting temperature T_m was calculated to be 1353°C from the rule of mixture [40]. The modified J-C cook equation after substituting experimental data for the range of strain rate is shown below:

$$\sigma_f = (400 + 5253\varepsilon^{0.53})(1 + 0.11 \ln \frac{\dot{\varepsilon}}{\dot{\varepsilon}_0})(\frac{T_m - T}{T_m - T_r})^{-0.45} \quad 4.9$$

The flow stress-strain curve using Eq.4.9 for dynamic deformation at strain rate of 1800 s^{-1} is plotted along with the experimental data in Fig. 4.5(b). Thus, the modified J-C equation is in good agreement with the experimental results.

4.3.4 Deformation Mechanisms

Fig. 4.6 represents the inverse pole figure (IPF), the phase map, the geometrically necessary dislocations (GND) map and the band contrast map combined with boundary maps along with misorientation plots of a section parallel to the loading direction of the deformed as-cast alloy sample compressed at a strain rate of ~1800 s^{-1}. These maps show the dislocation distributions and various substructure formations to understand the strain hardening behavior and deformation mechanisms involved at high strain rate loading. In our previous study of the as-cast alloy, the deformation behavior under quasi-static loading resulted in the formation of high misorientation based wavy deformation bands in the FCC region [7]. In contrast, the alloy exhibited a range of deformation substructure formations at high strain rate loading as shown in Fig. 4.6. Additionally, TEM image shown in Fig. 4.7 were analyzed to find the possibility of formation of nano-level deformation substructures and associated deformation mechanisms involved at room temperature and at high temperature under high strain rate loading. The major deformation mechanisms in the as-cast alloy are illustrated below.

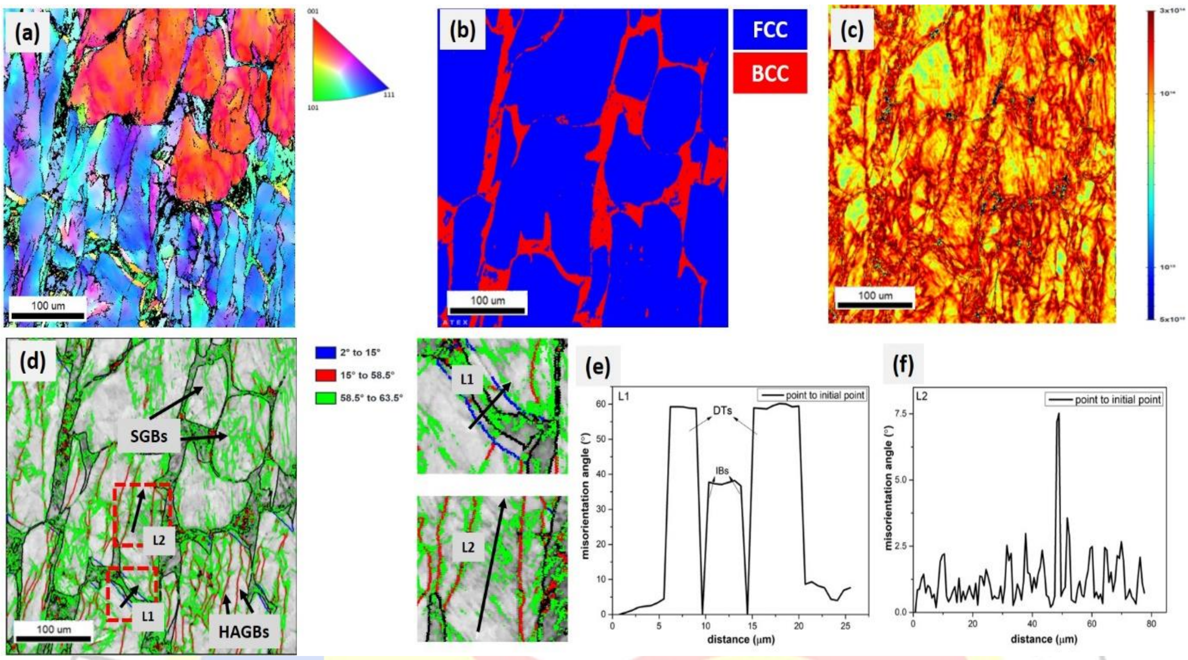

Figure 4.6 EBSD images of deformed as-cast alloy at a nominal strain of ~16% compressed at a strain rate of 1800 s^{-1}: (a)IPF, (b) phase map, (c) GND map showing areas of high dislocation densities, (d) misorientation boundary overlaid on band contrast map along with their magnified images showing the regions of deformation twins (DTs, marked by blue color), sub grain boundaries (SGBs, marked by green color), high angle grain boundaries (HAGBs, marked by red color), interphase boundaries (IBs, marked by black color) and deformation bands (DBs), and (e,f) misorientation plots (point to initial point) across DTs, IBs and DBs.

Dislocation strengthening

The average density of GNDs (ρ_{GND}) after dynamic deformation was close to 1.3 × 10^{14} m^{-2} with high concentration of dislocations (ρ_{GND}=3.3 × 10^{14} m^{-2}) along the interphase boundaries (Fig. 4.6(c)). Parallel deformation bands were formed with maximum misorientation angle of 7.5° within the FCC region of the grains (Fig. 4.6(d) and (f)). Subgrain boundaries (SGBs) having misorientations between 2° and 10° marked by green colour in Fig. 4.6(d)) were one of the important substructures noticed in the deformed alloy samples under high strain rate loading. The GND densities at the SGBs and DBs (ρ_{GND} = 7.5 × 10^{13} m^{-2}) were almost four times lower compared to the interphase boundaries. High concentration of dislocations at interphase boundaries and formation of DBs and SGBs help in excellent strain hardening rate in the stage B of deformation as was shown in K-M plots of Fig. 4.3(c).

These substructures act as barriers to dislocation glide and also act as active sites for stacking fault interactions due to severe lattice distortion. The gradual conversion of SGBs to HAGBs (misorientations >10°) due to large lattice rotation can be confirmed from Fig. 4.6(d) in which HAGBs were formed encompassing the SGBs [41]. These zones of HAGBs exhibited very high dislocation accumulation having ρ_{GND} =1.7 × 10^{14} m^{-2}. This occurs in HEAs because the low SFE restricts for dislocation cross slip which makes the requirement of partial dislocations to unify into dislocations. This creates higher pinning effect among dislocations at different slip planes and forces dislocations towards planar slip. The planar slip generates lattice misfit that results in higher GNDs to accommodate for the misorientation creating high dislocation pile ups and DBs [42].

Twin strengthening

Another major energy storage deformation substructure in the as-cast alloy under dynamic loading was the deformation twins (DTs) with CSL $\sum 3 = 60°$ misorientation near the BCC-FCC interphase boundaries (IBs) as shown in Fig. 4.6(d) and (e). As mentioned above, the interphase boundaries also act as zones of high dislocation density making them high energy sites for probable twin formation. Therefore, a mixed mode of deformation mechanism, i.e., dislocation slip and deformation twinning, was observed in the as-cast alloy under dynamic loading. The critical stress for twin formation (σ_T) can be expressed by the following equation [9]:

$$\sigma_T = \frac{2\gamma_{SF}}{mb_p} \qquad 4.10$$

where γ_{SF} is the stacking fault energy (SFE), m is the average Schmid factor and b_p is the Burgers vector. Although the stacking fault energy of the dual-phase as-cast alloy can be close to 150 mJ/m^2 as reported for $Al_{0.6}CoCrFeNi$, the FCC region due to low presence of Al were estimated around 36 mJ/m^2, which makes them conducive for twin formation as per Eq. 4.10 [9]. The formation of additional twin boundary induce back stress which hinder the mean free path of the dislocation and increase strain storage capacity by creating heavy dislocation pile-ups with ρ_{GND} values similar to interphase boundaries [10]. Therefore, deformation twinning enhanced the strain hardening behaviour of the as-cast alloy.

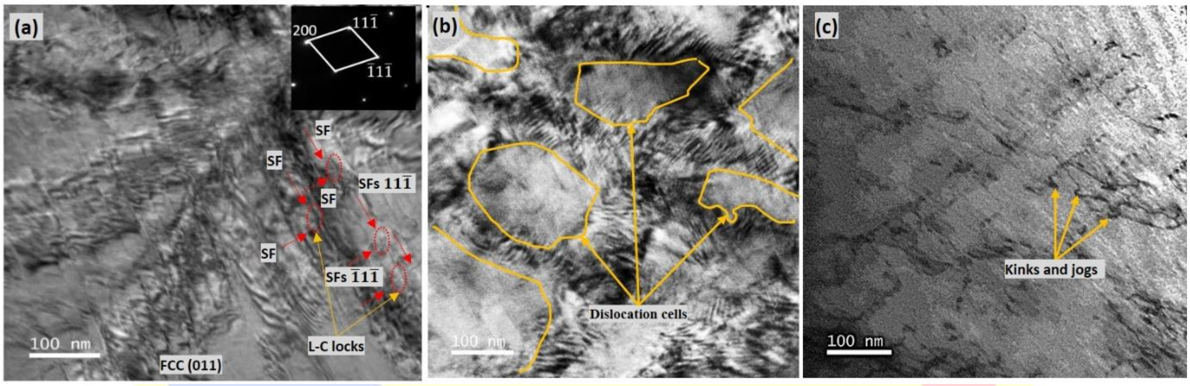

Figure 4.7 Bright-field (BF) TEM images of the alloy sample at a nominal strain of ~16% deformed at a strain rate of 1800 s^{-1} showing (a) SF-SF interactions in the form of Lomer-Cottrell (L-C) locks at room temperature, (b) formation of dislocation cells at 200 °C and (c) dislocation patterns in the form of jogs and kinks at 200 °C.

Stacking-fault (SFs) strengthening

The bright-field (BF) images at room temperature deformation in Fig. 7(a) showed that the as-cast alloy developed a high density of stacking faults (SFs) in the FCC dendritic region pertaining to its low stacking fault energy as mentioned previously. The evidence of stacking faults in the form of Shockley partial dislocations on the planes $(11\bar{1})$ and $(\bar{1}1\bar{1})$ can be observed in the bright-field image and its corresponding SAED pattern in Fig. 4.7(a). The SF-SF interactions resulted in the formation of V-shaped Lomer-Cottrell (L-C) locks (Fig. 4.7(a)). The resultant of the interaction between two partial dislocations, which result in formation of sessile stair rod dislocation from two SFs of {111} planes, is $\frac{1}{6}[1\bar{1}0]$ [17,23,43,44]. The L-C locks, which act as precursor to deformation twin, contributed to the excellent strain hardening properties of the alloy. In contrast, there was no sign of formation such Shockley partials for the as-cast alloy samples deformed under high strain rate at 200 °C (Fig. 4.7(b) and (c)) due to the rise in the stacking fault energy with temperature[43,44]. However, intense dislocation cell formation (Fig. 4.7(b)) and dislocation interactions in the form of jogs and kinks (Fig. 4.7(c)) helped to retain good strain hardening properties at high temperature under high strain rate loading.

Thus, the overall deformation mechanisms in the as-cast alloy under dynamic loading was driven by dislocation pile-ups near interphase boundaries (IBs) and the formation of subgrain boundaries (SGBs), deformation twins (DTs) and deformation bands (DBs). The presence of L-C locks at room temperature also established SF-SF interactions during high strain rate deformation. The plasticity behaviour of the alloy at high temperature under high strain rate loading was characterized by the formation of dislocation cells, kinks and jogs.

4.4 Summary

The as-cast alloy $Al_{0.65}CoCrFe_2Ni$ prepared under industrially melted large-scale comprised of both FCC phase as dendritic region and BCC/B2 phase in the interdendritic spinodally decomposed region, respectively, with grain sizes of the order of 10^3 μm. The high strain rate loading response and associated deformation mechanisms of the as-cast alloy can be summarized as follows.

(a) The dual-phase as-cast alloy exhibited high strain rate sensitivity (SRS) having comparable values to that of single-phase FCC-based HEAs owing to its dominant solid solution strengthening and low athermal strengthening contributions.

(b) The temperature sensitivity or the thermal softening effect decreased with the increase in operating temperature under high strain rate loading due to rise in phonon drag effects with temperature.

(c) The deformation of the as-cast alloy under dynamic loading at room temperature was governed by interphase boundary strengthening and the formation of deformation twins, sub-grain boundaries, deformation bands and L-C locks.

(d) The deformation under high strain rate loading at high temperature exhibited excellent retention of strain hardening behaviour due to the formation of dislocation cells, jogs and kinks.

(e) The JC model predicted the plasticity behaviour of the as-cast alloy under high strain rate loading with reasonable accuracy.

The outstanding strain rate sensitivity of the as-cast dual-phase high entropy alloy along with its excellent strain hardening behaviour under high strain rate loading for a range of temperature lays the foundation for the alloy to be used in applications such as impact-resistant structures and high-speed manufacturing processes. The effect of cooling rate of solidification under dynamic loading on various aspects will establish the amount of strain hardening and strain rate sensitivity that can be adjusted further to achieve the desired results.

References

[1] C.Y. Hsu, T.S. Sheu, J.W. Yeh, S.K. Chen, Effect of iron content on wear behavior of AlCoCrFexMo0.5Ni high-entropy alloys, Wear. (2010). https://doi.org/10.1016/j.wear.2009.10.013.

[2] X. Yang, Y. Zhang, Prediction of high-entropy stabilized solid-solution in multi-component alloys, Mater. Chem. Phys. 132 (2012) 233–238. https://doi.org/10.1016/j.matchemphys.2011.11.021.

[3] S. Guo, C.T. Liu, Phase stability in high entropy alloys: Formation of solid-solution phase or amorphous phase, Prog. Nat. Sci. Mater. Int. (2011). https://doi.org/10.1016/S1002-0071(12)60080-X.

[4] J.W. Yeh, Alloy design strategies and future trends in high-entropy alloys, JOM. 65 (2013) 1759–1771. https://doi.org/10.1007/s11837-013-0761-6.

[5] K.Y. Tsai, M.H. Tsai, J.W. Yeh, Sluggish diffusion in Co-Cr-Fe-Mn-Ni high-entropy alloys, Acta Mater. (2013). https://doi.org/10.1016/j.actamat.2013.04.058.

[6] Y.F. Ye, Q. Wang, J. Lu, C.T. Liu, Y. Yang, High-entropy alloy: challenges and prospects, Mater. Today. (2016). https://doi.org/10.1016/j.mattod.2015.11.026.

[7] S. Tamuly, S. Dixit, B. Kombaiah, P. Khanikar, Strengthening Mechanisms and Deformation Behavior of Industrially-Cast and Lab-Cast Dual-Phase High Entropy Alloy, Met. Mater. Int. (2022). https://doi.org/10.1007/s12540-022-01211-x.

[8] Website, www.atex-software.eu, (n.d.). http://www.atex-software.eu/ (accessed December 25, 2021).

[9] L. Wang, J.W. Qiao, S.G. Ma, Z.M. Jiao, T.W. Zhang, G. Chen, D. Zhao, Y. Zhang, Z.H. Wang, Mechanical response and deformation behavior of Al0.6CoCrFeNi high-entropy alloys upon dynamic loading, Mater. Sci. Eng. A. 727 (2018) 208–213. https://doi.org/10.1016/j.msea.2018.05.001.

[10] I. Basu, V. Ocelík, J.T.M. De Hosson, BCC-FCC interfacial effects on plasticity and strengthening mechanisms in high entropy alloys, Acta Mater. 157 (2018) 83–95. https://doi.org/10.1016/j.actamat.2018.07.031.

[11] R.S. Ganji, P. Sai Karthik, K. Bhanu Sankara Rao, K. V. Rajulapati, Strengthening mechanisms in equiatomic ultrafine grained AlCoCrCuFeNi high-entropy alloy studied by micro- and nanoindentation methods, Acta Mater. 125 (2017) 58–68. https://doi.org/10.1016/j.actamat.2016.11.046.

[12] C.T. Wang, Y. He, Z. Guo, X. Huang, Y. Chen, H. Zhang, Y. He, Strain Rate Effects on the Mechanical Properties of an AlCoCrFeNi High-Entropy Alloy, Met. Mater. Int. 27 (2021) 2310–2318. https://doi.org/10.1007/s12540-020-00920-5.

[13] A. Arab, Y. Guo, Z. Dilshad Ibrahim Sktani, P. Chen, Effect of strain rate and temperature on deformation and recrystallization behaviour of BCC structure AlCoCrFeNi high entropy alloy, Intermetallics. 147 (2022) 107601. https://doi.org/10.1016/j.intermet.2022.107601.

[14] M.N. Hasan, J. Gu, S. Jiang, H.J. Wang, M. Cabral, S. Ni, X.H. An, M. Song, L.M. Shen, X.Z. Liao, Effects of elemental segregation on microstructural evolution and local mechanical properties in a dynamically deformed CrMnFeCoNi high entropy alloy, Scr. Mater. 190 (2021) 80–85. https://doi.org/10.1016/j.scriptamat.2020.08.048.

[15] S. Chen, W. Li, F. Meng, Y. Tong, H. Zhang, K.K. Tseng, J.W. Yeh, Y. Ren, F. Xu, Z. Wu, P.K. Liaw, On temperature and strain-rate dependence of flow serration in HfNbTaTiZr high-entropy alloy, Scr. Mater. 200 (2021) 113919. https://doi.org/10.1016/j.scriptamat.2021.113919.

[16] S. Niu, H. Kou, Y. Zhang, J. Wang, J. Li, The characteristics of serration in Al0.5CoCrFeNi high entropy alloy, Mater. Sci. Eng. A. 702 (2017) 96–103. https://doi.org/10.1016/j.msea.2017.05.075.

[17] W. Jiang, X. Gao, Y. Guo, X. Chen, Y. Zhao, Dynamic impact behavior and deformation mechanisms of Cr26Mn20Fe20Co20Ni14 high-entropy alloy, Mater. Sci. Eng. A. 824 (2021) 141858. https://doi.org/10.1016/j.msea.2021.141858.

[18] L. Wang, J.W. Qiao, S.G. Ma, Z.M. Jiao, T.W. Zhang, G. Chen, D. Zhao, Y. Zhang, Z.H. Wang,

Mechanical response and deformation behavior of Al0.6CoCrFeNi high-entropy alloys upon dynamic loading, Mater. Sci. Eng. A. (2018). https://doi.org/10.1016/j.msea.2018.05.001.

[19] S. Gangireddy, L. Kaimiao, B. Gwalani, R. Mishra, Microstructural dependence of strain rate sensitivity in thermomechanically processed Al0.1CoCrFeNi high entropy alloy, Mater. Sci. Eng. A. 727 (2018) 148–159. https://doi.org/10.1016/j.msea.2018.04.108.

[20] M. lei Hu, W. dong Song, D. bo Duan, Y. Wu, Dynamic behavior and microstructure characterization of TaNbHfZrTi high-entropy alloy at a wide range of strain rates and temperatures, Int. J. Mech. Sci. 182 (2020) 105738. https://doi.org/10.1016/j.ijmecsci.2020.105738.

[21] M.R. Chen, S.J. Lin, J.W. Yeh, S.K. Chen, Y.S. Huang, C.P. Tu, Microstructure and properties of Al0.5CoCrCuFeNiTix (x = 0-2.0) high-entropy alloys, in: Mater. Trans., 2006: p. Vol.47 No. 5 1396-1401. https://doi.org/10.2320/matertrans.47.1395.

[22] Y.M. Wang, A. V. Hamza, E. Ma, Temperature-dependent strain rate sensitivity and activation volume of nanocrystalline Ni, Acta Mater. 54 (2006) 2715–2726. https://doi.org/10.1016/j.actamat.2006.02.013.

[23] X. Zhong, Q. Zhang, M. Ma, J. Xie, M. Wu, S. Ren, Y. Yan, Dynamic compressive properties and microstructural evolution of Al1.19Co2CrFeNi1.81 eutectic high entropy alloy at room and cryogenic temperatures, Mater. Des. 219 (2022) 110724. https://doi.org/10.1016/j.matdes.2022.110724.

[24] J.M. Park, J. Moon, J.W. Bae, M.J. Jang, J. Park, S. Lee, H.S. Kim, Strain rate effects of dynamic compressive deformation on mechanical properties and microstructure of CoCrFeMnNi high-entropy alloy, Mater. Sci. Eng. A. 719 (2018) 155–163. https://doi.org/10.1016/j.msea.2018.02.031.

[25] N. Kumar, Q. Ying, X. Nie, R.S. Mishra, Z. Tang, P.K. Liaw, R.E. Brennan, K.J. Doherty, K.C. Cho, High strain-rate compressive deformation behavior of the Al0.1CrFeCoNi high entropy alloy, Mater. Des. 86 (2015) 598–602. https://doi.org/10.1016/j.matdes.2015.07.161.

[26] Z. Li, S. Zhao, H. Diao, P.K. Liaw, M.A. Meyers, High-velocity deformation of Al0.3 CoCrFeNi high-entropy alloy: Remarkable resistance to shear failure, Sci. Rep. 7 (2017) 1–8. https://doi.org/10.1038/srep42742.

[27] S. Jiang, Z. Lin, H. Xu, Y. Sun, Studies on the microstructure and properties of Al x CoCrFeNiTi 1-x high entropy alloys, J. Alloys Compd. (2018). https://doi.org/10.1016/j.jallcom.2018.01.247.

[28] I. Basu, J.T.M. De Hosson, Strengthening mechanisms in high entropy alloys: Fundamental issues, Scr. Mater. 187 (2020) 148–156. https://doi.org/10.1016/j.scriptamat.2020.06.019.

[29] S.G. Ma, Z.M. Jiao, J.W. Qiao, H.J. Yang, Y. Zhang, Z.H. Wang, Strain rate effects on the dynamic mechanical properties of the AlCrCuFeNi2 high-entropy alloy, Mater. Sci. Eng. A. 649 (2016) 35–38. https://doi.org/10.1016/j.msea.2015.09.089.

[30] S. Gangireddy, B. Gwalani, R. Banerjee, R.S. Mishra, High Strain Rate Response of Al0.7CoCrFeNi High Entropy Alloy: Dynamic Strength Over 2 GPa from Thermomechanical Processing and Hierarchical Microstructure, J. Dyn. Behav. Mater. 5 (2019) 1–7. https://doi.org/10.1007/s40870-018-00178-4.

[31] X. Liu, Y. Wu, Y. Wang, J. Chen, R. Bai, L. Gao, Z. Xu, W.Y. Wang, C. Tan, X. Hui, Enhanced dynamic deformability and strengthening effect via twinning and microbanding in high density NiCoFeCrMoW high-entropy alloys, J. Mater. Sci. Technol. 127 (2022) 164–176. https://doi.org/10.1016/j.jmst.2022.02.055.

[32] H. Li, C. Shao, O.K. Orhan, D.F. Rojas, M. Ponga, J.D. Hogan, Strain-Rate-Dependent mechanical behavior of a non-Equimolar CoCrFeMnNi high entropy alloy with a segmented coarse grain structure, Materialia. 21 (2022) 101271. https://doi.org/10.1016/j.mtla.2021.101271.

[33] S. Gangireddy, B. Gwalani, K. Liu, R. Banerjee, R.S. Mishra, Microstructures with extraordinary dynamic work hardening and strain rate sensitivity in Al0.3CoCrFeNi high entropy alloy, Mater. Sci. Eng. A. 734 (2018) 42–50. https://doi.org/10.1016/j.msea.2018.07.088.

[34] M. Zhang, L. Zhang, J. Fan, G. Li, P.K. Liaw, R. Liu, Microstructure and enhanced mechanical

behavior of the Al 7 Co 24 Cr 21 Fe 24 Ni 24 high-entropy alloy system by tuning the Cr content, Mater. Sci. Eng. A. (2018). https://doi.org/10.1016/j.msea.2018.07.069.

[35] S. Yao, X. Pei, Z. Liu, J. Yu, Y. Yu, Q. Wu, Numerical investigation of the temperature dependence of dynamic yield stress of typical BCC metals under shock loading with a dislocation-based constitutive model, Mech. Mater. 140 (2020) 103211. https://doi.org/10.1016/j.mechmat.2019.103211.

[36] G. Regazzoni, U.F. Kocks, P.S. Follansbee, Dislocation kinetics at high strain rates, Acta Metall. 35 (1987) 2865–2875. https://doi.org/10.1016/0001-6160(87)90285-9.

[37] Y. Zhang, Q. Shen, X. Chen, S. Jayalakshmi, R.A. Singh, S. Konovalov, V.B. Deev, E.S. Prusov, Strengthening mechanisms in cocrfenix0.4 (al, nb, ta) high entropy alloys fabricated by powder plasma arc additive manufacturing, Nanomaterials. 11 (2021) 1–14. https://doi.org/10.3390/nano11030721.

[38] Z. Xie, W.R. Jian, S. Xu, I.J. Beyerlein, X. Zhang, Z. Wang, X. Yao, Role of local chemical fluctuations in the shock dynamics of medium entropy alloy CoCrNi, Acta Mater. 221 (2021) 117380. https://doi.org/10.1016/j.actamat.2021.117380.

[39] K.A. Dahmen, P.K. Liaw, SERRATION BEHAVIOR OF HIGH-ENTROPY ALLOYS (HEAs), (2016) 65. https://www.netl.doe.gov/%5Cnhttps://drive.google.com/open?id=0B0fTxDBXtHZMRHVKd1RfX2xnMmM.

[40] R. Sriharitha, B.S. Murty, R.S. Kottada, Alloying, thermal stability and strengthening in spark plasma sintered AlxCoCrCuFeNi high entropy alloys, J. Alloys Compd. 583 (2014) 419–426. https://doi.org/10.1016/j.jallcom.2013.08.176.

[41] P. Lehto, Adaptive domain misorientation approach for the EBSD measurement of deformation induced dislocation sub-structures, Ultramicroscopy. 222 (2021) 113203. https://doi.org/10.1016/j.ultramic.2021.113203.

[42] N. Li, W. Chen, J. He, J. Gu, Z. Wang, Y. Li, M. Song, Dynamic deformation behavior and microstructure evolution of CoCrNiMox medium entropy alloys, Mater. Sci. Eng. A. 827 (2021). https://doi.org/10.1016/j.msea.2021.142048.

[43] H. Huang, J. Wang, H. Yang, S. Ji, H. Yu, Z. Liu, Strengthening CoCrNi medium-entropy alloy by tuning lattice defects, Scr. Mater. 188 (2020) 216–221. https://doi.org/10.1016/j.scriptamat.2020.07.027.

[44] X.D. Xu, P. Liu, Z. Tang, A. Hirata, S.X. Song, T.G. Nieh, P.K. Liaw, C.T. Liu, M.W. Chen, Transmission electron microscopy characterization of dislocation structure in a face-centered cubic high-entropy alloy Al0.1CoCrFeNi, Acta Mater. 144 (2018) 107–115. https://doi.org/10.1016/j.actamat.2017.10.050.

Chapter 5 High Strain Rate Deformation of Rapidly Cooled Suction-Cast Dual-Phase High Entropy Alloy

5.1 Introduction

In this chapter, the suction-cast rapidly cooled $Al_{0.65}CoCrFe_2Ni$ having FCC and BCC phases were deformed under high strain rate loading conditions. The effect of higher cooling rate of solidification on the microstructure and subsequent strain rate hardening, strain rate sensitivity and strain hardening behaviour at high strain rate loading were compared with their quasi static loading behaviour and the as-cast industrially melted alloy conditions. The strain rate sensitivity decreased with increase in cooling rate due to decrease in the grain size and high dislocation hardening in the suction cast alloy compared to the as-cast alloy. The strain hardening rate under high strain rate was higher than its quasi static conditions due activation of phonon drag effect. The strain hardening rate of the suction-cast compared to the as-cast alloy conditions were also higher than as-cast conditions. The orientation image mapping images were analysed to understand the deformation behaviour at high strain rate and compared to deformation at quasi static conditions at similar nominal strain. It was observed that high strain rate loadings of the suction cast alloy lead to homogeneous deformation without large strain gradients in the FCC matrix interior and its boundary areas while the deformation under quasi static deformation lead to inhomogeneous deformation in the FCC phase of the alloy. The high strain rate loading of the suction cast alloy also exhibited excellent strain hardening features like deformation bands and deformation twins during the course of deformation thereby establishing an overall improvement in the properties compared to the large scale as-cast conditions.

5.2 Materials And Methodology

As mentioned in the previous chapters, the high entropy alloy $Al_{0.65}CoCrFe_2Ni$ was designed to have both FCC and BCC phases maintaining a high Fe content. The enthalpy of mixing (ΔH_{mix}), configurational entropy (ΔS) and size effect (δ) of the alloy were calculated as $-12.264\ KJ/mol$, 1.535 R (gas constant) and 4.67%, respectively. The overall combined effect (Ω) of entropy, enthalpy and size effect was calculated to be greater than 1.1. The design considerations were made in such a way that all the above theoretical values adhered to the definition of high entropy alloy.[1–3]. The valence electron concentration (VEC) criteria of 6.4<VEC<8.5 required for dual FCC-BCC phase HEAs was also maintained (VEC=7.626) to obtain both FCC and BCC phases in the alloy[4,5] . The as-cast (IM) alloy $Al_{0.65}CoCrFe_2Ni$ was prepared in an large-scale vacuum induction melting setup at Mishra Dhatu Nigam Limited, (MIDHANI) Hyderabad. The furnace consisted of a 60kg crucible having alumina lining. The melting was performed in an argon atmosphere of 10^{-2} mbar for half an hour. Electromagnetic stirring was used to maintain the homogeneity of the melt pool. After the complete meltdown and stirring, the liquid melt was poured in a rectangular shaped mould located inside the argon chamber. An appropriate riser was designed and attached on the top of the mould of the cast to ensure defect-free condition. The cast was placed in the furnace chamber under argon atmosphere for a few hours to complete solidification. The cooling rate of solidification during this processing was ~10 K/s. The slow cooling of solidification ensured low residual thermal stress as reported in a previous work published by the authors[6]. This industrially melted as-cast alloy was re-melted by vacuum arc melting taking 50 g each at time and suction cast into a copper mould in cylindrical shapes of 6 mm diameter and 80 mm length. The suction-cast alloy (SC) was cooled at a very high rate of the order of ~10^3 K/s. Microstructural evaluation and phase identification for the alloy were exercised using X-ray diffraction (XRD) and scanning electron microscopy (SEM) techniques. The XRD analysis have been performed with Cu-k$_{\alpha}$ radiation (λ=1.5406 Å) operating at 50kV/160mA in a Rigaku made instrument. Field emission scanning electron microscope (FE-SEM) make Zeiss model Sigma integrated with energy dispersive spectroscopy (EDS) detectors make Oxford have been used to examine the microstructure as well as elemental mapping at different locations. Oxford Instruments made electron backscatter diffraction (EBSD) probe integrated with FE-SEM were used to identify the phases and grains and substructures in the alloy before and after deformation under dynamic loading. The orientation image maps have been generated using TSL-OIM software and ATEX software [7].

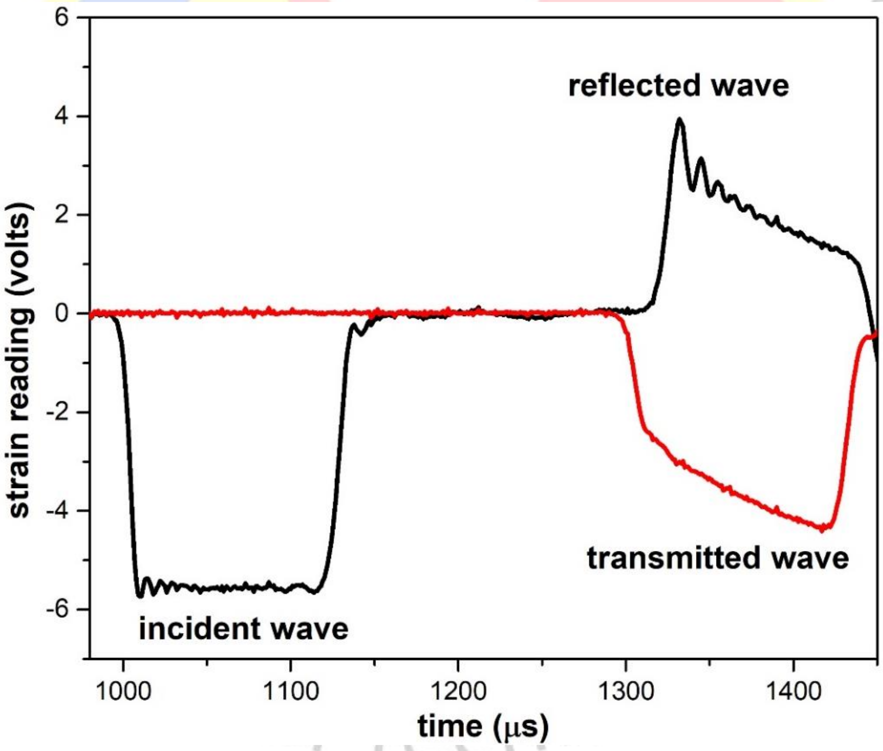

Figure 5.1 Typical wave forms of incident, transmitted and reflected signals obtained during the test.

Cylindrical samples of the alloy having dimensions of 6 mm diameter and 6 mm height was compressed under quasi-static conditions at strain rates ~ 10^{-4} s^{-1} and 10^{-2} s^{-1} at room temperature using Instron 8801 universal testing machine. The high strain rate deformation behaviour was tested using a split Hopkinson pressure bar (SHPB) setup at Indian Institute of

Technology Kanpur. The dimensions of the cylindrical samples were 6 mm diameter and 5 mm height. The strain gauges were mounted in a diametrically opposite arrangement on the incident bar and the transmission bar. The wave form recorded in the oscilloscope generated by an impact on the SC alloy sample at a strain rate 2100 s^{-1} is displayed in Fig 1. The engineering stress (σ_s), engineering strain (ε_s) and strain rate ($\dot{\varepsilon}_s$) under high strain rate loading conditions follow the one-dimensional elastic wave theory and are given by the equations Eq. 2.3,2.4 and 2.5 [8].

5.3 Results and Discussions

5.3.1 Phase and Microstructural Analysis

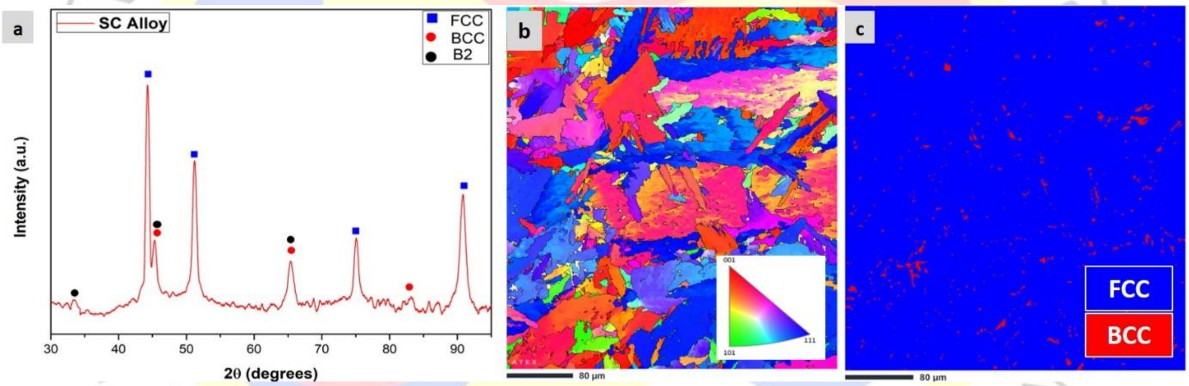

Figure 5.2 (a) the XRD pattern of SC alloy showing the different phase, EBSD images of the SC alloy (b) IPF (c) phase map showing presence of FCC and BCC phases

The XRD analysis of the SC alloy in Fig. 5.2(a) confirmed the presence of both FCC phase and BCC/B2 phase. The lattice parameter for FCC phase was 3.82 Å and that of the BCC/B2 phase was 2.83 Å. The microstructure of the alloy was of dendritic in nature having mixture of lamellar and anomalous grain structure in the IPF image of. The EBSD analysis also revealed the average grain size of 153.6 µm. The phase map shown in Fig. 5.2(c) corroborated the XRD results and displayed the presence of FCC phase (~84 %) and BCC phase in the (~14%) of the alloy respectively. The magnified IPF and the band contrast + phase map of the alloy in Fig. 5.3 (a) and (b) clearly shows the BCC/B2 phase in the interdendritc region and they are finer than the IM alloy and at regions can be equated to precipitates like in case of precipitation hardened $Al_{0.7}CoCrFeNi$ [9]. The kernel average misorientation (KAM) map is an established technique to evaluate the local strain partitioning in an alloy and in this case has been taken with consideration of five neighbouring pixel as shown in Fig. 5.3(c). The KAM map clearly shows the that the residual stress is concentrated along the interdendritic BCC/B2 region in the FCC dendritic matrix. The EDS analysis at dendritic and interdendritic region of the alloy have already been discussed in Chapter 3 that the BCC region was rich in Al concentration and the compositional variation of the elements is listed in the Table 5.1 below. It has been clearly established that in HEAs increase in aluminium concentration stabilizes BCC phase formation [10].

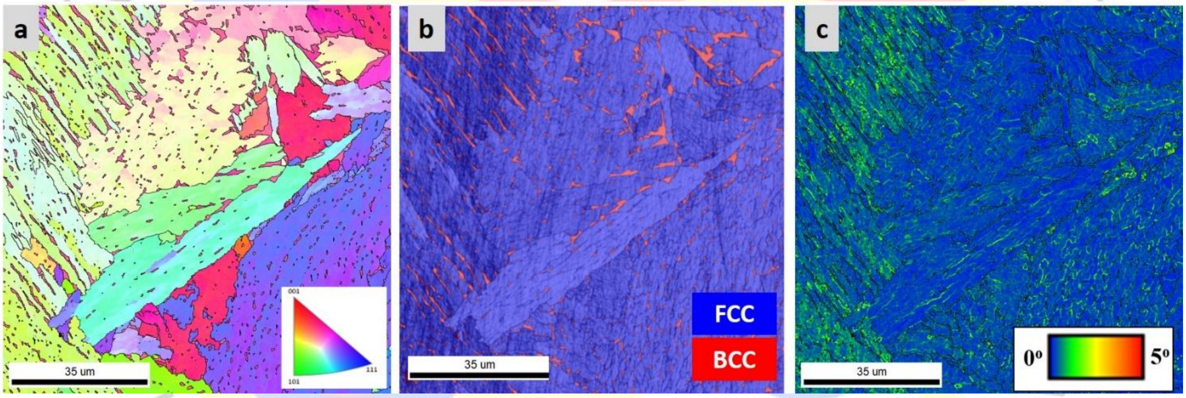

Figure 5.3 Magnified image of the suction-cast alloy (a) IPF (b) band contrast + phase map (c) KAM map

Table 5.1 The compositional variation of the alloy at the dendritic and the interdendritic regions

Zones	Al (wt.%)	Co (wt.%)	Cr (wt.%)	Fe (wt.%)	Ni (wt.%)
Dendritic (FCC)	3	21.5	19.5	35.5	19.7
Interdendritic (BCC)	8.8	18.1	22.8	31	19.4

5.3.2 Mechanical Response

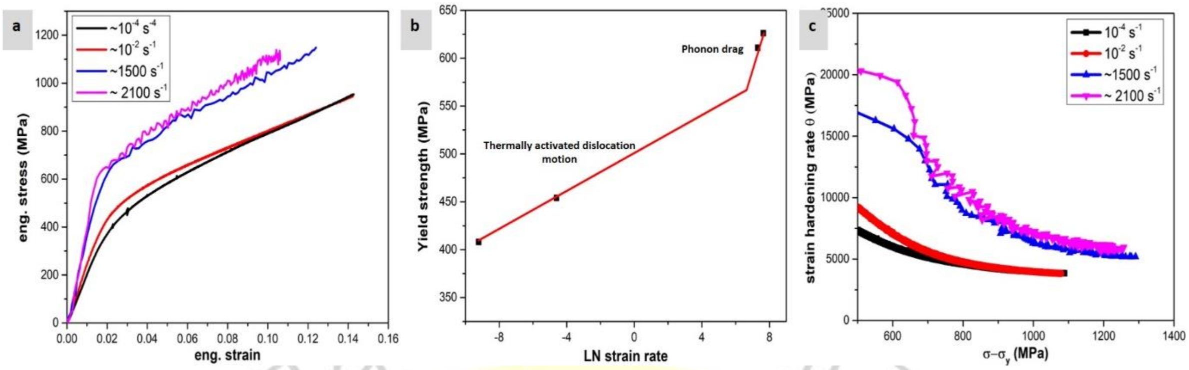

Figure 5.4 Stress strain plots from quasi static compression testing and dynamic deformation using SHPB (b) Varying yield strength with strain rates indicating two distinct regions (c) Kocks-Mecking (K-M) plots showing the variation of strain hardening rate (θ) with flow stress

The quasi-static and the high strain rate stress-strain responses of the suction cast (SC) alloy $Al_{0.65}CoCrFe_2Ni$ are compared under a range of strain rates is shown in Fig. 5.3(a). The quasi-static yield strengths of the alloy at strain rates of ~10^{-4} s^{-1} and ~10^{-2} s^{-1} were 420 ± 10 MPa and 454 ± 5 MPa, respectively. The high strain rate compression tests using SHPB were conducted for stable region of strain rates at ~1500 s^{-1} and ~2100 s^{-1}, and the respective yield strengths were 611 ± 5 MPa and 626 ± 8 MPa. The specimens exhibited considerable ductility without failure under all strain rates. The serrated behaviour of stress-strain curve was observed at high strain rate loading, which is a phenomenon of plastic instability that occurs during high temperature deformation or high strain rate deformation. In particular, during a high strain rate deformation, the complex wave interactions, solute-dislocation interaction, local fluctuation of stress and segregation of elemental composition causes serration [11–13]. The increase in average yield strength with increase in strain rate from 10^{-4} s^{-1} to 2100 s^{-1} was close to 50 %, exhibiting excellent strain rate hardening, which is typical of low stacking fault energy (SFE) alloys like 304L SS and Cu_xAl_y alloys [14]. However, the as-cast (IM) alloy exhibited higher increase in the yield strengths than the SC alloy as the SFE of a material increases with decrease in the grain size.

The slope of the semi-logarithmic yield strength vs. strain rate plot, λ =$\frac{\partial \sigma}{\partial \, In\dot{\varepsilon}}$, shown in Fig. 5.3(b), shows significantly higher strain rate hardening in the high strain rate region compared to quasi-static loading in the SC alloy. The slope in the quasi-static region (λ_I) and in the dynamic region (λ_{II}) were calculated as 7.38 and 44.58, respectively. The difference in strain rate hardening of the alloy under quasi-static and high strain rate loading can be explained on the basis of dislocation activities in the alloy. Generally, the long-range and short-range barriers resist dislocation movements and hinder plastic deformation. Under quasi-static loading, due to the difference in size of the solute atoms in HEAs, the distorted lattice acts as short range barriers to restrict dislocation movements [15,16]. These short-range barriers can be overcome by reaching the thermal activation energy. For the lower slope in the quasi-static region, the thermal-activation dislocation theory was employed to understand the low strain rate sensitivity. The equation for thermal activation energy (ΔG), i.e. Gibbs free energy, is given below in the following equation[17,18]:

$$\Delta G = kT \left(ln \frac{\dot{\varepsilon_0}}{\dot{\varepsilon}}\right) \tag{5.1}$$

where $\dot{\varepsilon_0}$ is the reference strain rate, $\dot{\varepsilon}$ is the strain rate, k is the Boltzmann constant and T is the temperature.

Eq. 5.1 ascertains that the higher is the strain rate $\dot{\varepsilon}$, the lower is the thermal activation energy ΔG needed for the dislocation to overcome the barriers. Furthermore, the activation volume (V^*) is related to the Gibbs free energy as $V^* = \frac{\partial \, \Delta G}{\partial \, \tau^*}$, where τ^* is the effective thermal component of shear. Using Von Mises criterion for yielding, i.e., the relation between shear stress and normal stress $\tau = \frac{\sigma}{\sqrt{3}}$, the activation volume can be expressed as [14,19].

$$V^* = \sqrt{3}\, kT \frac{\partial\, ln\dot{\varepsilon}}{\partial\sigma} = \sqrt{3}\, kT \frac{\partial\, ln\sigma}{m\, \partial\sigma} \qquad 5.2$$

where m is the logarithmic strain rate sensitivity (SRS) (m= $\frac{\partial\, ln\sigma}{\partial\, In\dot{\varepsilon}}$).

Thus, the activation volume for HEAs derived from the above Eq. 5.5, lie between (1-100 b^3) which is significantly smaller compared to conventional FCC metals such as Cu, Cu-Zn [20,21]. The smaller activation volume is attributed to high lattice friction stress and solid solution pinning effect. This contributes to high dislocation interactions resulting in substructures formation [14,20].

The quasi-static deformation process involves thermal activation of dislocation movement. However, for dynamic deformations, the viscoelastic phonon-drag effect play the dominant role in the deformation process because instantaneous increase in temperature reduces the activation energy and high strain deformation is transient in nature where the thermal energy is not fully utilized [17,22,23].

Armstrong *et al.* has proposed the Orowan model to accurately determine the plastic behaviour of the metals under shock wave loading, which can be expressed as [22–24]:

$$\frac{d\varepsilon}{dt} = \frac{1}{m}.\rho b v = \frac{1}{m}.\frac{d\rho}{dt} b\Delta x_d \qquad 5.3$$

where $\frac{d\varepsilon}{dt}$ is the strain rate; m is the orientation factor, b is the Burgers vector, ρ is the mobile dislocation density, v is the dislocation velocity and Δx_d is the separation between dislocation generation. From Eq. 5.6, it can be inferred that higher strain rate of loading leads to higher dislocation velocity. The dislocation velocity at very high strain rates approach the shear wave velocity. The dislocation velocity is related to the frictional force (f) for unit length and the shear stress (τ) during high strain rate loading as given below.

$$f = b\tau = \eta v \qquad 5.4$$

, where η is the drag coefficient. This phonon-drag effect, which becomes operative in the high strain rate deformation, leads to a significant rise in the yield stresses.

The high lattice distortions inherently present in the HEAs also develop local elastic stress field, which interacts with the dislocation stress field, and these interactions impede the dislocation movements under high strain rate loading[25]. The higher strength and the higher strain hardening rate under high strain rate loading can be understood with the help of Taylor equation as given below.

$$v = A\sigma^m \qquad 5.5$$

, where A and m are material constants.

The overall strain rate sensitivity (SRS) of the as-cast alloy, m= $\frac{\partial\, ln\sigma}{\partial\, In\dot{\varepsilon}}$, at a strain of 0.02 was calculated as 0.023 considering two strain rates, 0.0001 s^{-1} and 2100 s^{-1}, across quasi-static and dynamic loading conditions. Similarly, the strain rate sensitivity in the quasi-static range (m_s) was 0.033 and in the dynamic loading (m_d) was 0.072. The SRS(m) of the alloy was higher than conventional FCC metals like Al, Ni, Cu, 304 L *etc.*[14,20] . The SRS(m) reported by Li *et al*. in single-phase FCC-based HEA $Al_{0.3}$CoCrFeNi was 0.053 [23]. The SRS for single-phase FCC-based HEA $Al_{0.1}$CoCrFeNi was 0.033 and 0.009 in the as-cast and the cold-rolled conditions of the alloy, respectively, as per the findings of Gangireddy *et al.* [16,22]. This is obvious that the FCC based HEAs will exhibit higher SRS than dual-phase HEAs having BCC and FCC due to their intrinsic chemical composition and crystal structure [26].The SRS of the suction cast alloy is still higher than for that of Co-free FCC-BCC based dual-phase $AlCrCuFeNi_2$ which was estimated at 0.0124 [27]. For dual-phase alloy $Al_{0.6}CoCrFeNi$ having FCC and BCC phases, having a similar dendritic microstructure as the alloy under the current study fabricated by suction cast, the SRS was evaluated as 0.029. [8]. $Al_{0.6}CoCrFeMnNi$ drop cast and cold rolled exhibited a SRS 0.024 but with lower strength than the SC alloy [26].A hypo-eutectic alloy precipitation hardened $Al_{0.7}CoCrFeNi$ having FCC and BCC phases with lamellar microstructure showed significantly reduced SRS of 0.018. Therefore, the fabrication route of re-melting an HEA and rapidly cooling the alloy proves to be an effective and easy way of not only increasing the strength of the alloy but also retain good strain rate sensitivity.

In general, the strain rate sensitivity depends on the relative contributions of temperature-dependent strengthening factors that influence slip and dislocation activities. The microstructure of a material largely influences the dislocation motion and the SRS of the material. However, the dislocation hindrances are caused by both long-range athermal obstacles and short-range thermal obstacles. The relative dominance of the above two types of obstacles eventually impacts the value of SRS. The mechanical threshold stress (MTS) model formulates the total stress (σ) required for deformation as [16,28]:

$$\sigma = \sigma_{thermal} + \sigma_{athermal} \tag{5.6}$$

The thermal contributions of stress are from the frictional stress σ_{fs}, Peierls Nabarro (σ_{P-N}) stress and the solid solution strengthening (σ_{ss}). The higher values of these stress contributors increase the SRS values of an alloy system. The athermal barriers in the form of grain boundaries (σ_{GB}), dislocation density (σ_{DIS}) and twin boundaries (σ_{TW}) adversely impact the SRS of a material. The dislocation density strengthening was one of the dominant strengthening contributor in the SC alloy as reported in a previous work published by the authors [6]. In addition, the smaller grain size of the SC alloy, which led to higher number of long-range athermal obstacles in the form of grain boundaries compared to IM alloy, resulted in lower strain rate sensitivity than the as-cast condition [28].

The Kocks-Mecking (K-M) plot of strain hardening rate ($\theta = \frac{d\sigma}{d\epsilon}$) vs flow stress ($\sigma - \sigma_y$) is presented in Fig. 5.3(c). The plot consists of three stages of strain hardening rate in all the cases of loading. The dynamic strain hardening rate for the SC alloy was higher values, $\theta = 5859.05$ MPa for strain rate of 2100 s^{-1}, than the quasi-static condition, $\theta = 3906.03$ MPa for strain rate of 10^{-4} s^{-1} before the respective strain hardening rate curve plateaus, because of the phonon drag which became activated at high strain rates as mentioned in Eq. 5.7 and Eq.5.8. In addition, the various substructure formation associated with dynamic loading could be the reasons for higher strain hardening rate compared to quasi-static loading [21,29]. The higher strain hardening rate in the SC alloy compared to the IM alloy largely is due to the smaller grain size and Taylor hardening effect resulting from higher residual thermal stresses that impacts the plastic deformation behaviour of material also[30,31]. However, like the IM alloy, slip was the dominant deformation mechanism in both quasi-static and dynamic compression tests for the SC alloy. To further investigate the appropriate reasons, the post-deformation microstructures are analysed in the next section.

5.3.3 Deformation Mechanisms

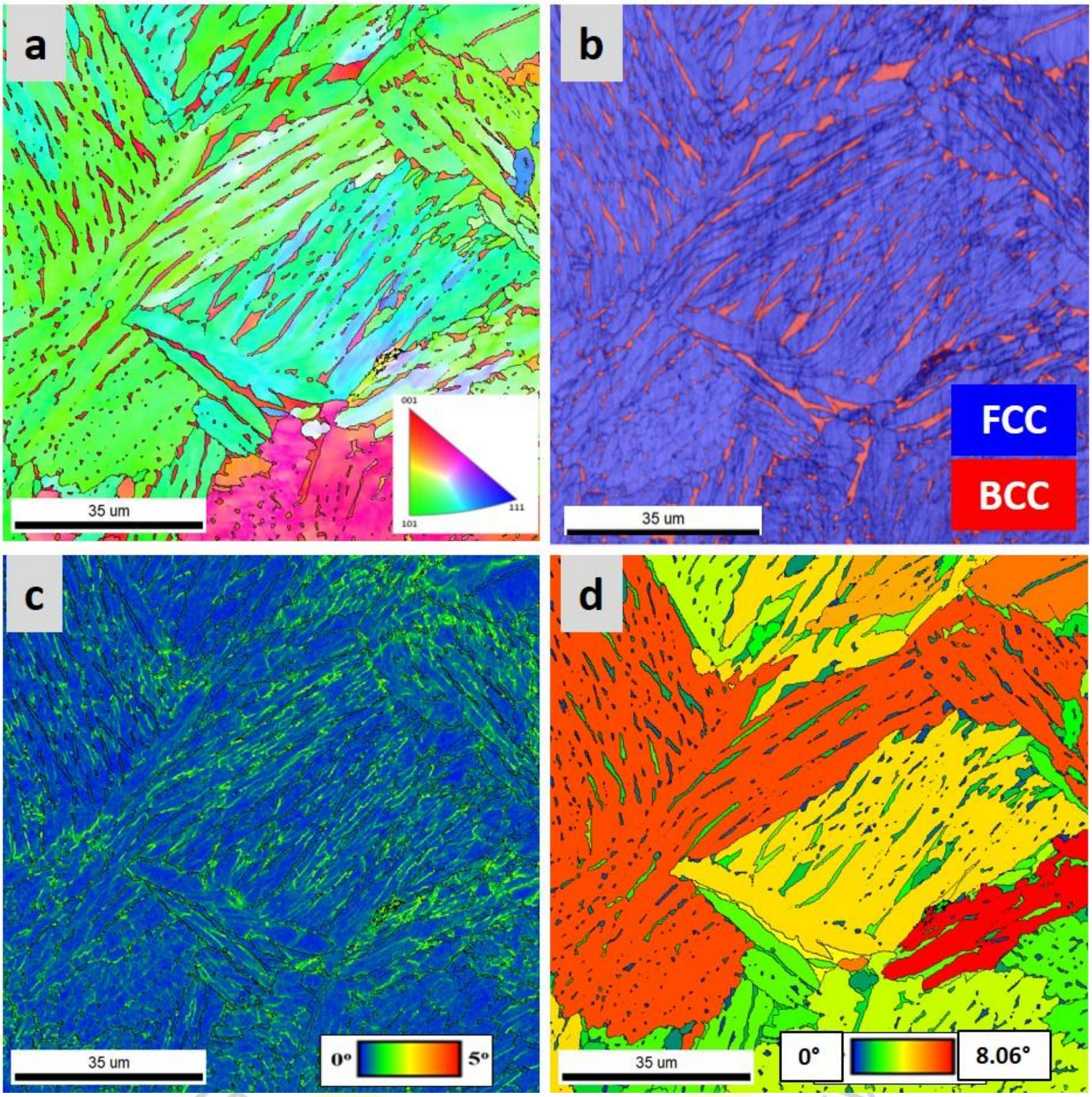

Figure 5.5 EBSD images of deformed suction cast (SC) alloy at a nominal strain of ~12% compressed at a strain rate of 10^{-4} s^{-1}: (a)IPF, (b) band contrast + phase map, (c) KAM map showing areas of high dislocation densities, (d) GOS map

Fig.5.5 and 5.6 consist of the inverse pole figure (IPF), the band contrast + phase map, the kernel average misorientation (KAM) map and the grain orientation spread (GOS) maps in the direction compression of the deformed SC alloy sample compressed at a strain rate of ~10^{-4} s^{-1} and 2100 s^{-1}. With the help of these maps show the dislocation distributions and various substructure formations will be analysed to understand the strain hardening behaviour and deformation mechanisms involved under quasi static loading at a nominal strain of ~12% and compared with the deformation behaviour of the alloy under high strain rate loading conditions at similar strain.

In our previous study of the SC alloy studied in the Chapter 3 the SC alloy was strained at a relatively higher value of ~25% at quasi static loading and for this reason not utilised under this study to compare with the high strain deformation behaviour. The IPF [001] map extracted from the orientation image maps in Fig 5.5 (a) and band contrast + phase map in Fig 5.5(b), clearly shows that there is a high degree of misorientation between the FCC matrix and the BCC interdendritic region which results out high lattice misfit between the crystal structure. KAM maps are good indicators of local strain fields and dislocation accumulation. In fact, KAM represents the amount of geometrically necessary dislocation which can be given the following equation [32]:

$$\rho_{GND} = \frac{\alpha\, KAM}{bx} \qquad 5.7$$

, where ρ_{GND} is the density of GNDs, b is the magnitude of Burgers vector, α depends on the type of the grain boundary and x is the scan-step size. The average GND values after quasi static deformation in the SC alloy was 4.5×10^{14} m^{-2}. The KAM map in Fig. 5.5 (c) suggest that the FCC matrix is deformed extensively and the dislocation generate in the FCC matrix along interphase BCC boundary. This is consistent with proven literature that FCC phase being softer deforms more than harder BCC phase[33,34]. In addition, there is large local strain gradient between the FCC matrix interior which has relatively lower KAM values compared to the contours of the FCC phase. The GOS map is another indicator of intragranular misorientation and in Fig 5.5 (d), it is clearly demonstrated that the FCC matrix is heavily deformed with GOS values as high as 8.06 ° compared to the BCC interdendritic region is deformed. Thus, like in DP steel the softer and coarser matrix determines the plasticity of the alloy [32]. No traces of deformation bands or deformation twins were seen in the as-cast IM alloy were observed in the SC alloy under quasi static deformation [6]. Since, transmission electron microscopy is not carried out in this analysis, the possibility of formation of nano-twins cannot be ruled out.

The high strain rate deformation of the SC alloy resulted in elongated grains and with low strain gradient in the FCC resulting in homogeneous deformation as can be seen in Fig 5.6 (a), (b) and (c). This inhomogeneous deformation reflected by the KAM map (Fig. 5.6 (c))is a typical deformation under high strain rate because the phonon drag effect reduces dynamic recovery and increases dislocation motion. The GOS map indicate also indicates higher intragranular misorientation than the quasi static condition with maximum values of 51.06°. Similar to the quasi static deformation the BCC interdendritic phase are not deformed as indicated in the GOS map for the same region of being the harder and finer phase.

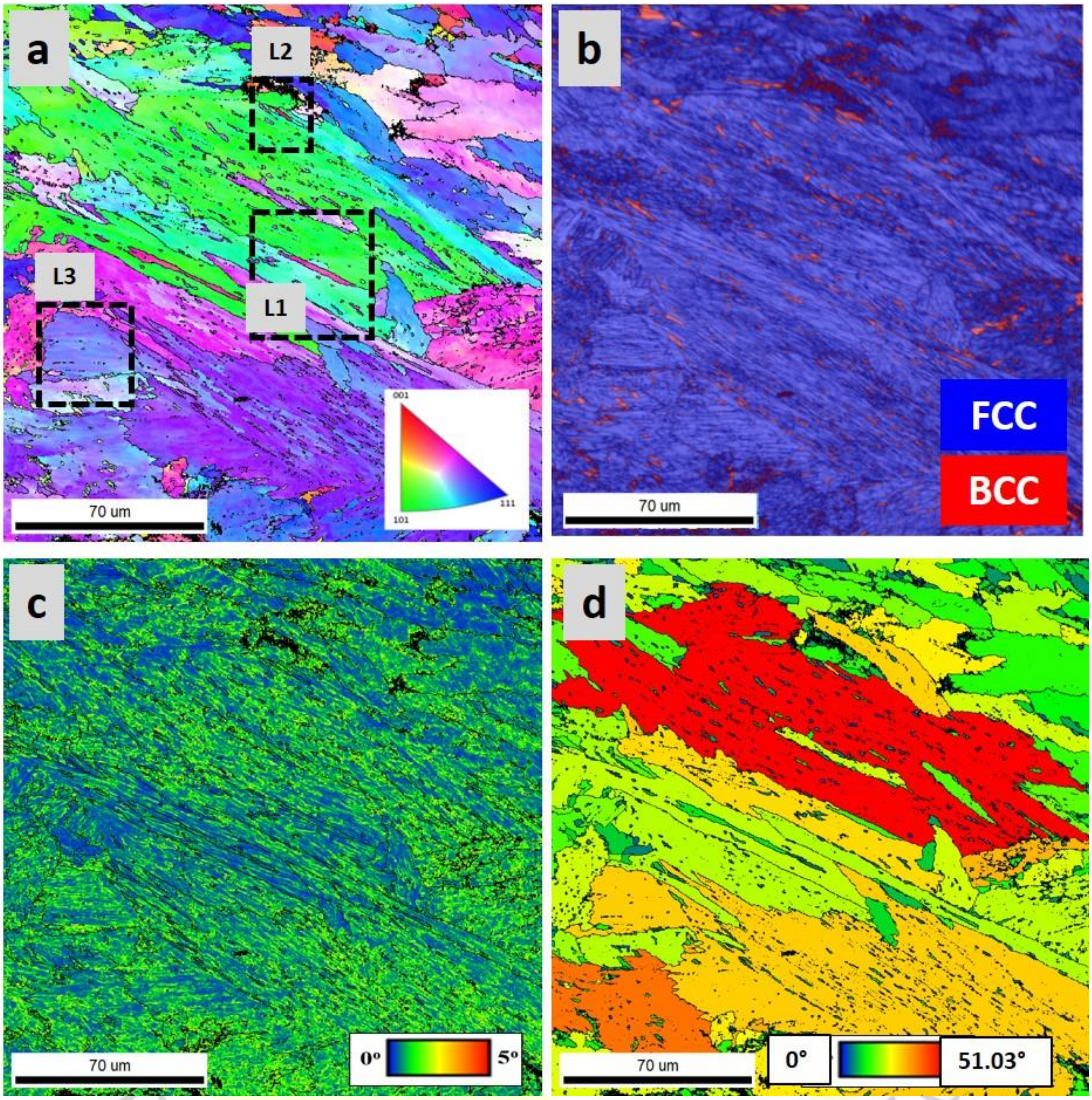

Figure 5.6 EBSD images of deformed suction cast (SC) alloy at a nominal strain of ~12% compressed at a strain rate of 2100 s^{-1}: (a)IPF, (b) band contrast + phase map, (c) KAM map showing areas of high dislocation densities, (d) GOS map

The high strain rate deformation of the SC alloy resulted in elongated grains and with low strain gradient in the FCC resulting in homogeneous deformation as can be seen in Fig 5.6 (a), (b) and (c). This homogeneous deformation reflected by the KAM map (Fig. 5.6 (c))is a typical deformation under high strain rate because the phonon drag effect reduces dynamic recovery and increases dislocation motion. The GOS map indicate also indicates higher intragranular misorientation than the quasi static condition with maximum values of 51.06°.

Similar to the quasi static deformation the BCC interdendritic phase are not deformed as indicated in the GOS map for the same region of being the harder and finer phase.

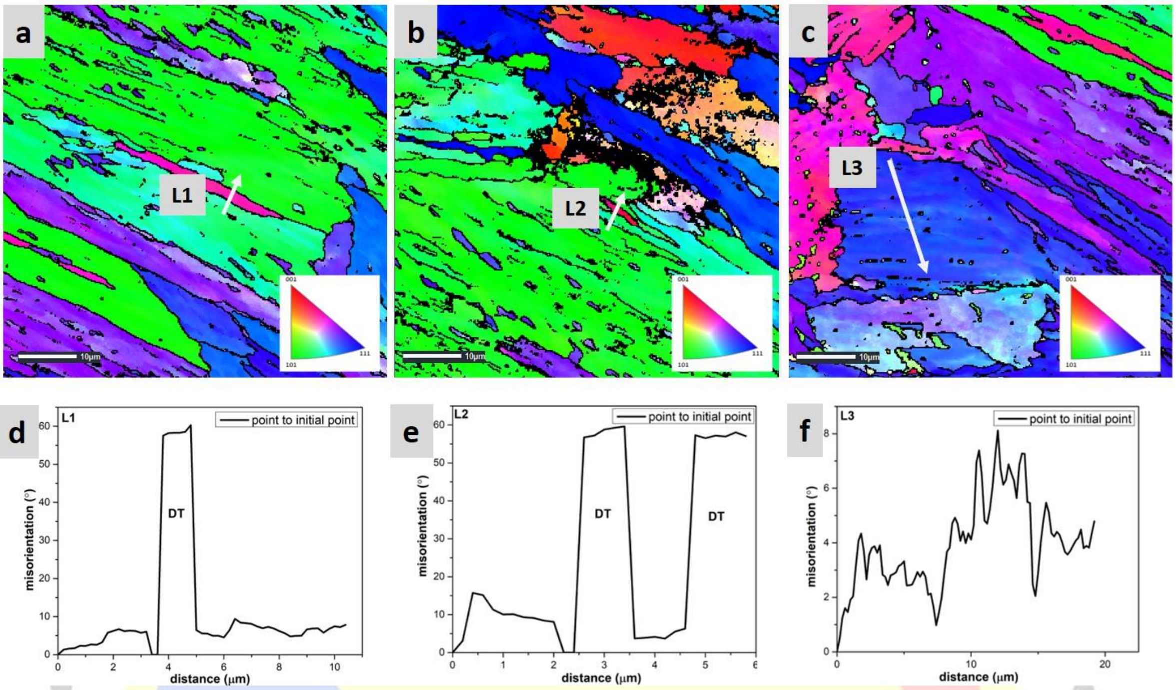

Figure 5.7 Magnified IPF images maps of the alloy deformed at high strain rate and marked as square in the previous figure at specified location (a), (b)and (c) and their respective misorientation plots (d), (e) and (f)

A major energy storage deformation substructure in the SC alloy under dynamic loading was the deformation twins (DTs) with CSL $\sum 3 = 60°$ misorientation near the BCC-FCC interphase boundaries as shown in Fig. 5.6(a) and (b). The point to initial point misorientation lines are measured which are indicated by lines L1 and L2 and they exhibited misorientation between 58.5° to 63.5° (Fig. 5.6 (d) and (e)) confirming the presence of deformation twins. As mentioned above, the interphase boundaries also act as zones of high dislocation density making them high energy sites for probable twin formation. Therefore, a mixed mode of deformation mechanism, i.e., dislocation slip and deformation twinning, was observed in the as-cast alloy under dynamic loading. The critical stress for twin formation (σ_T) can be expressed by the following equation [8]:

$$\sigma_T = \frac{2\gamma_{SF}}{mb_p} \qquad 5.8$$

where γ_{SF} is the stacking fault energy (SFE), m is the average Schmid factor and b_p is the Burgers vector. Although the stacking fault energy of the dual-phase SC alloy can be close to 150 mJ/m^2 as reported for similar high entropy alloy $Al_{0.6}CoCrFeNi$, the FCC region the SFE of the alloy was estimated around 36mJ/m^2, which makes them conducive for twin formation as per Eq. 5.11 [8]. The formation of additional twin boundary induce back stress which hinder the mean free path of the dislocation and increase strain storage capacity by creating heavy dislocation pile-ups with significantly higher than high angle grain boundaries [35]. Therefore, deformation twinning enhanced the strain hardening behaviour of the SC alloy under high strain rate. However, the propensity of formation of twins were lower than the as-cast IM alloy as the SFE of a material increases with decrease in the grain size[36]. The formation of deformation bands resulting out the deformation under high strain was another feature which was noticed in the SC alloy. These deformation bands also act as excellent strain hardening instruments which enhances the plastic strengthening of the SC alloy at dynamic deformation.

5.4 Summary

The suction cast (SC) alloy $Al_{0.65}CoCrFe_2Ni$ prepared re-melted from the industrially melted as-cast (IM) alloy and solidified at faster cooling rate also comprised of both FCC phase and BCC phase with average grain size reduced significantly to 153.6 µm. The high strain rate loading response and associated deformation mechanisms of the SC alloy can be summarized as follows.

(a) The dual-phase suction cast (SC) alloy exhibited lower strain rate sensitivity (SRS) compared to as-cast (IM) alloy having due to dominant smaller grain size and high dislocation strengthening resulting out of rapid cooling of solidification.

(b) The strain hardening rate of the suction cast (SC) alloy was higher at dynamic loading compared to the as-cast (IM) alloy due smaller interdendritic BCC phase, lower grain size and higher residual thermal stresses.

(c) The deformation of the suction cast alloy under quasi static deformation was characterised by high strain gradient in the FCC matrix with higher strains in the contours of the matrix and negligible strains in the interior representing a homogenised deformation.

(d) Under dynamic loading the SC alloy deformation was homogeneous with high dislocation generation and low dynamic recovery resulting in formation of deformation twins and deformation bands.

Although, the outstanding strain rate sensitivity of the as-cast dual-phase high entropy alloy was compromised under rapid solidification, the overall decrease in the value was moderate and excellent strain hardening features due to deformation bands and deformation twins were still observed at high strain rate loading. Therefore, it can be said that re-melting the as-cast alloy and rapidly solidifying them can act as fast and effective mechanism to improve the overall mechanical properties of the alloy.

References

[1] X. Yang, Y. Zhang, Prediction of high-entropy stabilized solid-solution in multi-component alloys, Mater. Chem. Phys. 132 (2012) 233–238. https://doi.org/10.1016/j.matchemphys.2011.11.021.

[2] S. Guo, C.T. Liu, Phase stability in high entropy alloys: Formation of solid-solution phase or amorphous phase, Prog. Nat. Sci. Mater. Int. (2011). https://doi.org/10.1016/S1002-0071(12)60080-X.

[3] J.W. Yeh, Alloy design strategies and future trends in high-entropy alloys, JOM. 65 (2013) 1759–1771. https://doi.org/10.1007/s11837-013-0761-6.

[4] K.Y. Tsai, M.H. Tsai, J.W. Yeh, Sluggish diffusion in Co-Cr-Fe-Mn-Ni high-entropy alloys, Acta Mater. (2013). https://doi.org/10.1016/j.actamat.2013.04.058.

[5] Y.F. Ye, Q. Wang, J. Lu, C.T. Liu, Y. Yang, High-entropy alloy: challenges and prospects, Mater. Today. (2016). https://doi.org/10.1016/j.mattod.2015.11.026.

[6] S. Tamuly, S. Dixit, B. Kombaiah, P. Khanikar, Strengthening Mechanisms and Deformation Behavior of Industrially-Cast and Lab-Cast Dual-Phase High Entropy Alloy, Met. Mater. Int. (2022). https://doi.org/10.1007/s12540-022-01211-x.

[7] Website, www.atex-software.eu, (n.d.). http://www.atex-software.eu/ (accessed December 25, 2021).

[8] L. Wang, J.W. Qiao, S.G. Ma, Z.M. Jiao, T.W. Zhang, G. Chen, D. Zhao, Y. Zhang, Z.H. Wang, Mechanical response and deformation behavior of Al0.6CoCrFeNi high-entropy alloys upon dynamic loading, Mater. Sci. Eng. A. 727 (2018) 208–213. https://doi.org/10.1016/j.msea.2018.05.001.

[9] S. Gangireddy, B. Gwalani, V. Soni, R. Banerjee, R.S. Mishra, Contrasting mechanical behavior in precipitation hardenable AlXCoCrFeNi high entropy alloy microstructures: Single phase FCC vs. dual phase FCC-BCC, Mater. Sci. Eng. A. 739 (2019) 158–166. https://doi.org/10.1016/j.msea.2018.10.021.

[10] C. Li, J.C. Li, M. Zhao, Q. Jiang, Effect of aluminum contents on microstructure and properties of Al xCoCrFeNi alloys, J. Alloys Compd. (2010). https://doi.org/10.1016/j.jallcom.2010.03.111.

[11] M.N. Hasan, J. Gu, S. Jiang, H.J. Wang, M. Cabral, S. Ni, X.H. An, M. Song, L.M. Shen, X.Z. Liao, Effects of elemental segregation on microstructural evolution and local mechanical properties in a dynamically deformed CrMnFeCoNi high entropy alloy, Scr. Mater. 190 (2021) 80–85. https://doi.org/10.1016/j.scriptamat.2020.08.048.

[12] S. Chen, W. Li, F. Meng, Y. Tong, H. Zhang, K.K. Tseng, J.W. Yeh, Y. Ren, F. Xu, Z. Wu, P.K. Liaw, On temperature and strain-rate dependence of flow serration in HfNbTaTiZr high-entropy alloy, Scr. Mater. 200 (2021) 113919. https://doi.org/10.1016/j.scriptamat.2021.113919.

[13] S. Niu, H. Kou, Y. Zhang, J. Wang, J. Li, The characteristics of serration in Al0.5CoCrFeNi high entropy alloy, Mater. Sci. Eng. A. 702 (2017) 96–103. https://doi.org/10.1016/j.msea.2017.05.075.

[14] W. Jiang, X. Gao, Y. Guo, X. Chen, Y. Zhao, Dynamic impact behavior and deformation mechanisms of Cr26Mn20Fe20Co20Ni14 high-entropy alloy, Mater. Sci. Eng. A. 824 (2021) 141858. https://doi.org/10.1016/j.msea.2021.141858.

[15] L. Wang, J.W. Qiao, S.G. Ma, Z.M. Jiao, T.W. Zhang, G. Chen, D. Zhao, Y. Zhang, Z.H. Wang, Mechanical response and deformation behavior of Al0.6CoCrFeNi high-entropy alloys upon dynamic loading, Mater. Sci. Eng. A. (2018). https://doi.org/10.1016/j.msea.2018.05.001.

[16] S. Gangireddy, L. Kaimiao, B. Gwalani, R. Mishra, Microstructural dependence of strain rate sensitivity in thermomechanically processed Al0.1CoCrFeNi high entropy alloy, Mater. Sci. Eng. A. 727 (2018) 148–159. https://doi.org/10.1016/j.msea.2018.04.108.

[17] M. lei Hu, W. dong Song, D. bo Duan, Y. Wu, Dynamic behavior and microstructure characterization of TaNbHfZrTi high-entropy alloy at a wide range of strain rates and temperatures, Int. J. Mech. Sci. 182 (2020) 105738. https://doi.org/10.1016/j.ijmecsci.2020.105738.

[18] M.R. Chen, S.J. Lin, J.W. Yeh, S.K. Chen, Y.S. Huang, C.P. Tu, Microstructure and properties of Al0.5CoCrCuFeNiTix (x = 0-2.0) high-entropy alloys, in: Mater. Trans., 2006: p. Vol.47 No. 5 1396-1401. https://doi.org/10.2320/matertrans.47.1395.

[19] Y.M. Wang, A. V. Hamza, E. Ma, Temperature-dependent strain rate sensitivity and activation volume of nanocrystalline Ni, Acta Mater. 54 (2006) 2715–2726. https://doi.org/10.1016/j.actamat.2006.02.013.

[20] X. Zhong, Q. Zhang, M. Ma, J. Xie, M. Wu, S. Ren, Y. Yan, Dynamic compressive properties and microstructural evolution of Al1.19Co2CrFeNi1.81 eutectic high entropy alloy at room and cryogenic temperatures, Mater. Des. 219 (2022) 110724. https://doi.org/10.1016/j.matdes.2022.110724.

[21] J.M. Park, J. Moon, J.W. Bae, M.J. Jang, J. Park, S. Lee, H.S. Kim, Strain rate effects of dynamic compressive deformation on mechanical properties and microstructure of CoCrFeMnNi high-entropy alloy, Mater. Sci. Eng. A. 719 (2018) 155–163. https://doi.org/10.1016/j.msea.2018.02.031.

[22] N. Kumar, Q. Ying, X. Nie, R.S. Mishra, Z. Tang, P.K. Liaw, R.E. Brennan, K.J. Doherty, K.C. Cho, High strain-rate compressive deformation behavior of the Al0.1CrFeCoNi high entropy alloy, Mater. Des. 86 (2015) 598–602. https://doi.org/10.1016/j.matdes.2015.07.161.

[23] Z. Li, S. Zhao, H. Diao, P.K. Liaw, M.A. Meyers, High-velocity deformation of Al0.3 CoCrFeNi high-entropy alloy: Remarkable resistance to shear failure, Sci. Rep. 7 (2017) 1–8. https://doi.org/10.1038/srep42742.

[24] S. Jiang, Z. Lin, H. Xu, Y. Sun, Studies on the microstructure and properties of Al x CoCrFeNiTi 1-x high entropy alloys, J. Alloys Compd. (2018). https://doi.org/10.1016/j.jallcom.2018.01.247.

[25] I. Basu, J.T.M. De Hosson, Strengthening mechanisms in high entropy alloys: Fundamental issues, Scr. Mater. 187 (2020) 148–156. https://doi.org/10.1016/j.scriptamat.2020.06.019.

[26] C.M. Cao, W. Tong, S.H. Bukhari, J. Xu, Y.X. Hao, P. Gu, H. Hao, L.M. Peng, Dynamic tensile

deformation and microstructural evolution of AlxCrMnFeCoNi high-entropy alloys, Mater. Sci. Eng. A. 759 (2019) 648–654. https://doi.org/10.1016/j.msea.2019.05.095.

[27] S.G. Ma, Z.M. Jiao, J.W. Qiao, H.J. Yang, Y. Zhang, Z.H. Wang, Strain rate effects on the dynamic mechanical properties of the AlCrCuFeNi2 high-entropy alloy, Mater. Sci. Eng. A. 649 (2016) 35–38. https://doi.org/10.1016/j.msea.2015.09.089.

[28] S. Gangireddy, B. Gwalani, K. Liu, R. Banerjee, R.S. Mishra, Microstructures with extraordinary dynamic work hardening and strain rate sensitivity in Al0.3CoCrFeNi high entropy alloy, Mater. Sci. Eng. A. 734 (2018) 42–50. https://doi.org/10.1016/j.msea.2018.07.088.

[29] M. Zhang, L. Zhang, J. Fan, G. Li, P.K. Liaw, R. Liu, Microstructure and enhanced mechanical behavior of the Al 7 Co 24 Cr 21 Fe 24 Ni 24 high-entropy alloy system by tuning the Cr content, Mater. Sci. Eng. A. (2018). https://doi.org/10.1016/j.msea.2018.07.069.

[30] U.F. Kocks, H. Mecking, Physics and phenomenology of strain hardening: The FCC case, Prog. Mater. Sci. 48 (2003) 171–273. https://doi.org/10.1016/S0079-6425(02)00003-8.

[31] B.K. Choudhary, J. Christopher, E. Isaac Samuel, Applicability of Kocks-Mecking approach for tensile work hardening in P9 steel, Mater. Sci. Technol. (United Kingdom). (2012). https://doi.org/10.1179/1743284711Y.0000000106.

[32] A. Das, S. Tarafder, S. Sivaprasad, D. Chakrabarti, Influence of microstructure and strain rate on the strain partitioning behaviour of dual phase steels, Mater. Sci. Eng. A. 754 (2019) 348–360. https://doi.org/10.1016/j.msea.2019.03.084.

[33] R. Sonkusare, A. Swain, M.R. Rahul, S. Samal, N.P. Gurao, K. Biswas, S.S. Singh, N. Nayan, Establishing processing-microstructure-property paradigm in complex concentrated equiatomic CoCuFeMnNi alloy, Mater. Sci. Eng. A. 759 (2019) 415–429. https://doi.org/10.1016/j.msea.2019.04.096.

[34] R. Sonkusare, R. Jain, K. Biswas, V. Parameswaran, N.P. Gurao, High strain rate compression behaviour of single phase CoCuFeMnNi high entropy alloy, J. Alloys Compd. (2020). https://doi.org/10.1016/j.jallcom.2020.153763.

[35] I. Basu, V. Ocelík, J.T.M. De Hosson, BCC-FCC interfacial effects on plasticity and strengthening mechanisms in high entropy alloys, Acta Mater. 157 (2018) 83–95. https://doi.org/10.1016/j.actamat.2018.07.031.

[36] Z. Li, C.C. Tasan, K.G. Pradeep, D. Raabe, A TRIP-assisted dual-phase high-entropy alloy: Grain size and phase fraction effects on deformation behavior, Acta Mater. 131 (2017) 323–335. https://doi.org/10.1016/j.actamat.2017.03.069.

Chapter 6 Strengthening Mechanisms, Strain Rate Effects and Deformation of Friction Stir Processed Dual-Phase High Entropy Alloy

6.1 Introduction

In this chapter, the effect of a single step thermo-mechanical processing in the form of friction stir processing on the industrially melted as-cast alloy dual-phase HEA with FCC and BCC phases was investigated. The hardness, compressive strength, strength contributions and strain rate sensitivity and strain hardening behaviour were determined in this chapter. The high strain rate loading behaviour is carried out using split Hopkinson pressure bar (SHPB) at strain rates of the order of 10^3 s^{-1}. The deformation mechanisms and strain partitioning involved under a wide range of strain rate were observed through microstructural characterisation.

6.2 Material and Methodology

The high entropy alloy $Al_{0.65}CoCrFe_2Ni$ was prepared by vacuum induction melting at industrial environment at large scale (~60 kg) setup at Mishra Dhatu Nigam Limited, (MIDHANI) Hyderabad. As mentioned, the composition of the as-cast (IM) alloy was maintained within the definition of HEA with respect to configurational entropy, size effect, enthalpy and combined effect. The dual-phase nature of the alloy was predicted through VEC rule and confirmed in our previous work [1]. Sheets with dimension 100 mm × 75 mm × 5.25 mm were cut from the as-cast base metal (BM) alloy billet using wire-electrical discharge machining (EDM). Friction stir processing (Fig. 6.1(b)) was undertaken by a conical pin stir tool made of tungsten carbide tool (WC-10% Co) with dimensions as represented in Fig. 6.1(a) at transverse speed of 50 mm/min with rotational speed of 300 r.p.m., plunge depth of

0.3 mm and tilt angle of 2°. The final defect free friction stir processed alloy in a single pass was also shown in Fig. 6.1 (c).

The FSP alloy samples of as-cast alloy $Al_{0.65}CoCrFe_2Ni$, having cylindrical dimensions of 5.25 mm diameter and 5.25 mm height, were compressed under quasi static conditions of strain rates of ~ 10^{-4} s^{-1} and 10^{-2} s^{-1} at room temperature using Instron 8801 universal testing machine. The dynamic deformation was tested using split Hopkinson pressure bar (SHPB) setup at Indian Institute of Technology Kanpur. The sample sizes for carrying out high strain rate deformation are cylinders with 6 mm diameter and 5.25 mm height. The strain gauges were mounted in a diametrically opposite arrangement on the incident and the transmission bar. The stress, strain and strain rate of the specimen under study were evaluated based on one dimensional wave elastic wave theory given by the equations 2.3,2.4 and 2.5.

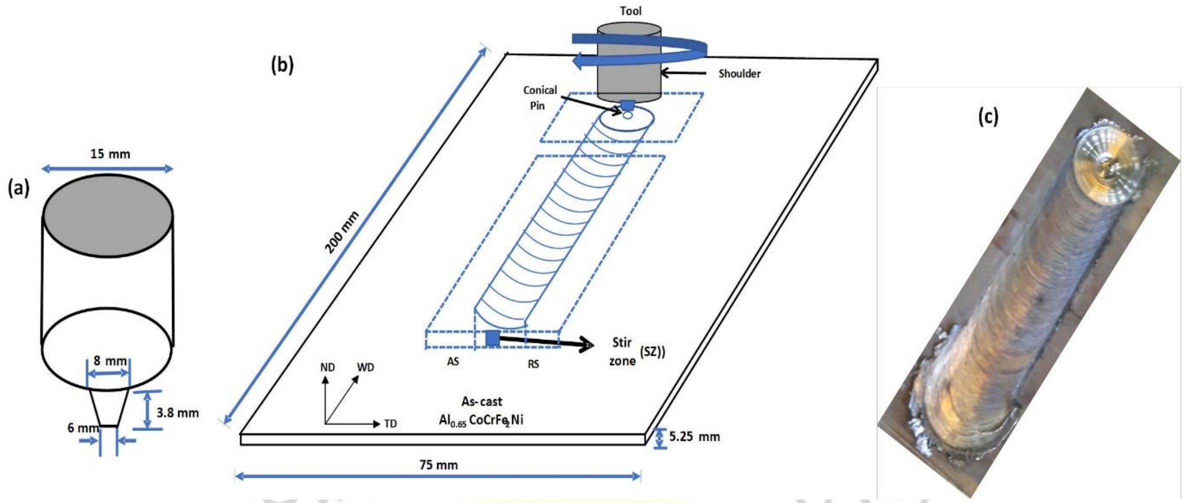

Figure 6.1 Schematic of (a) FSP tool geometry (b) Schematic of FSP (c) FSP alloy

The micro Vickers hardness across the transverse section of the sample comprising of the approaching side (AS), stir zone (SZ) and the retreating side (RS). The macrostructure of the FSP alloy was taken using NIKON made stereo zoom microscope. Microstructural and phase investigation identification for the alloy were carried out using optical microscope, X-ray diffraction (XRD) and scanning electron microscopy (SEM) techniques. The XRD analysis was performed with Cu-k$_{\alpha}$ radiation (λ=1.5406 $\boldsymbol{A}^{\circ}$) operating at 50kV/160mA in a Rigaku made instrument. After fine mechanical polishing, the FSP alloy sample was etched with aqua regia before observing under optical microscope and scanning electron microscope as per ASTM E3 standard. Field emission scanning electron microscope (FE-SEM) integrated with energy dispersive X-ray (EDS) detectors were used to examine the microstructure as well as elemental mapping at different locations of the processed alloy sample. Well-polished FSP alloy samples before and after deformation were used to evaluate the average grain size, identify phases and measure the various orientations of grains and other microstructures in the alloy with the help of Oxford instruments made electron backscatter diffraction system. The orientation image maps have been generated using TSL-OIM and ATEX software [4].

6.3 Results and discussions

6.3.1 Macrostructure, Phase and Microstructure

The macrostructure of the transverse section of the FSP alloy comprising of the was shown in Fig. 6.2(a), where it was observed that the depth of stir zone was ~4 mm on the as-cast base metal (BM) with no major processing defects. The optical micrograph in Fig. 6.2(b) clearly show the grain refinement associated with friction stir processing and the original dendritic structure of the as-cast alloy dissolved after processing. The XRD pattern in Fig. 6.2(c) of the processed alloy in comparison to the as-cast alloy shows that the intensity for BCC phase increased and the intensity for FCC phase decreased establishing the TRIP effect. The phase transformation which occurred due to severe plastic deformation, resulted out of initial decrease in the lattice parameter for FCC phase from 3.84 Å to 3.62 Å which eventually on further straining result in TRIP effect, whereas the lattice parameter for BCC phase remained unchanged at 2.86 Å. Furthermore, decrease in lattice parameter of FCC phase translates into phase transformation with increased plastic deformation which is the basis of

TRIP effect [5–8]. The inverse pole figure (IPF) and phase maps of the as-cast (IM) alloy and the processed alloy are shown in Fig. 6.2(d-f) and these figures are consistent with the findings of the optical micrograph (Fig. 6.2(b)) and the XRD patterns (Fig. 6.2(c)). Significant grain refinement in the FSP alloy was observed compared to the as-cast alloy where the original grain size was of the order of 10^3 µm as seen in the IPF figures Fig. 6.2(d) and (e). The phase maps of the as-cast (IM) and the FSP samples (Fig. 2 (f) and (g)) clearly demonstrates the TRIP effect where the BCC phase increased from nearly 15% in the as-cast conditions to 92% in the FSP sample at the expense of the FCC phase [9]. The higher the percentage of FCC phase in the as-cast (IM) conditions the higher is probability of TRIP effect[9,10].

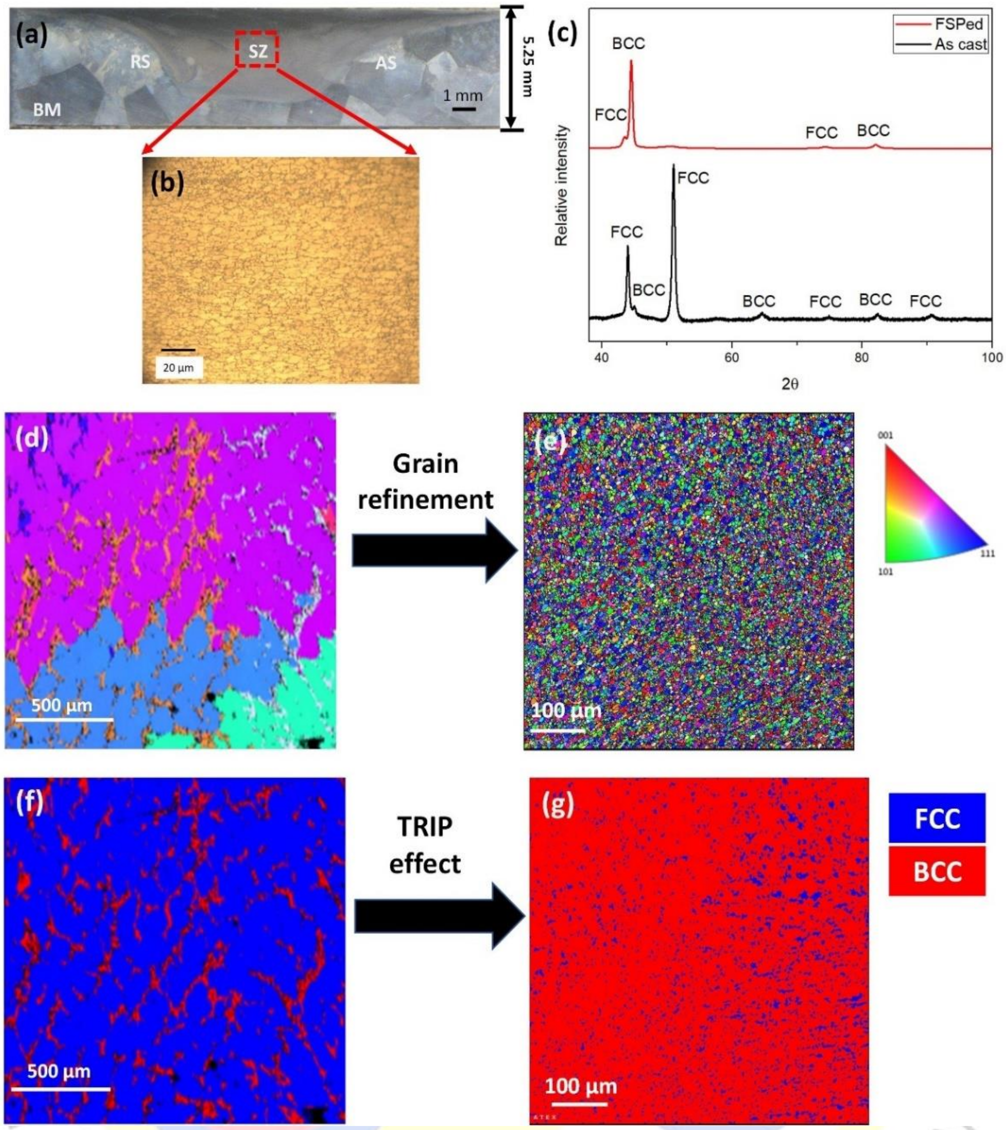

Figure 6.2 (a) Macrostructure of the FSP alloy (b) Optical micrograph of the refined stir zone (SZ) (d) XRD pattern before and after FSP; the IPF images of the as-cast alloy and FSP alloy are shown in (d) and (e) respectively; the phase map of the as-cast alloy and FSP are shown in (f) and (g) respectively.

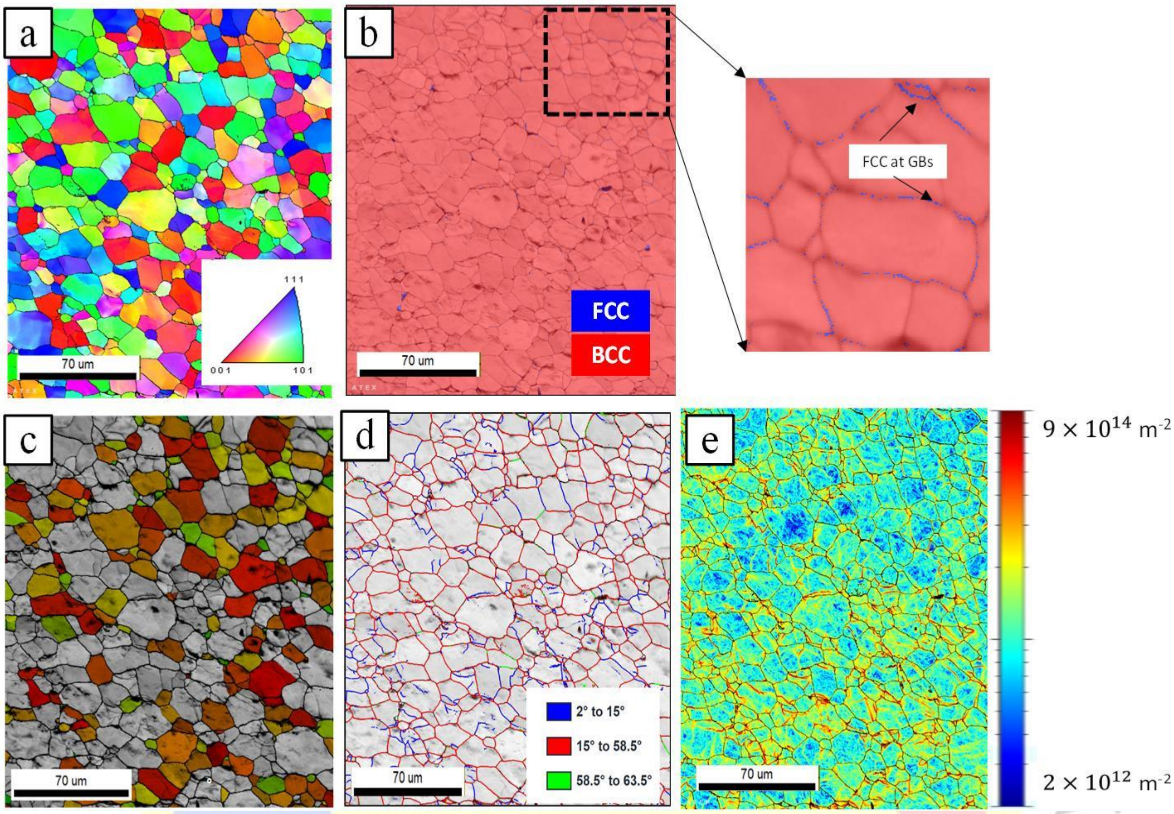

Figure 6.3 Magnified (a) IPF map (b) Phase Map + Band Contrast (BC) map (c)GOS <2° map showing the amount of recrystallization (d) Misorientation distribution plot correlated and non-correlated

On examining the magnified IPF map and the phase + band contrast map in Fig. 6.3(a) and (b) of the FSP alloy showed that the spinodal morphology present in the as-cast alloy [1] were completely diluted . The FCC phase confined to the grain boundaries as can be seen in the magnified region of Fig. 6.3(b) with higher Al and Ni content in the BCC region occupying the grain interiors, and Fe and Cr rich FCC region as observed in other dual-phase HEAs [11] listed in Table 6.1 . The grain size decreased after FSP to an average of 15.45± 3 µm having random orientation as seen in the IPF map of Fig. 6.3(a). Dynamic recrystallization (DRX) which is a common phenomenon occurring in FSP and other thermomechanical processing for materials like Al based HEAs is the main reason behind grain refinement [12,13]. The IPF image (Fig. 6.3(a))) clearly established that the recrystallization was combination of continuous-DRX (CDRX) with near equiaxed grain sand discontinuous-DRX (DDRX) with some nucleated regions of ultrafine grains at trijunctions of grain boundaries by definition which is consistent for low-medium SFE alloys [14,15]. The SFE of similar HEAs including both single phase FCC and dual-phase HEAs were reported to be low-medium [3,12,16,17]. Although the distinction between CDRX and DDRX is not quite evident , the co-existence of both DRX were observed in duplex steels and is not uncommon [15]. The DRX led to increase in high angle grain boundaries (HAGB,$\theta > 15°$) which stands at ~70%% resulting in increase in dislocation storage [18]. In addition to that, such an effective grain refinement in dual-phase HEAs can also be attributed to particle stimulated nucleation effect of fragmented BCC phase and highly localized deformation at the heterophase interface of BCC and FCC during FSP [14].

The EBSD grain orientation distribution (GOS) map is a well-established technique to quantify the amount of DRX grains, deformed DRX grains and deformed grains which occurred during a thermomechanical processing of metallic materials. According to Allain-Bonasso, the GOS of a grain *i* can be written as follows[19,20]:

$$GOS(i) = \frac{1}{J(i)} \sum_{j} w_{ij} \qquad 6.1$$

,where *J(i)* is the number of pixels in the i^{th} grain, w_{ij} is the misorientation angle between the orientation of the pixel *j* and the average orientation of grain *i*. The fundamental idea behind GOS as a parameter for measuring DRX is that GOS measures the intragranular deformation and recrystallized grains are mostly strain-free whose GOS is below 2°. In the GOS< 2° map of Fig.6.3(c), the percentage of strain free latest DRXed grains stood at 45 %. The overall recrystallization for GOS< 5° which represents the deformed DRX and strain free (undeformed) DRX grains was more than 98% [19,20].

Therefore, the FSP of the as-cast alloy resulted in grain refinement which was driven by DDRX and strain induced phase transformation (TRIP effect) with FCC phase concentrated at the grain boundaries.

Table 6.1 EDS analysis of distribution of elements in BCC and FCC region

Element	Friction stir processed	
	BCC (at. %)	FCC (at. %)
Al	13.2	5
Co	18.8	18.2
Cr	17.4	21.8
Fe	30	38.2
Ni	20.4	15.4

6.3.2 Mechanical Response

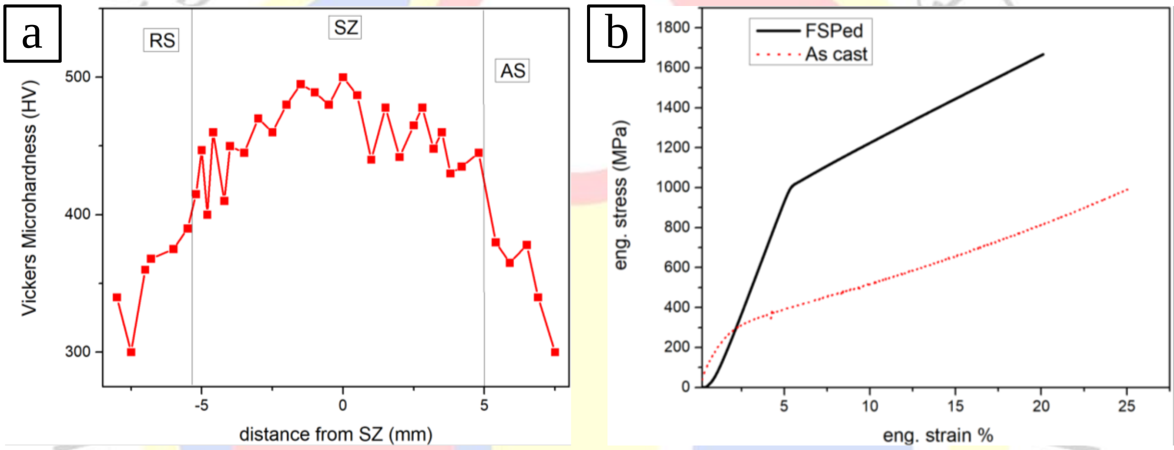

Figure 6.4 Variation of hardness across the processed area in the approaching side (AS), retreating side (RS) and stir zone (SZ) (b) engineering stress vs strain curve of as-cast condition and the friction stir processed condition

In Fig. 6.4(a) the variation of micro Vickers hardness of the FSP alloy across the advancing side (AS), stir zone and retreating side (RS) were displayed. The average hardness of the AS, SZ and RS were 359.9 HV, 467.8 HV and 346.5 HV respectively. In comparison to the as-cast alloy the hardness improved by more than three times for the SZ [1]. The lower hardness in the AS and RS side was due reduced TRIP effect with BCC percentage of less than 50 % and lathe like microstructure having average FCC lathe width of 20.2 µm as seen in Fig 6.5 (a) and (b).

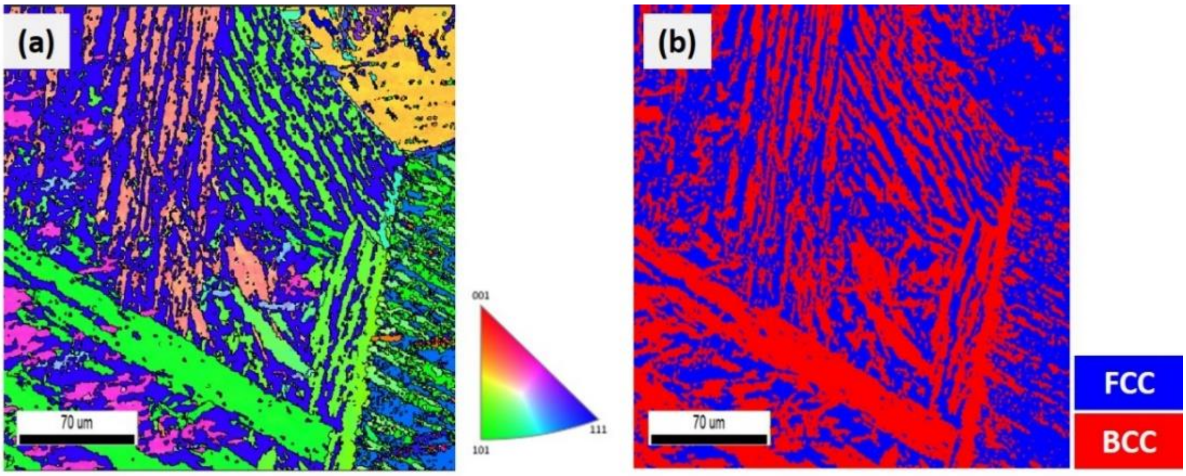

Figure 6.5 Lathe microstructure in the AS side (a) IPF (b) Phase map

While comparing the compressive strength of the as-cast alloy and the FSP alloy in Fig 6.4(b), the compressive yield strength increased from 250 $\pm$ 10 MPa to 996.10 $\pm$ 15 MPa. The percentage increase by 746 MPa which was close to 300 %. The hardness, yield strength and the overall increase in yield strength in terms relative percentage of FSP alloy was the highest for any single-phase FCC or dual-phase HEA of similar principal element system having single or multiple pass of FSP or cold rolled HEA undergoing FSP. The enhanced TRIP effect and harder BCC phase formed because of it in the FSP alloy compared to the HCP phase formed in the previous studies due to TRIP was one of the primary reasons for such a high increase in the hardness and strength [5,10,18,21–25].

Strengthening mechanisms

The primary strengthening mechanisms involved in a metallic alloy system can be categorized into four broad mechanisms: solid solution strengthening, grain boundary strengthening, dislocation hardening, and precipitation strengthening. The strength of a polycrystalline high entropy alloy can be cumulatively written as the summation of the above-mentioned strengthening mechanisms[1,26].

$$\sigma_{0.2} = \sigma_0 + \Delta\sigma_{ss} + \Delta\sigma_D + \Delta\sigma_{GB} + \Delta\sigma_{ppt} \quad 6.2$$

where σ_0 is the lattice friction stress, $\Delta\sigma_{ss}$ is the solid solution strengthening, $\Delta\sigma_D$ is the dislocation hardening, $\Delta\sigma_{GB}$ is the grain boundary contribution to strength, and $\Delta\sigma_{ppt}$ is the strength increment due to the presence of precipitation (which is negligible in this case). The lattice friction stress σ_0, which is an intrinsic property of a material, is calculated to be ~114 MPa applying the rule of mixture taking the elemental lattice friction stress values as given in the table below:

Table 6.2 Individual friction stress of the elements

Element	σ_0 (MPa)
Al	16
Co	10.3
Cr	454
Fe	100
Ni	22

(i) Solid solution strengthening

Although, HEAs which possess high solid solution strengthening inherently due to the difference in atomic size among its principal elements, it is rather difficult to distinguish the solute and the solvent in HEAs. The extent of the solubility of the large atoms in the alloy can be applied to determine the strength of solid solution strengthening. Since the BCC region is the primary phase in the FSP alloy, the solid solution strengthening based on the solubility of atoms in the BCC phase have been determined to estimate solid solution strengthening. For $Al_xCoCrFeNi$ system, solid solution strengthening is the lattice distortion based on different combinations of composition of the principal elements. Considering Al atoms as solute and the rest of the elements (Co, Cr, Fe, Ni) as the solvent, the Gypen L A formula can be used to determine the solid solution strengthening as given below [1,27]:

$$\Delta\sigma_{ss} = (\sum(k_i.\sqrt{c_i})^{\frac{1}{p}})^p \qquad 6.3$$

where k_i is the strengthening coefficient of solute i, c_i is the atomic percentage of solute i, and the value of p is ½. The average atomic percentage of Al in the BCC dendritic region for the FSP alloy was 13.2 %. The value of k_{Al} = 225MPa/ (at. %)$^{1/2}$ was adopted. Thus, the total solid solution strengthening in the case of FSP alloy was calculated as 82.14 MPa, respectively. Both atomic mismatch criteria and Gypen L A estimation predicted that solid solution strengthening in the FSP alloy was higher than the as-cast alloy where the reported solid solution strengthening in the as-cast alloy was 65.21 MPa [1]. The increase in solid solution strengthening was due to the dilution of secondary phase based spinodal decomposition based interdendritic region present in the as-cast alloy [28].

(ii) Grain boundary strengthening

The strength of a material is significantly influenced by the size of the grains in the processed alloy. The smaller the grain size, the greater is the number of grain boundaries that the dislocations have to overcome. The classic Hall-Petch equation relates the average size of the grains to the yield strength of the material.

$$\sigma_y = \sigma_0 + \frac{k_y}{d^{\frac{1}{2}}} \qquad 6.4$$

,where σ_0 is the lattice friction stress, k_y is the strengthening coefficient, and d is the grain diameter. The increase in yield strength owing to decrease in grain size can be further derived from the above equation for the FSP alloy compared to the as-cast condition as:

$$\Delta\sigma_{GB} = k_y(d_{FSP}^{-\frac{1}{2}} - d_{as-cast}^{-\frac{1}{2}}) \qquad 6.5$$

The average grain size of the SC alloy was found to be 12.45 µm, and that of the as-cast alloy was approximated at 1500 µm. The value of k_y for the FeMnCoCrNi system was adopted as 226 MPa.µm$^{1/2}$ for both the cases. Therefore, the difference in strength increment, due to grain boundary strengthening, between the FSP alloy and the as-cast alloy was evaluated as ~58.21 MPa.

(iii) Dislocation strengthening

The increase dislocation interactions impede their own mobility, which contributes to the hardening of the material. The Bailey-Hirsch formulates a relationship between dislocation density and dislocation hardening, as given below.

$$\Delta\sigma_D = M\alpha Gb\rho^{0.5} \qquad 6.6$$

where M is the Taylor factor, α is a correcting constant, the Burgers vector is given by b, G is the shear modulus and ρ is the total dislocation density which includes both statically stored dislocation (SSD) and geometrically necessary dislocations (GND) (in m^{-2}). Modifying Eq. 9 to find the strength contribution from GNDs the above equation can be modified as $\Delta\sigma_D = M\alpha Gb\rho_{GND}^{0.5}$.

The average GND value for the FSP alloy was derived from the EBSD data which estimated roughly at 1.6×10^{14} m^{-2}. The Burgers vector $b = \frac{\sqrt{3}}{2}a_{BCC} = 0.247nm$, the shear modulus value of G = 84 GPa was adopted, Taylor factor $M = 2.73$ for BCC phase and correction $\alpha = 1$ were taken for calculating the increase in strength due to GND and it was found to be 716.47 MPa. Therefore, the contribution of GND towards strengthening was the dominant contributor and the strengthening by SSDs can be neglected in the FSP alloy as seen in Table. 6.3 and the strengthening model was being able to accurately measure the strength after processing of the material.

Table 6.3 Strengthening contributions

$\Delta\sigma_{ss}$ (MPa)	$\Delta\sigma_{GB}$ (MPa)	$\Delta\sigma_{GND}$ (MPa)	σ_0 (MPa)	σ_{total} (MPa)	$\sigma_{experimenntal}$ (MPa)
82.14	63.21	716.4	114	975.82	996.1

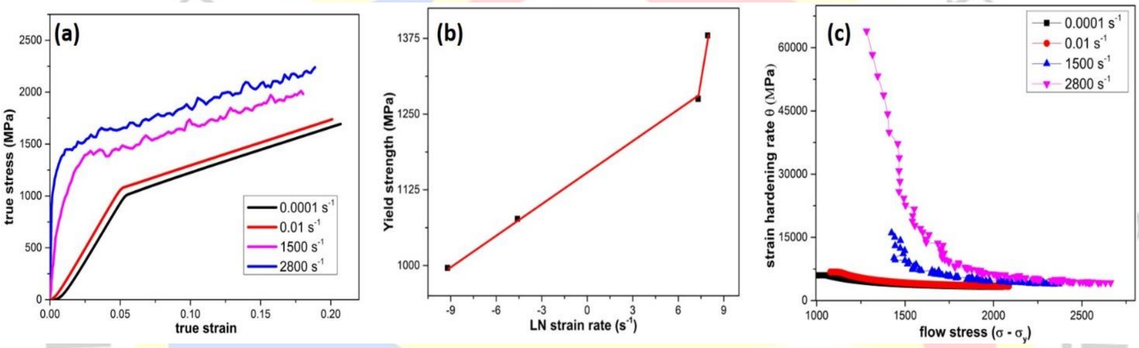

Figure 6.6 Stress strain plots from quasi static compression testing and dynamic deformation using SHPB (b) Varying yield strength with strain rates indicating two distinct regions (c) Kocks-Mecking (K-M) plots showing the variation of strain hardening rate (θ) with flow stress

The quasi static deformation and the high strain rate deformation of the as-cast alloy $Al_{0.65}CoCrFe_2Ni$ after friction stir processing were compared under varying strain rates in Fig. 6.6(a). Compared to the quasi static yield strength of the FSP alloy at 10^{-4} s^{-1}, the dynamic compression strength after SHPB tests were conducted increased by more than 350 MPa for strain rate 2800 s^{-1}. The serrated behavior of stress strain was observed at dynamic loading due to the complexities of wave interactions at such high velocity of deformation and substructure generation during deformation.

The strain rate hardening effect of the yielding stress is higher under dynamic conditions as shown in Fig. 6.6(b). The slope of the semi logarithmic strain rate plot in Fig 6(b) for FSP alloy, $\lambda = \frac{\partial \sigma}{\partial In\dot{\varepsilon}}$, was used to highlight the above statement. For the processed alloy in quasi static region (λ_I) was calculated as 35.11 and in the dynamic region the strain rate sensitivity (λ_{II}) is 168.94 which was significantly higher. The dislocation movement plays a significant role in the understanding of the deformation behaviour of alloys. The long range and short-range barriers resist the movement of the dislocations in the lattice and hinder plasticity. HEAs with solute size in the lattice impose short range barriers restricting dislocation movements under quasi static conditions. These short-range barriers can be overcome by reaching the thermal activation energy. For the lower slope in the quasi static region the thermal activation dislocation theory was employed with the help of thermal activation energy equation to understand the low strain rate sensitivity. The equation for thermal activation energy is given below:

$$\Delta G = kT\ (ln\frac{\dot{\varepsilon}_0}{\dot{\varepsilon}}) \qquad 6.7$$

where $\dot{\varepsilon}_0$ is the reference strain rate, $\dot{\varepsilon}$ is the strain rate, k is the Boltzmann constant, T is the temperature.

From Eq. 6.7, it is clear that higher the value of strain rate $\dot{\varepsilon}$, lower is the thermal activation energy needed to for ΔG to affect the dislocation and barrier negotiations. Further the activation volume related to the Gibbs free energy as $V^* = \frac{\partial\ \Delta G}{\partial\ \tau^*}$, where $\tau^*$is effective thermal shear factor and by Von Mises criteria, the normal stress, $\sigma = \frac{\tau}{\sqrt{3}}$, which finally translates into the following equation:

$$V^* = \sqrt{3}\ k_b T \frac{\partial\ ln\dot{\varepsilon}}{\partial\sigma} = \sqrt{3}\ k_b T \frac{\partial\ ln\sigma}{m\ \partial\sigma} \qquad 6.8$$

, where m is the logarithmic SRS, m= $\frac{\partial\ ln\sigma}{\partial\ In\dot{\varepsilon}}$.

Consequently, the activation volume for HEAs lie between (1-100 b^3) which is relatively much smaller than conventional FCC metals such as Cu, Cu-Zn, are attributed to high friction stress from short range order and solid solution pinning effect at high strain rate. This might have contributed to high dislocation interactions resulting in substructures formation in HEAs under such loading.

Again, at high strain rate loading behaviour of materials, the viscoelastic effect becomes dominant and significant enough to sufficiently explain the deformation mechanism and the SRS ay dynamic loading because of the instantaneous increase in the temperature at high strain rate tend to reduce the activation energy (ΔG) significantly and the transient nature of dynamic deformation do not entirely utilize the thermal activation energy.

The Orowan model is frequently used to highlight the plastic behaviour of the metals under shock wave loading which can be written as given below:

$$\frac{d\varepsilon}{dt} = \frac{1}{m}.\rho b\vartheta = \frac{1}{m}.\frac{d\rho}{dt}b\Delta x_d \quad 6.9$$

where $\frac{d\varepsilon}{dt}$ is the compressive strain rate; m is the orientation factor, b is the Burgers vector, ρ is the mobile dislocation density, ϑ is the dislocation velocity and Δx_d is the separation between dislocations. From Eq. 6.9 it can be inferred that higher strain rate translates into faster movement of dislocation which eventually approaches shear wave velocity. The dislocation velocity can thereby be determined by the shear stresses (τ) and the frictional forces (σ_f) involved during the loading as given by the equation below.

$$\sigma_f = n\vartheta = b\tau \quad 6.10$$

where n is the drag coefficient. The above equation Eq. 6.10 is consistent with the relativity theory given by the equation below:

$$n = n_0 /(1 - \frac{\vartheta^2}{c_s^2}) \qquad 6.11$$

, where n_0 is the drag coefficient at rest. This effect of viscosity is the concept of phonon drag which becomes operative in the high strain rate deformation leading to a significant rise in the yield stresses.

As discussed, the high lattice distortions in HEAs also gives rise to local elastic stress field and the interactions between the stress field of the elastic field and the dislocation field impede the dislocation movement. The Taylor formula of dislocation movement therefore expalins the higher strength and strain hardening rate at high strain rates as given by the formula below:

$$\vartheta = A\sigma^m \qquad 6.12$$

, where A and m are constants.

The overall strain rate sensitivity (SRS), m= $\frac{\partial\, ln\sigma}{\partial\, In\dot{\varepsilon}}$, at a strain of 0.02 in the alloy taking both quasi statically deformed and dynamic deformed conditions of the FSPed alloy was calculated to be 0.019 which is lower than the as-cast alloy SRS of 0.035. The strain rate sensitivity of the quasi static loading (m_s) was 0.016 and the dynamic loading (m_d) was 0.125.

In general, the strain rate sensitivity depends on the temperature dependent strength contributions which influences slip and dislocation activities. The microstructure of a material largely determines the dislocation motion and the SRS of the material is sensitive to it. However, the dislocation hindrances are caused by both long-range obstacles (athermal) and short-range obstacles (temperature dependent). The dominance of the above two factors eventually impacts the value of SRS. The MTS model formulates the total stress for deformation as:

$$\sigma = \sigma_{thermal} + \sigma_{athermal} \tag{6.13}$$

The thermal factors of stress are contributed from the frictional stress σ_{fs}, Peierls Nabarro (σ_{P-N}) stress and the solid solution strengthening (σ_{ss}). The higher values of these factors increase the SRS values of metal alloy systems. The athermal barriers in the form of grain boundaries (σ_{GB}), dislocation density (σ_{DIS}) and twin boundaries (σ_{TW}) (absent in this case) adversely impact the strain rate on the material. The grain refinement after friction stir processing created significant athermal factors in the form of grain boundaries which led to the decrease of SRS compared to the as-cast alloy. While comparing the SRS with cold rolled HEAs it was observed that the SRS for pure cold rolled single-phase FCC-based HEAs $Al_{0.1}CoCrFeNi$ and $Al_{0.3}CoCrFeNi$ were 0.009 and 0.006 after grain refinement from 0.017 and 0.063 in the as-cast and homogenized conditions respectively. However, such single phase HEAs after being cold rolled exhibited only small improvements in their overall strengths. For thermo-mechanically processed single phase FCC HEAs, improved strain hardening properties with high SRS retention was seen in $Al_{0.3}CoCrFeNi$ after four step precipitation hardened coherent nano-sized L12 precipitate were introduced where SRS displayed was 0.054 [29,30]. For similar four stages (homogenised, cold rolled, solutionised and annealed) thermo-mechanically processed $Al_{0.7}CoCrFeNi$ hypo eutectic (FCC+BCC) HEA with lamellar system also exhibited good SRS retention with a value of 0.018 [31,32]. The nano-scale size of the precipitates acted like short range thermally activated barriers in the above two cases which helped in the maintaining the SRS. However, except for one case of thermomechanical processing conditions $Al_{0.7}CoCrFeNi$ which presented similar strength under quasi static loading, all cases possessed lower strength and required multiple steps.

The Kocks-Mecking (K-M) plot comprising of strain hardening rate ($\theta = \frac{d\sigma}{d\epsilon}$) vs flow stress ($\sigma - \sigma_y$) was represented in Fig.6.6(c). The K-M consisted of three stages of strain hardening rate in all the cases of loading. Stage A is a rapidly decreasing strain hardening transition period from elastic to plastic with stress, stage B is the gradually decreasing strain hardening rate with stress which is usually governed by dislocation slip and finally the last stage C where the strain hardening rate becomes constant with further deformation was due to dynamic recovery. It was observed that the dynamic strain hardening rate in stage A ended at higher values than quasi static region because of phonon drag as mentioned in Eq. 6.9-12. In the second stage of strain hardening rate, the slope of strain hardening rate at high strain rate ($\theta = 4803.57$ MPa at 2800 s^{-1}) was higher than that under quasi static deformation ($\theta = 4593.12$ MPa at 10^{-4} s^{-1}) because of the lower time for dynamic recovery to occur in case of high strain rate compression. However, the difference in strain hardening rate θ between the quasi static and the high strain rate loading conditions were smaller than that in case of as-cast conditions due to lower presence of better strain hardening FCC phase in the FSPed alloy. In addition, the various substructure evolution of the microstructure which were associated with dynamic loading could be reasons for such lower rate of decrease of strain hardening rate in stage B. Slip remained the dominant deformation mechanism at quasi static compression and compressive high strain rate loadings. To further investigate the appropriate reasons, the microstructural analysis after deformation are discussed in the next section.

6.3.3 Deformation Mechanisms

The deformation mechanisms of the FSP alloy after compression under quasi static loading and high strain rate loading from the perspective of misorientation study in the microstructure and substructure formation after respective deformations are discussed in this section. The unindexed section of the EBSD maps are due to heavy deformation of the lattice at certain sections.

Quasi Static Deformation Mechanisms

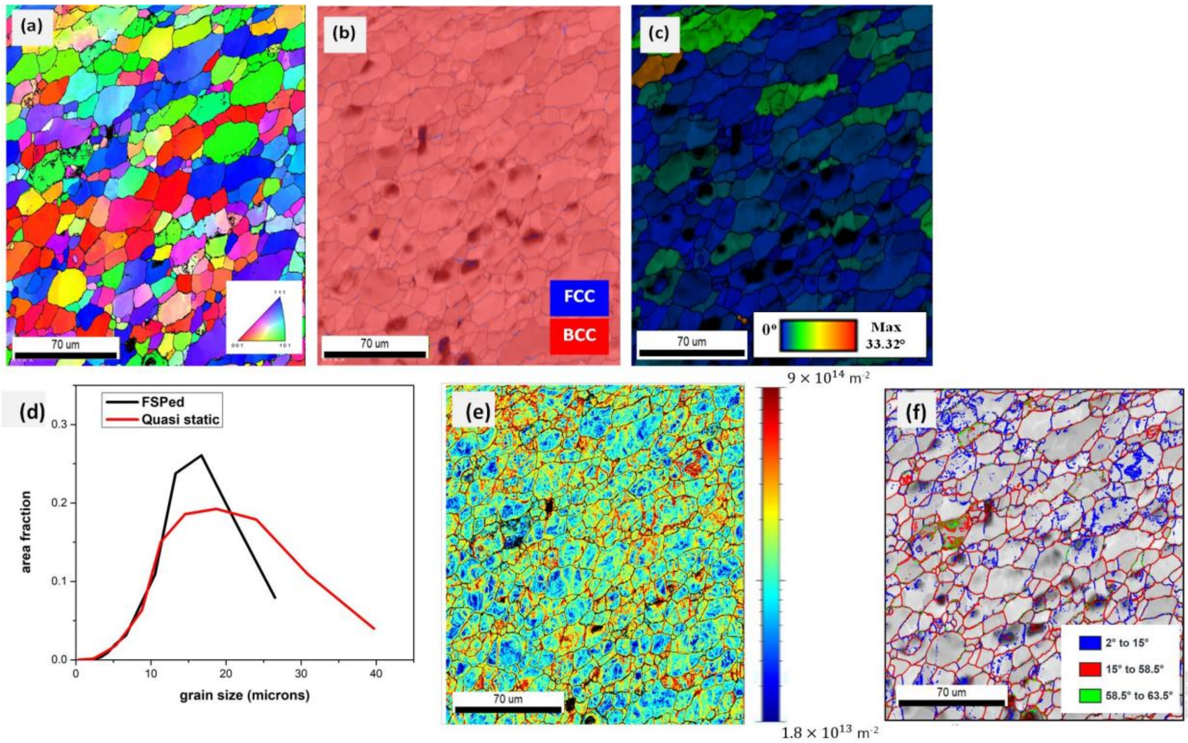

Figure 6.7 EBSD maps of quasi statically deformed sample at strain rate of $10^{-4}s^{-1}$ (a) IPF (b) phase map (c) GOS (d) grain size distribution plot (e) GND map (e) boundary map

The quasi static deformation at strain rate of $10^{-4}s^{-1}$ on the FSP alloy was governed by multiple mechanisms. The inverse pole figure (IPF), the phase map, the GOS map, geometrically necessary dislocation (GND) map and the boundary map along with the misorientation distribution map shown in Fig.6.7 were used to understand the deformation mechanism involved. The quasi static compression led to elongation of grains and heavy lattice deformation at certain regions as well as unindexed dark regions as can be seen in Fig. 6.7. Deformation induced phase transformation remain as one of the major deformation mechanisms during compression (Fig. 6.7(b)). The BCC phase further increased by 3% at a strain ε~18% and the total BCC phase after compression stood at 95%. The increase in the hard BCC phase from the FCC phase gives rise to strain induced phase transformation-based hardening [7,23,33]. The GOS map in Fig 6.7(c) with a maximum value of 33.32 clearly shows large intragranular lattice rotation. In fact, the heavily strained grains led to a modest increase in the average grain size (18.32 μm) compared to the FSP alloy (15.45 μm) as can be ascertained from the comparative grain size distribution plot of Fig. 6.7(d) which was broader than the undeformed sample. The geometric hardening due to lattice re-orientation is therefore another contributor to the strain hardening behaviour. The heavy deformation resulted in large generation of GND of Fig. 6.7(d) (avg. $\rho_{GND} = 2.1 \times 10^{14}$ m^{-2}) as energy storage regions which is an increase from the undeformed condition (avg. $\rho_{GND} = 1.6 \times 10^{14}$ m^{-2}). The boundary maps of the quasi statically compressed sample in Fig. 6.7(e) showed that there was an overall increase in the formation of subgrain boundaries (SGBs) or substructure which might eventually form SGBs having misorientation less than 15°. The SGBs rose to 38.6% from 24.8% after deformation which is triggered by higher rate of dynamic recovery and initial existence of high density of HAGBs and low annihilation of dislocations [34,35].

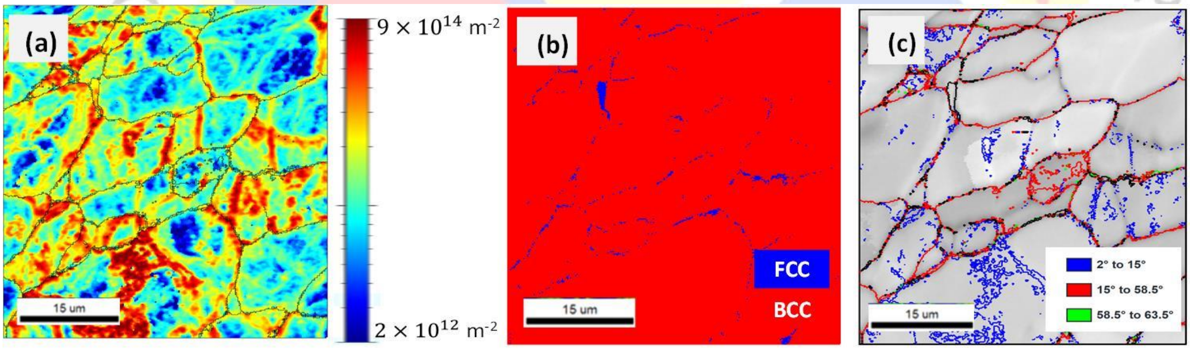

Figure 6.8 Magnified EBSD images of FSP samples deformed under quasi static loadingat strain rate 10^{-4} s^{-1} (a) GND map (b) phase map (c) boundary Map

A closer view of the combining the GND map, phase map and boundary map shows that the hotspots of GND occurs around the grain boundaries where interphase FCC phase is concentrated and inside the heavily deformed grains containing SGBs (avg. gnd ~10^{15}) as seen Fig. 6.8. The high GNDs at grain boundaries proves that the FCC phase concentrated at the grain boundaries in the undeformed FSP alloy were heavily strained to cause deformation induced phase transformations on deformation under quasi static compression which creates a synergy of strain hardening rate and ductility [7,36,37]. The subgrain boundaries formed creates barriers for unit dislocation to continuously overcome thereby increasing both ductility and strain hardening [34,35]. Negligible percentage of deformation twins like structures (misorientation close to 60°) were also present. The decrease in the overall twin formation of the FSP alloy compared to its as-cast condition was because the SFE of a material and hence its critical stress for twin formation increases with increase in with reduction of grain size and BCC phase have higher SFE than FCC phase. In addition, the microstructural homogeneity after FSP with the removal of dendritic phase also reduces the possibility of twin formation [7,23]. Since after FSP, there was reduction of grain size from ~2000 μm to ~15.45 μm and an increase in the percentage of BCC phase from ~15% to 92%, the SFE of the FSP alloy increased and led to lower twin formation on deformation.

Therefore, the quasi static deformation mechanism of FSP alloy involved deformation induced effect, phase boundary and subgrain boundary-based strain hardening and traces of deformation twin like structures.

High Strain Rate deformation

The IPF, phase map, GOS map, grain boundary distribution plot, GND map and misorientation boundary map of the deformed FSP alloy under high strain rate loading are shown in Fig. 6.9. The IPF in Fig. 6.9(a) clearly shows that there was refinement of grains after deformation in the FSP alloy. The overall average GOS and the maximum GOS were higher compared to quasi static deformation because of large number of elongated grains which were heavily deformed and were on the verge of breaking into new grains. The average grain size reduced to 5.4 μm from 15.45 μm in the undeformed sample. This indicated the possibility of DRX after deformation at high strain rate loading. The combination of equiaxed grains with some elongated grains clearly established the driving mechanism of DRX to be

CRDX and its coexisting geometric DRX (GDRX) [15,38,39]. There was a more pronounced stress induced phase transformation effect compared to the deformation under quasi static compression. The overall increase in strain induced BCC phase was 6% with the final percentage of BCC phase in the sample close to 98% as analysed from phase map in Fig.6.9(b). As discussed, the phonon drag effect cause higher dislocation pileup which causing high strain generation at grain boundaries where the FCC phase were concentrated due geometrical discontinuity. This large straining at the grain boundaries could have been reasons for higher deformation induced phase transformation effect at high strain rate loadings compared to quasi static compression. The deformation induced phase transformation effect is excellent strain absorbing mechanism which help the FSP alloy to increase the strengthen and also improve the ductility of the material [7,23,36,40]. The overall GND increased to avg. $\rho_{GND} = 2.2 \times 10^{14}$ m^{-2} from avg. $\rho_{GND} = 1.6 \times 10^{14}$ m^{-2} which an indication of the increase in strain storage creation of the FSP alloy under dynamic loading [35]. The boundary maps clearly show a rise in the fraction percentage of HAGB (~75%) compared to undeformed FSP (~70%) alloy due heavy intergranular lattice rotation causing grain refinement in Fig. 6.9(e).

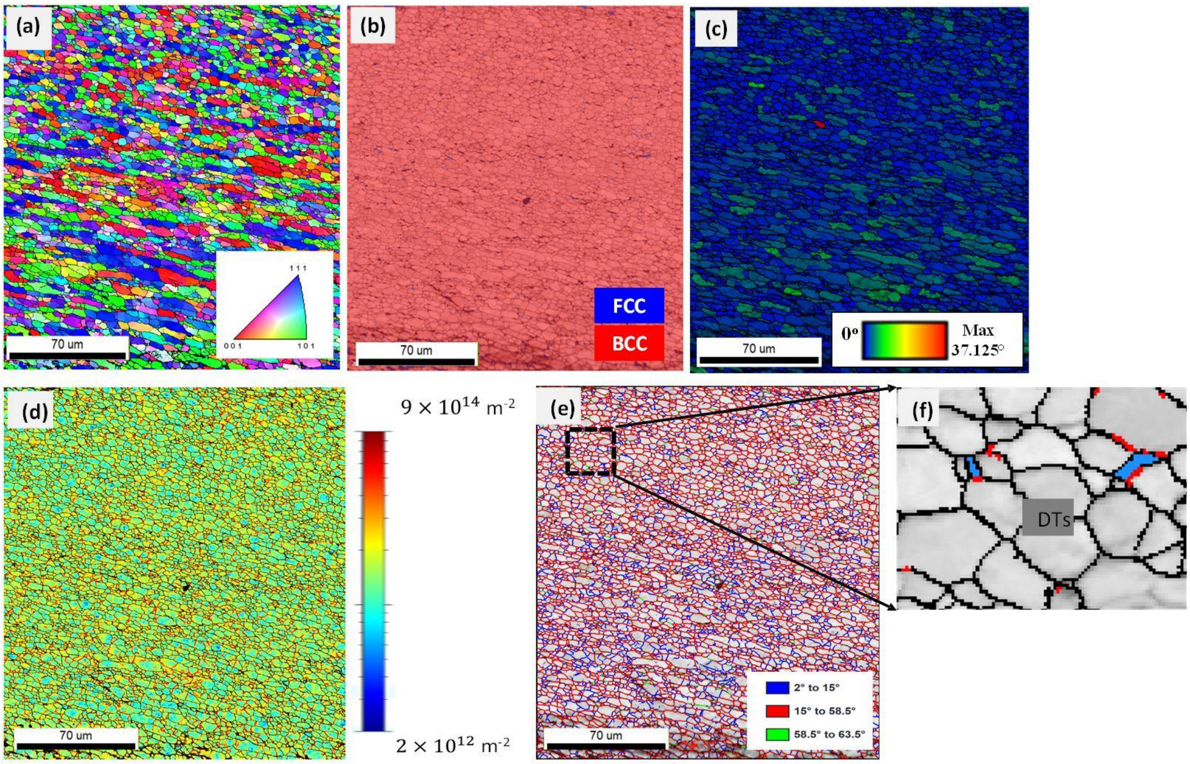

Figure 6.9 EBSD maps of deformed FSP samples at high strain rate (a) IPF (b) phase map (c) GOS (d) GND map (e) boundary map (f) twins area map

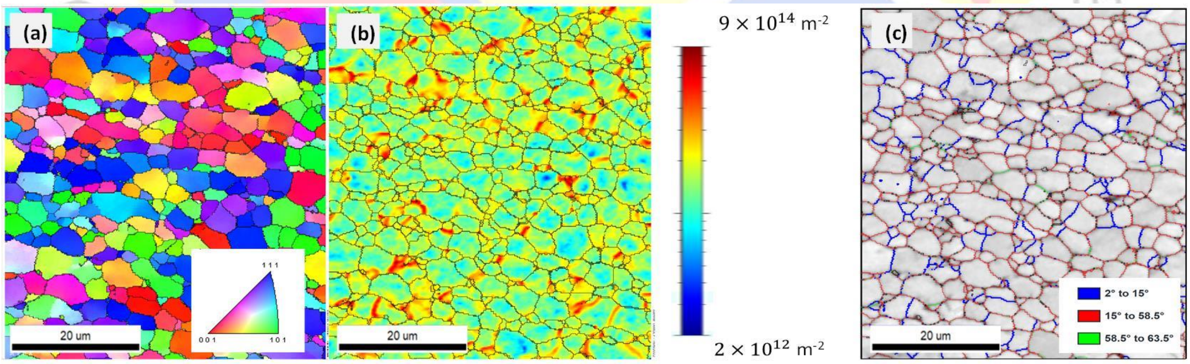

Figure 6.10 Magnified EBSD images of FSP samples deformed under high strain rate loading (a) IPF map (b) GND (c) boundary Map

While analysis the magnified IPF, GND map and boundary map in Fig. 6.10, it was quite evident that there was large dislocation accumulation at the HAGBs (avg. $\rho_{GND} = 2.4 \times 10^{14}$ m^{-2}). The rise in the fraction of HAGBs and number of HAGBs increase dislocation barrier which in turn improves the strain hardening of the sample. However, the higher stress concentration in the form of GNDs were located at the planar deformation bands (avg. $\rho_{GND} = 5.5 \times 10^{14}$ m^{-2}) formed inside grains (misorientation less than 15°) as analysed from Fig. 6.10(a) and(b). These deformation bands act as excellent barriers to hinder dislocation motion which enhances the strain hardening nature of the alloy[34,35,41]. Distinct deformation twins were also observed in the dynamically deformed samples as seen in Fig. 6.9(f). In fact, there was a modest increase in the fraction of twin formation in case under high strain rate deformation which was due to the viscous drag effect associated under dynamic loading. The formation of twins creates additional boundaries and reduces the dislocation free paths which adds to the increase of strain hardening rate efficiently [3,16,42].

Thus, the deformation of the FSP sample at high strain rate led to higher deformation induced phase transformation effect, intergranular lattice rotation in the form of increase HAGBs, formation of planar deformation bands and twins.

6.4 Summary

Friction stir processing (FSP) of as-cast $Al_{0.65}CoCrFe_2Ni$ conducted resulted in the TRIP effect with a high rise in BCC phase and grain refinement of the alloy. The microstructural and mechanical studies exercised on the FSP alloy can be summarized as follows:

(a) The as-cast sample after friction stir processing resulted in the reduction of grain size from ~10^3 µm to average grain size of 15.45 µm.

(b) The as-cast alloy after friction stir processing exhibited stress induced phase transformation effect leading to significant increase in the BCC phase from ~15% to ~92%.

(c) The average hardness increased from 128 HV in BCC phase of the as-cast sample to 467.5 HV in the stir zone nearly four times under quasi static compression compared to the as-cast condition.

(d) The yield strength under compressive quasi static loading after friction stir processing of the as-cast alloy increased nearly four times.

(e) The FSP alloy exhibited lower strain rate sensitivity (SRS) compared to as-cast (IM) alloy due to dominant smaller grain size, high dislocation strengthening, increase in BCC phase and increase in stacking fault energy.

(f) The strain hardening rate of the FSP alloy was higher at both quasi static and dynamic loadings compared to the as-cast (IM) alloy due to lower grain size and higher dislocation strengthening.

(g) The deformation of the FSP alloy under quasi static deformation was characterised by moderate deformation induced phase transformation effect, subgrain boundary strengthening and stress concentration at phase boundary.

(h) Under dynamic loading the FSP alloy deformation resulted in DRX, deformation induced phase transformation effect, deformation bands and deformation twins.

This study has proved that FSP can be an rapid effective thermo-mechanical processing technique that can be employed to high entropy alloys to enhance the mechanical properties in a simple one pass scalable way.

References

[1] S. Tamuly, S. Dixit, B. Kombaiah, P. Khanikar, Strengthening Mechanisms and Deformation Behavior of Industrially-Cast and Lab-Cast Dual-Phase High Entropy Alloy, Met. Mater. Int. (2022). https://doi.org/10.1007/s12540-022-01211-x.

[2] G.C. Soares, M. Patnamsetty, P. Peura, M. Hokka, Effects of Adiabatic Heating and Strain Rate on the Dynamic Response of a CoCrFeMnNi High-Entropy Alloy, J. Dyn. Behav. Mater. 5 (2019) 320–330. https://doi.org/10.1007/s40870-019-00215-w.

[3] L. Wang, J.W. Qiao, S.G. Ma, Z.M. Jiao, T.W. Zhang, G. Chen, D. Zhao, Y. Zhang, Z.H. Wang, Mechanical response and deformation behavior of Al0.6CoCrFeNi high-entropy alloys upon dynamic loading, Mater. Sci. Eng. A. 727 (2018) 208–213. https://doi.org/10.1016/j.msea.2018.05.001.

[4] Website, www.atex-software.eu, (n.d.). http://www.atex-software.eu/ (accessed December 25, 2021).

[5] A. Sittiho, M. Bhattacharyya, J. Graves, S.S. Nene, R.S. Mishra, I. Charit, Friction stir processing of a high entropy alloy Fe42Co10Cr15Mn28Si5 with transformative characteristics: Microstructure and mechanical properties, Mater. Today Commun. 28 (2021) 102635. https://doi.org/10.1016/j.mtcomm.2021.102635.

[6] Z. Li, K.G. Pradeep, Y. Deng, D. Raabe, C.C. Tasan, Metastable high-entropy dual-phase alloys overcome the strength-ductility trade-off, Nature. 534 (2016) 227–230. https://doi.org/10.1038/nature17981.

[7] Z. Li, C.C. Tasan, K.G. Pradeep, D. Raabe, A TRIP-assisted dual-phase high-entropy alloy: Grain size and phase fraction effects on deformation behavior, Acta Mater. 131 (2017) 323–335. https://doi.org/10.1016/j.actamat.2017.03.069.

[8] R.S. Mishra, S.S. Nene, Some Unique Aspects of Mechanical Behavior of Metastable Transformative High Entropy Alloys, Metall. Mater. Trans. A Phys. Metall. Mater. Sci. 52 (2021) 889–896. https://doi.org/10.1007/s11661-021-06138-3.

[9] S.S. Nene, K. Liu, M. Frank, R.S. Mishra, R.E. Brennan, K.C. Cho, Z. Li, D. Raabe, Enhanced strength and ductility in a friction stir processing engineered dual phase high entropy alloy, Sci. Rep. 7 (2017) 1–7. https://doi.org/10.1038/s41598-017-16509-9.

[10] S.S. Nene, M. Frank, K. Liu, R.S. Mishra, B.A. McWilliams, K.C. Cho, Extremely high strength and work hardening ability in a metastable high entropy alloy, Sci. Rep. 8 (2018) 1–8. https://doi.org/10.1038/s41598-018-28383-0.

[11] T. Wang, M. Komarasamy, S. Shukla, R.S. Mishra, Simultaneous enhancement of strength and ductility in an AlCoCrFeNi2.1 eutectic high-entropy alloy via friction stir processing, J. Alloys Compd. 766

(2018) 312–317. https://doi.org/10.1016/j.jallcom.2018.06.337.

[12] N. Kumar, Q. Ying, X. Nie, R.S. Mishra, Z. Tang, P.K. Liaw, R.E. Brennan, K.J. Doherty, K.C. Cho, High strain-rate compressive deformation behavior of the Al0.1CrFeCoNi high entropy alloy, Mater. Des. 86 (2015) 598–602. https://doi.org/10.1016/j.matdes.2015.07.161.

[13] L. Wang, J.W. Qiao, S.G. Ma, Z.M. Jiao, T.W. Zhang, G. Chen, D. Zhao, Y. Zhang, Z.H. Wang, Mechanical response and deformation behavior of Al0.6CoCrFeNi high-entropy alloys upon dynamic loading, Mater. Sci. Eng. A. (2018). https://doi.org/10.1016/j.msea.2018.05.001.

[14] Z. Savaedi, R. Motallebi, H. Mirzadeh, A review of hot deformation behavior and constitutive models to predict flow stress of high-entropy alloys, J. Alloys Compd. 903 (2022) 163964. https://doi.org/10.1016/j.jallcom.2022.163964.

[15] K. Huang, R.E. Logé, A review of dynamic recrystallization phenomena in metallic materials, Mater. Des. 111 (2016) 548–574. https://doi.org/10.1016/j.matdes.2016.09.012.

[16] Z. Li, S. Zhao, H. Diao, P.K. Liaw, M.A. Meyers, High-velocity deformation of Al0.3 CoCrFeNi high-entropy alloy: Remarkable resistance to shear failure, Sci. Rep. 7 (2017) 1–8. https://doi.org/10.1038/srep42742.

[17] J.M. Park, J. Moon, J.W. Bae, M.J. Jang, J. Park, S. Lee, H.S. Kim, Strain rate effects of dynamic compressive deformation on mechanical properties and microstructure of CoCrFeMnNi high-entropy alloy, Mater. Sci. Eng. A. 719 (2018) 155–163. https://doi.org/10.1016/j.msea.2018.02.031.

[18] M. Komarasamy, N. Kumar, Z. Tang, R.S. Mishra, P.K. Liaw, Effect of microstructure on the deformation mechanism of friction stir-processed Al0.1CoCrFeNi high entropy alloy, Mater. Res. Lett. 3 (2014) 30–34. https://doi.org/10.1080/21663831.2014.958586.

[19] A. Hadadzadeh, F. Mokdad, M.A. Wells, D.L. Chen, A new grain orientation spread approach to analyze the dynamic recrystallization behavior of a cast-homogenized Mg-Zn-Zr alloy using electron backscattered diffraction, Mater. Sci. Eng. A. (2018). https://doi.org/10.1016/j.msea.2017.10.062.

[20] A. Ayad, M. Ramoul, A.D. Rollett, F. Wagner, Quantifying primary recrystallization from EBSD maps of partially recrystallized states of an IF steel, Mater. Charact. 171 (2021) 110773. https://doi.org/10.1016/j.matchar.2020.110773.

[21] N. Kumar, M. Komarasamy, P. Nelaturu, Z. Tang, P.K. Liaw, R.S. Mishra, Friction stir processing of a high entropy alloy Al0.1CoCrFeNi, Jom. 67 (2015) 1007–1013. https://doi.org/10.1007/s11837-015-1385-9.

[22] J. Zhang, R. Fu, Y. Li, Y. Lei, L. Guo, H. Lv, J. Yang, Synergistic enhancement in strength and ductility of nitrogen-alloyed CoCrFeMnNi high-entropy alloys via multi-pass friction stir processing, J. Alloys Compd. 927 (2022) 167015. https://doi.org/10.1016/j.jallcom.2022.167015.

[23] R.S. Haridas, P. Agrawal, S. Thapliyal, S. Yadav, R.S. Mishra, B.A. McWilliams, K.C. Cho, Strain rate

sensitive microstructural evolution in a TRIP assisted high entropy alloy: Experiments, microstructure and modeling, Mech. Mater. 156 (2021) 103798. https://doi.org/10.1016/j.mechmat.2021.103798.

[24] K. Liu, S.S. Nene, M. Frank, S. Sinha, R.S. Mishra, Metastability-assisted fatigue behavior in a friction stir processed dual-phase high entropy alloy, Mater. Res. Lett. 6 (2018) 613–619. https://doi.org/10.1080/21663831.2018.1523240.

[25] S. Sinha, S.S. Nene, M. Frank, K. Liu, R.A. Lebensohn, R.S. Mishra, Deformation mechanisms and ductile fracture characteristics of a friction stir processed transformative high entropy alloy, Acta Mater. 184 (2020) 164–178. https://doi.org/10.1016/j.actamat.2019.11.056.

[26] J.Y. He, H. Wang, H.L. Huang, X.D. Xu, M.W. Chen, Y. Wu, X.J. Liu, T.G. Nieh, K. An, Z.P. Lu, A precipitation-hardened high-entropy alloy with outstanding tensile properties, Acta Mater. 102 (2016) 187–196. https://doi.org/10.1016/j.actamat.2015.08.076.

[27] Q. Tian, G. Zhang, K. Yin, W. Wang, W. Cheng, Y. Wang, The strengthening effects of relatively lightweight AlCoCrFeNi high entropy alloy, Mater. Charact. 151 (2019) 302–309. https://doi.org/10.1016/j.matchar.2019.03.006.

[28] X. Liu, Y. Wu, Y. Wang, J. Chen, R. Bai, L. Gao, Z. Xu, W.Y. Wang, C. Tan, X. Hui, Enhanced dynamic deformability and strengthening effect via twinning and microbanding in high density NiCoFeCrMoW high-entropy alloys, J. Mater. Sci. Technol. 127 (2022) 164–176. https://doi.org/10.1016/j.jmst.2022.02.055.

[29] S. Gangireddy, L. Kaimiao, B. Gwalani, R. Mishra, Microstructural dependence of strain rate sensitivity in thermomechanically processed Al0.1CoCrFeNi high entropy alloy, Mater. Sci. Eng. A. 727 (2018) 148–159. https://doi.org/10.1016/j.msea.2018.04.108.

[30] S. Gangireddy, B. Gwalani, K. Liu, R. Banerjee, R.S. Mishra, Microstructures with extraordinary dynamic work hardening and strain rate sensitivity in Al0.3CoCrFeNi high entropy alloy, Mater. Sci. Eng. A. 734 (2018) 42–50. https://doi.org/10.1016/j.msea.2018.07.088.

[31] S. Gangireddy, B. Gwalani, R. Banerjee, R.S. Mishra, High Strain Rate Response of Al0.7CoCrFeNi High Entropy Alloy: Dynamic Strength Over 2 GPa from Thermomechanical Processing and Hierarchical Microstructure, J. Dyn. Behav. Mater. 5 (2019) 1–7. https://doi.org/10.1007/s40870-018-00178-4.

[32] S. Gangireddy, B. Gwalani, V. Soni, R. Banerjee, R.S. Mishra, Contrasting mechanical behavior in precipitation hardenable AlXCoCrFeNi high entropy alloy microstructures: Single phase FCC vs. dual phase FCC-BCC, Mater. Sci. Eng. A. 739 (2019) 158–166. https://doi.org/10.1016/j.msea.2018.10.021.

[33] S. Gupta, P. Agrawal, S.S. Nene, R.S. Mishra, Friction stir welding of γ-fcc dominated metastable high entropy alloy: Microstructural evolution and strength, Scr. Mater. 204 (2021) 114161. https://doi.org/10.1016/j.scriptamat.2021.114161.

[34] F.H. Dalla Torre, E. V. Pereloma, C.H.J. Davies, Strain hardening behaviour and deformation kinetics

of Cu deformed by equal channel angular extrusion from 1 to 16 passes, Acta Mater. 54 (2006) 1135–1146. https://doi.org/10.1016/j.actamat.2005.10.041.

[35] X. Gao, Y. Lu, J. Liu, J. Wang, T. Wang, Y. Zhao, Extraordinary ductility and strain hardening of Cr26Mn20Fe20Co20Ni14 TWIP high-entropy alloy by cooperative planar slipping and twinning, Materialia. 8 (2019) 100485. https://doi.org/10.1016/j.mtla.2019.100485.

[36] S. Bhowmik, J. Zhang, S.C. Vogel, S.S. Nene, R.S. Mishra, B.A. McWilliams, M. Knezevic, Effects of plasticity-induced martensitic transformation and grain refinement on the evolution of microstructure and mechanical properties of a metastable high entropy alloy, J. Alloys Compd. 891 (2022) 161871. https://doi.org/10.1016/j.jallcom.2021.161871.

[37] J. Li, Q. Fang, B. Liu, Y. Liu, Transformation induced softening and plasticity in high entropy alloys, Acta Mater. 147 (2018) 35–41. https://doi.org/10.1016/j.actamat.2018.01.002.

[38] C. Zhang, K. Feng, H. Kokawa, Z. Li, K. Chen, Microstructure transition and mechanical properties of friction stir processed CoCrFeMnNi high entropy alloy fabricated by laser powder bed fusion, Mater. Sci. Eng. A. 845 (2022) 143254. https://doi.org/10.1016/j.msea.2022.143254.

[39] Y. Hu, Y. Niu, Y. Zhao, W. Yang, X. Ma, J. Li, Friction stir welding of CoCrNi medium-entropy alloy: Recrystallization behaviour and strengthening mechanism, Mater. Sci. Eng. A. 848 (2022) 143361. https://doi.org/10.1016/j.msea.2022.143361.

[40] H. Jeong, N. Park, Materials Science & Engineering A TWIP and TRIP-associated mechanical behaviors of Fe x (CoCrMnNi) 100-x medium-entropy ferrous alloys, 782 (2020).

[41] Q. Wang, T. Gao, H. Du, Q. Hu, Q. Chen, Z. Fan, L. Zeng, X. Liu, Hot compression behaviors and microstructure evolutions of a cast dual-phase NiCoFeCrAl0.7 high-entropy alloy, Intermetallics. 138 (2021) 107314. https://doi.org/10.1016/j.intermet.2021.107314.

[42] N. Kumar, Q. Ying, X. Nie, R.S. Mishra, Z. Tang, P.K. Liaw, R.E. Brennan, K.J. Doherty, K.C. Cho, High strain-rate compressive deformation behavior of the Al0.1CrFeCoNi high entropy alloy, Mater. Des. 86 (2015) 598–602. https://doi.org/10.1016/j.matdes.2015.07.161.

Chapter 7 Conclusions and Future Work

7.1 Background

Processing of high entropy alloys at large scale and appropriate strengthening of these alloys can address major shortcomings in the alloy industry for structural and high strain rate applications. However, study on high entropy alloys under high strain rate loading have gained attention only in recent times. Interestingly, the high entropy alloys have shown excellent strain rate hardening and strain hardening properties under high strain rate loading but dual-phase high entropy alloys with balanced strength and ductility under dynamic loading conditions are not extensively studied. The current thesis work attempts to contribute fundamental knowledge towards processing a dual-phase high entropy alloy, improving its mechanical properties and analysing the deformation behaviour of the alloy under high strain rate loading. In pursuit of this primary aim, the following major aspects are covered.

(a) Development of a dual-phase high entropy alloy $Al_{0.65}CoCrFe_2Ni$ consisting of FCC and BCC phases at a large-scale industrial environment.

(b) The effects of cooling rate of solidification on the mechanical properties and deformation behaviour of the alloy under quasi-static loading were investigated.

(c) Understanding of the high strain rate deformation response of the as-cast industrially melted alloy.

(d) Investigation of the high strain rate deformation behaviour of the rapidly cooled suction-cast alloy.

(e) Improvement of the mechanical properties of the as-cast industrially melted alloy by friction stir processing and investigation of its deformation behaviour under quasi-static and high strain rate loading.

7.2 Conclusions

This thesis work contributes several key findings related to alloy processing, microstructural evolution, mechanical properties and deformation behaviour under several strain rate regimes. The major conclusions of the thesis work are highlighted below.

(a) Both as-cast alloy and suction-cast alloy samples possessed similar percentages of FCC and BCC phases. However, higher cooling rate of solidification of the suction-cast alloy resulted in the increase in strength and hardness compared to as-cast alloy due to finer grains and thermal residual stress in the suction-cast alloy.

(b) The friction stir processed alloy exhibited significantly higher compressive strength than the as-cast alloy and suction-cast alloy owing to grain refinement and stress induced phase transformation effect.

(c) The strain rate sensitivity for the as-cast alloy was the highest and it decreased under rapidly cooled suction-cast alloy and friction stir processed alloy because of the increase in athermal strengthening contributors in the suction-cast alloy and the friction stir processed alloy.

(d) The quasi-static deformation mechanisms in the as-cast alloy was characterised by formation of wavy deformation bands. The suction-cast alloy under quasi-static compression displayed strain partitioning at moderate strains and homogeneous deformation at higher strains. The friction stir processed alloy under quasi-static loading exhibited deformation induced phase transformation effect, grain elongation and subgrain formation.

(e) The high strain rate compression test in the as-cast alloy resulted in heavy dislocation pile-up at interphase boundary, stacking fault interactions and formation of twins, deformation bands and subgrains. The substructures formed in the suction-cast alloy under high strain rate loading were deformation twins and bands. The deformation mechanisms of friction stir processed alloy under high strain rate loading was characterised by deformation induced effect, twin formation and grain refinement by dynamic recrystallization (DRX).

Table 7.1 List of key findings of the thesis work

Sample	Phase(FCC% : BCC%)	Grain size (µm)	Compressive strength (MPa)	SRS (m)	Quasi-static deformation mechanisms	Dynamic deformation mechanisms
IM	84:15	~1000	250	0.035	Wavy deformation bands, interphase boundary	Deformation twins, stacking fault interactions, interphase boundary, subgrain boundary
SC	84:15	153.6	420	0.023	Strain partitioning between FCC and BCC phases at moderate strains and homogeneous deformation at higher strains	Deformation twins, deformation bands
FSP	6:92	15.45	996	0.019	Deformation induced effect, subgrain formation, grain elongation	Deformation induced phase transformation, traces of deformation twins, grain refinement by DRX

7.3 Future Scope

In conclusion, this thesis is an attempt to address a few major constraints in bringing high entropy alloys to the mainstream large-scale production and find its potential use in high strain rate applications. However, the alloy under this study needs more testing and characterisation so that the alloy can be used commercially.

(a) The materials used for high strain rate applications usually require high temperature resistance, and hence, further high temperature tests can be conducted for all conditions of the alloy.

(b) The cryogenic properties of the alloy will complement the high strain rate test as metallic materials exhibit similar deformation mechanisms to that under high strain rate loading may also be carried out.

(c) The shear resistance of the alloy can be tested to determine the resistance of the alloy against shear band formation under high strain rate loading.

(d) Corrosion and creep test are equally important for any alloy before they can be used in real life practice and hence can be carried out.

List of Publications

Journals

1 **S Tamuly,** S Dixit, B Kombaiah, P Khanikar. "Strengthening Mechanisms and Deformation Behavior of Industrially cast and Lab cast Dual Phase High Entropy alloys", Met. Mater. Int.(2022) DOI: 10.1007/s12540-022-01211-x

2 **S Tamuly,** S Dixit, B Kombaiah, P Khanikar. "High strain rate deformation of industrially melted $Al_{0.65}CoCrFe_2Ni$" (submitted).

3 **S Tamuly**, A Tiwari, P Venkitanarayanan, P Khanikar. "Strain rate effects of friction stir processed dual phase high entropy alloy"(under preparation)

4 **S Tamuly,** S Dixit, P Venkitanarayanan, P Khanikar "Dynamic deformation behaviour of rapidly cooled suction-cast high entropy alloy", (under preparation)

Patent

1 **S Tamuly,** S Dixit, C Halder, R Kondabalu, P Khanikar and SK Jha, Application no. 202041057507 (India), "A multi component alloy and a method for its production thereof"

Conferences Presentations

1 **S Tamuly,** S Dixit, P Venkitanarayanan, P Khanikar "Effect of cooling rate on high strain rate deformation of dual phase high entropy alloys", in TMS 2021-Virtual, held from March 15-18, 2019

2 **S Tamuly,** S Dixit, P Khanikar "Dynamic deformation behavior of suction cast dual phase high entropy alloy", in SICE-2020, December 2020, Virtual mode IIT Bombay.